

CHAPTER 14: THE OCEANIC CRUST

William M. White

Dept. of Earth & Atmospheric Sciences
Cornell University
Ithaca, NY 14850 USA
(607) 255-7466; Fax (607) 254-4780
wmw4@cornell.edu

and

Emily M. Klein

Div. of Earth and Ocean Sciences
Nicholas School of the Environment
Duke University
Durham, NC 27708-0227 USA
(919) 684-5965; Fax (919) 684-5833
ek4@duke.edu

keywords: mid-ocean ridge basalt, mid-ocean ridges, magmatic processes, back-arc basins, back-arc basin basalts, oceanic volcanism, spreading centers

Synopsis

Oceanic crust is created as magma rises to fill the gap between diverging tectonic plates and consumed in subduction zones. It is geologically young, with a mean age of 60 m.y., and it is thin, averaging 6.5 km in thickness. Ocean crust consists almost exclusively of extrusive basalt and its intrusive equivalents. This chapter focuses on the roughly 1.5-2 km thick “volcanic layer” consisting of lava flows that overlie the feeder dikes that make up the sheeted dike complex. The basalts of the oceanic crust, referred to as mid-ocean ridge basalts (MORB), are dominantly tholeiitic and are on average depleted in incompatible trace elements compared to basalts erupted in other tectonic environments. Isotopic compositions suggest their depleted character is inherited from their mantle source and that this source varies in composition both locally and on the scale of ocean basins. Their major element chemistry appears to be controlled primarily by the temperature of the underlying mantle, which determines the extent and pressure of melting, and consequently the thickness of the oceanic crust and the depth of the ridge axis. Basalts erupted at back-arc spreading centers, called back-arc basin basalts (BABB) are compositionally similar to MORB, but have some compositional features suggesting a dilute subducted lithosphere-derived component in their source.

1 Introduction

When Harry Hess first proposed the theory of sea-floor spreading, he imagined that mantle peridotite upwelling at mid-ocean ridges reacted with water to form a serpentinite oceanic crust (Hess, 1962). The sea-floor spreading concept proved correct, but his original hypothesis missed one important point: mantle upwelling beneath mid-ocean ridges undergoes decompression melting and these melts rise buoyantly to the surface to form a basaltic, rather than serpentinitic, oceanic crust. Approximately sixty percent of the Earth's surface consists of oceanic crust (Cogley, 1984), and most of it has formed in this way at divergent plate boundaries called mid-ocean ridges or spreading centers (Fig. 1). The global rate of ocean crust production is 3.4 km²/yr; how this might have varied in the past is a matter of debate (e.g., Rowley, 2002, 2008; Müller et al., 2008a). Additionally, oceanic crust can be created, or at least substantially

thickened, when mantle plumes generate melt that erupts through the oceanic lithosphere, creating oceanic islands or oceanic plateaus. These plateaus are the subject of Chapter 19 and will not be discussed here. Once created, the oceanic crust is transported off-axis to each side of the spreading center, accumulating sediment (discussed in Chapter 18) as it ages, and is ultimately consumed at subduction zones and returned in a modified form to the mantle (see Chapters 20 through 22). Thus, in contrast to continental crust, oceanic crust is distinctly ephemeral: its mean age is about 60 m.y. (Cogné et al., 2006) and it is nowhere older than about 167 Ma (Koppers et al., 2003), except in the Eastern Mediterranean where *in situ* crust as old as 270 Ma may be preserved (Müller et al., 2008b).

The oceanic crust plays a key role in the on-going processes that modify the compositions of major earth reservoirs. As the product of mantle melting, the generation of new oceanic crust continuously changes the composition of the upper mantle from which it forms (e.g., Chapter 2.08). This has a profound effect on the mantle, because if present rates of oceanic crust production are typical of those in the past, a considerable fraction of the mantle has melted to produce oceanic crust. The ocean crust is also a primary interface of exchange between fluids of the earth's surface and the solid earth below. Hydrothermal circulation of seawater through the ocean crust, for example, is a major factor controlling the chemistry of seawater (e.g., see Chapters 17 and 6.07). Subduction and consequent dehydration of hydrothermally altered oceanic crust is believed to initiate island arc volcanism, and the particular composition of the subducting crust affects the compositions of the island arc magmas (e.g., see Chapters 20 through 22). The deep subduction of altered ocean crust is also the primary means of recycling material from the surface back to the mantle where, convectively mixed with ambient mantle, it may form both the source region of some hot spots and dispersed chemical heterogeneities (Hofmann and White, 1982). Changes in rates of sea-floor spreading, and consequently the age and elevation of oceanic crust, have been the major cause of eustatic sea-level change over the past 180 Ma (Cogné et al., 2006). Thus, an understanding of the oceanic crust is central to our elucidation of diverse geologic processes.

This chapter reviews the architecture of the oceanic crust, the geochemical processes by which it is created, and its major element, trace element, and isotopic composition. The principal focus is on the more-readily sampled volcanic upper oceanic crust; the gabbroic lower crust is the subject of Chapter 15. The oceanic crust begins to react with seawater as soon as it is created

and these processes eventually result in significant modification of its composition. This hydrothermal alteration is the subject of Chapter 17; consequently this chapter focuses exclusively on the pristine magmatic composition of oceanic crust. Finally, oceanic crust acquires a veneer of sediment, the nature and composition of which is the subject of Chapter 18. More detailed perspectives on these and related topics such as melting and melt percolation models (Chapter 16), mantle heterogeneity (Chapter 2.03), and subduction zone processes (Chapters 20 through 22) are presented elsewhere in these volumes.

2 Architecture of the Oceanic Crust

2.1 Vertical Structure

The structure of igneous oceanic crust (Figure 2) has been deduced from seismic studies, drilling of the ocean crust, exposures of the deeper crust at fracture zones and rare tectonic windows, and studies of portions of the oceanic crust that have been obducted onto land (ophiolites). The uppermost layer consists of basaltic lava flows and pillows. In ODP Hole 504B this extrusive layer is 780 m thick (Alt et al., 1993); in ODP Hole 1256D it is 881 m thick (Umino et al., 2008). It is typically 800 m thick in the Hess Deep (Karson, 2002). A 20 to 60 m thick transition zone typically separates the eruptive layer from the underlying sheeted dike complex, which forms as magma freezes in dikes, typically 0.5 to 2 m wide, that feed the eruptions that form the overlying layer. This sheeted dike complex is 350 m thick in Hole 1256D and 1060 m thick in Hole 1256D (Alt et al., 1993, Umino et al., 2008). In the Hess Deep, near the East Pacific Rise (EPR), the sheeted dike complex varies in thickness from 300 m to 1200 m (Karson, 2002). Seismic studies are generally consistent with these observations, suggesting that the thickness of lavas and dikes is typically 1.5 to 2 km thick. Together, the lavas and dikes constitute seismic layer 2 (layer 1 is the sediments), which is sub-divided into layer 2A, thought to correspond to the lavas, and layer 2B, thought to correspond to the dikes. However, some have argued that the seismically identified boundary between these two is actually an alteration boundary (e.g., Christeson et al., 2006). The sheeted dike complex is underlain by seismic layer 3, which consists of intrusive gabbroic rocks of diverse textures and lithologies, which are described in Chapter 15. The total thickness of oceanic crust averages about 6.5 km, meaning the gabbroic layer is typically 4.5 to 5 km thick and constitutes over 70% of the volume of oceanic crust.

2.2 Ridge Segmentation

The 50,000 km global ridge system is divided into distinct segments. The largest scale of segmentation is that of the ocean basin, where systematic, but sometimes subtle differences in radiogenic isotopic composition suggest the mantle beneath each major ocean basin has evolved more or less independently for substantial periods of Earth history (Batiza, 1996). At smaller scales, a hierarchy of transform and non-transform offsets tectonically segment mid-ocean ridges (Macdonald et al., 1988, 1991). First-order segments are of the order of 300-500 km in length and are bounded by major transform faults. On fast-spreading ridges, second-order segments, typically 50-300 km in length, are bounded by large overlapping spreading centers that offset the ridge by at least 2 km. On slow-spreading ridges these second-order segment boundaries are bends or jogs in the ridge. Third-order segments, typically 10-50 km in length, are bounded by smaller overlapping spreading centers on fast-spreading ridges and larger gaps in chains of volcanoes on slow-spreading ridges. Fourth-order segments have also been identified as deviations from axial linearity (devals) on fast-spreading ridges and small gaps in volcanic chains on slow spreading ridges. First-order segments persist for 10 million years or more; higher order segmentation is progressively more transient.

In some areas, there is clear evidence of a correspondence between the hierarchical scales of tectonic and magmatic segmentation. In an examination of lavas erupted along the southern EPR, for example, Sinton et al. (1991) showed that isotopically coherent domains (primary magmatic segments) several hundred kilometers in length are bounded by large-offset overlapping spreading centers. Nested within these primary magmatic segments, are numerous secondary magmatic segments that share a common parental magma composition and are bounded by smaller offset overlapping spreading centers. In a detailed study of variations in lava composition along the northern EPR, Langmuir et al. (1986) showed further that devails (fourth-order segment boundaries) often correspond with the changes in magma composition in terms of fractionation and/or enrichment. It should be noted, however, that even along fast-spreading ridges, where the higher order tectonic features are most easily identified, not all large-offset transforms correspond to changes in isotopic or source composition (e.g., the Clipperton transform), and there may be variations in composition that grade continuously across several hundred kilometers of ridge irrespective of the presence of overlapping spreading centers or devails (e.g., 12-14°N EPR; Castillo et al., 2000).

2.3 Morphology, Structure, and Spreading Rate

The morphology and structure of mid-ocean ridges varies with spreading rate. Slow-spreading ridges, those with full spreading rates less than 4 cm/yr such as the Mid-Atlantic Ridge, are characterized by rough fault-dominated topography. The plate boundary is marked by a prominent fault-bounded graben, or axial valley, that is typically 10 km or more wide and 1 km or more deep. Within the axial valley, volcanic ridges and small seamounts coalesce and overlap to form a diffuse neovolcanic zone. Lava flows are often small and dominantly of pillow lava morphology suggesting low effusion rates. Fast-spreading ridges, with spreading rates in excess of 8 cm/yr such as the EPR, have smoother topography and lack a prominent axial valley. Instead, there is a comparatively narrow axial summit trough or graben. Fornari et al. (1998) recognized two types: narrow axial *troughs*, $<\sim 200$ m wide and $<\sim 15$ m deep, formed by collapse of lava flow surfaces over eruptive fissures or conduits, and wider (300–2000 m wide and 30–100 m deep), fault-bounded axial summit *graben* of primarily tectonic origin. The neovolcanic zone is restricted to the zone within a kilometer or so of this feature, although some off-axis flows do occur. Constructive volcanic features are restricted to small lava domes. Lavas are more often lobate and sheet flows, and have other features such as large collapse pits that suggest high lava volumes and high effusion rates, although pillow flows also occur, particularly near ridge offsets. Intermediate spreading ridges, with spreading rates between 4 and 8 cm/yr, have morphologies that vary between those typical of fast- and slow-spreading. Indeed, the intermediate-spreading Juan de Fuca Ridge has segments exhibiting the full range of morphology (Carbotte et al., 2006).

Ultra-slow spreading ridges, those with full spreading rates less than about 15 mm/yr, such as the Gakkel Ridge in the Arctic and portions of the Southwest Indian Ridge, are different yet again. The Gakkel ridge, the slowest-spreading ocean ridge, consists of a western volcanic zone, a central zone that is nearly amagmatic, and an eastern zone of widely spaced volcanoes. The eastern volcanic zone of the Gakkel consists of widely spaced volcanic edifices within the axial valley. Dredge recoveries were dominated by basalt with some peridotites and altered diabbases. The western volcanic zone is reminiscent of slow-spreading ridges and consists of 15–50 km long volcanic ridges that rise from a deep and wide axial valley bounded by high-angle normal faults. Short segments containing small volcanic cones separate the volcanic ridges. The axial valley deepens into the sparsely magmatic zone, located near 3° E at a non-transform

offset in the ridge. Dredge recoveries in this >80 km long zone consisted of peridotite and serpentinite with rare older basalt and dolerite (Michael et al., 2003), suggesting intermittent magmatism. Amagmatic or sparsely magmatic mid-ocean ridges such as this correspond best to Hess's original vision of sea-floor spreading.

These variations in spreading center morphology reflect the interplay between tectonic stretching of the lithosphere and its thermal state (Phipps Morgan and Chen, 1993). The thermal state in turn reflects the balance between magmatic and hydrothermal heat fluxes. When the magma flux is high, as it is in fast-spreading ridges, the axial lithosphere is weak, and ductile flow dominates over brittle deformation. When the magma flux is lower, as it generally is along slow spreading ridges, the lithosphere deforms more brittly, resulting in rough topography and large axial grabens. The important role of the magmatic heat flux in governing axial morphology is demonstrated by the observation that magmatically robust segments of the slow- and intermediate-spreading ridges, such as segments of the Juan de Fuca and Reykjanes Ridges, have morphology more similar to fast-spreading ridges.

2.4 Magmatic Processes and Magma Chambers

Over the past several decades our understanding of the process by which oceanic crust is created has advanced substantially, although it remains imperfect. Seismic reflection studies have revealed the existence of axial magma chambers (AMC) beneath intermediate (4-6 cm/yr) to fast-spreading (>6 cm/yr) ridges, such as the Juan de Fuca Ridge and EPR. These magma chambers can extend for 10's of km along axis and appear to be steady-state features. The top of the AMC is typically at a depth of about 2 km (e.g., Detrick et al., 1987; Sinton and Detrick, 1992), although it can be as shallow as 0.76 km and as deep as 4.5 km (van Ark et al., 2007). The AMC is typically only 0.5 to 1.5 km wide, but it can be as narrow as 0.25 km and as wide as 4 km. Seismic refraction and tomographic studies suggest the zone of pure melt is quite thin, only 50 to 100 m deep (e.g., Kent et al., 1990, Toomey et al, 1990). This overlies a deeper and wider (> 8 km) mush zone (melt plus crystals) and partially solid transition zone that extends to the base of the crust. Melt from the mantle is focused toward the ridge (e.g., Spiegelman and McKenzie, 1987) and replenishes both the mush zone and the melt lens where cooling and crystallization take place, forming the gabbroic layer. Periodically, extensional forces associated with seafloor spreading create a pathway for dike injection above the melt lens. Repeated dike injection forms the sheeted dike complex. If the dike pierces the surface, magma erupts on the

ocean floor as lava, forming the eruptive layer. Large eruptions produce extensive sheet flows, while pillows and pillow mounds are the products of smaller eruptions (and perhaps, the waning stages of larger flows). Below the crust lie mantle rocks that are the residues of a previous melting event that provided the melt that formed the ocean crust above (Dick et al., 1984; Michael and Bonatti, 1985; Johnson and Dick, 1992).

Magma chambers appear to be much rarer on slow spreading ridges, as only a couple of examples have been found thus far (e.g., Singh, et al., 2006), although this might partly reflect the difficulty of identifying them in rough terrain. Based on present evidence, magma chambers on slow-spreading ridges appear to be ephemeral rather than permanent.

Perhaps remarkably, there appears to be no dependence of crustal thickness on spreading rate down to spreading rates of 2 cm/yr (Figure 3). This suggests that the crustal creation process is substantially similar on both slow- and fast-spreading ridges. Differences in spreading rate, however, do result in differences in thermal regime, which affect magmatic evolution within the crust, and we will discuss these in greater detail in a subsequent section. Figure 3 also shows that below about 2 cm/ yr crustal thickness decreases rapidly with decreasing spreading rate. Thus crustal creation at ultra-slow-spreading ridges such as the Gakkel Ridge may differ in significant ways from the process at faster-spreading ridges. Dick et al. (2003) have argued that the near constancy of crustal thickness with spreading rate implies that mantle flow beneath must have a buoyant component, at least beneath volcanically robust segments of ultra-slow spreading ridges, rather than being merely passive.

Volcanic eruptions on mid-ocean ridges have yet to be visually observed, with the exception of the portion of the ridge dominated by the Iceland hotspot. However, several eruptions have been detected seismically and evidence of very recent eruptions has been observed at a number of sites. Most recently, a 2005-2006 series of eruptions at 9°50'N on the EPR were observed by ocean-bottom seismometers, several of which were enveloped in lava (Tolstoy et al., 2006). The eruption occurred in essentially the same area of the ridge where in 1991 the immediate after-effects were observed of a similar, but smaller eruption (Haymon et al., 1993). Dating with the (^{210}Pb)/(^{226}Ra) technique suggests several eruptions have occurred in the past 100 years in the super-fast spreading region near 17°30'S on the EPR (Bergmanis et al., 2007). And at least 3 dike and eruption events occurred on the CoAxial Segment between 1981 and 1993, with the 1993 event being detected seismically (Embley et al., 2000). A 1986

eruption on the Cleft Segment of the Juan de Fuca Ridge produced a hydrothermal burst or “megaplume”, and new pillow mounds associated with the eruption were subsequently mapped (Embley and Chadwick, 1994). A 1998 eruption of Axial Seamount was monitored by *in situ* sea-floor instruments, one of which was overrun and entrapped by the lava flow (Fox et al., 2001). The Rose Garden hydrothermal system on the Galapagos Spreading Center, one of the initial hydrothermal vent communities discovered in 1979, was found to be buried by lava flows when revisited in 2002 (Shank, et al., 2003). These observations are consistent with the eruption recurrence interval of a decade or so for intermediate to fast-spreading ridges estimated by Perfit and Chadwick (1998). Even on the ultra-slow spreading eastern Gakkel Ridge, side-scan sonar revealed very young lavas flows where a seismic swarm had occurred in 1999 (Edwards et al., 2001).

3 Creation of Oceanic Crust at Mid-Ocean Ridges

3.1 Mantle Flow and Melting

In the simple passive model for mantle melting illustrated in Figure 4, viscous drag associated with seafloor spreading draws mantle up from depth (e.g., Oxburgh, 1965, 1980; Lachenbruch, 1976; McKensie and Bickle, 1988; Plank and Langmuir, 1992). Below the solidus, mantle will rise adiabatically (isentropically), along a path T-P path given by $(\partial T/\partial P)_s = T\alpha V/C_p$ where T is temperature, α is the coefficient of thermal expansion, V is molar volume and C_p is heat capacity (Figure 4). This slope will be steeper than the slope of the solidus, which is given by the Clapeyron expression, $(dT/dP) = \Delta V_m/\Delta S_m$ where ΔV_m and ΔS_m are the volume and entropy change of melting, respectively. Consequently, provided the mantle is initially hot enough, it will eventually intersect the solidus and melting will begin. Once melting begins, the rising mantle will follow a shallower T-P path because energy is being consumed by melting. Continued corner flow causes the mantle to rise further, melting more as it ascends; thus, the amount of melting that a parcel of mantle will experience is governed by the difference in pressure between the depth of intersection of the solidus (P_0) and the depth at which it turns the corner and no longer decompresses (P_f ; depth of final melting). Seismic studies suggest that beneath the EPR P_0 occurs (i.e., significant melting begins) at a depth of about 70 to 100 km, although traces of melt may be present as deep as 150 km (Forsyth et al., 1998, Gu et al., 2005, Yang et al., 2007).

An important aspect of this and related models is that mid-ocean ridge basalts (MORB) are not generated at a unique depth of melting or by a unique percentage of melting. Rather, they are mixtures of melts generated over a range of pressures and over a range of melting percentage. A relatively large volume of mantle contributes small-degree melts created at depth (Figure 5). A much smaller volume of mantle contributes large-degree melt fractions, and only a quite small volume of mantle rises to the base of the crust directly beneath the spreading center and melts to the maximum extent. It should also be noted that it is this small volume of mantle that melts to the maximum extent that forms the uppermost mantle and is the most likely to be sampled in fracture zones or observed in ophiolites.

One can nevertheless define a mean pressure (\bar{P}) and mean extent of melting (\bar{F}), simply by integrating these parameters over the melting volume (Plank and Langmuir, 1992). In the simplest example, where the melting volume is an equilateral triangle, mantle upwelling velocity is constant across the base of the region, melting is a linear function of height above the base of the triangle, and all melt is focused into the ridge axis with equal efficiency, the mean extent of melting will be 1/3 the maximum and the mean pressure of melting will be the pressure 1/3 of the way up the melting region. However, incompatible elements, which we define here as those elements strongly concentrated in a melt phase in equilibrium with a solid, will be derived disproportionately from the regions undergoing only a small extent of melting such that for these elements, the effective mean extent of melting will be 1/2 the maximum extent of melting (Plank and Langmuir, 1992). In the model illustrated in Figures 4 and 5 there is an implicit relationship between the mean depth of melting, \bar{P} , the depth of the initial intersection of the solidus, P_o , the total height of the melting column, and mean and maximum extent of melting. Hotter mantle will intersect the solidus at greater depth and higher pressure, resulting in a longer melting column and a large mean and maximum extent of melting than will colder mantle. This relationship leads to correlations between magma chemistry, axial depth, and crustal thickness that we discuss in a subsequent section.

In reality, the mantle flow field will be more complex if flow is not merely passive (e.g., Scott and Stevenson, 1989) and melting will be a more complex function of height. For example, Asimow et al. (2004) point out that the $1/T$ dependence of $(\partial S/\partial T)_p$ leads to increased melt productivity with increasing melt fraction during batch melting. Exhaustion of phases such as clinopyroxene and garnet will also affect the rate at which melt is produced as a function of

pressure. More complex mantle flow patterns, varying efficiency of melting focusing, and other factor also complicate the picture.

The homogeneity of MORB compared to basalts from other tectonic regimes suggests that, on the whole, mixing of the varied melts produced within the melting region is relatively efficient. Much of this mixing likely occurs in shallow axial magma chambers. There is, however, some evidence that the primary melts are quite diverse, as the model in Figure 5 would suggest. There are several lines of evidence for this. The first is chemical heterogeneity between lava flows closely related in space and time and within individual lava flows (e.g., Rubin et al., 2001, Rubin et al., 2009, Bergmanis et al., 2007). Only some of the chemical variability within individual flows can be attributed to the effects of low-pressure fractional crystallization. For example, Bergmanis et al. (2007) document correlated $\text{MgO}-^{206}\text{Pb}/^{204}\text{Pb}$ variations in a single <15 year old, ~20 km long lava flow on the southern EPR. They attribute this to incomplete mixing of magmas in shallow, seismically imaged, axial magma chambers. Rubin et al. (2001) show that the extent of within-flow compositional heterogeneity correlates positively with flow volume on slow-spreading ridges; lavas from the superfast-spreading southern EPR are, however, more homogeneous than this global trend would predict. They also found that compositional heterogeneity is inversely correlated with spreading rate: more homogeneous lavas erupted on faster spreading ridges probably reflecting the greater thermal stability and longevity of sub-ridge crustal magma bodies, as well as, perhaps, higher eruption frequencies.

A second line of evidence comes from studies of melt inclusions. Melt inclusions are small pockets of melt that are trapped within phenocrysts as the minerals crystallized. Thus, to the extent that the phenocrysts crystallized from a less evolved or less mixed melt, the melt inclusions record the nature of more primitive melt compositions. Studies of melt inclusions have revealed that although they are broadly similar in major element composition to their host lavas, they tend to extend to more primitive (higher MgO) compositions, suggesting that they indeed record an earlier point in the evolutionary history of the magma (e.g., Sobolev and Shimizu, 1993; Sinton et al., 1993; Nielsen et al., 1995; Shimizu, 1998; Sours-Page et al., 1999, 2002, Zhang et al., 2010). Melt inclusions from the FAMOUS area near 37°N on the MAR display major- and trace element chemical trends indicating that they are genetically related, highly primitive magmas (Laubier et al., 2007). Comparison of these trends with predicted curves for models of peridotite melting indicates that compositional variations are best

reproduced by polybaric partial melting of a relatively homogeneous mantle source and subsequent mixing in various proportions of the melt batches produced at different degrees of melting and/or in different parts of the melting system. These observations suggest that transport of melts from the melting region to the site of olivine crystallization occurs without significant chemical exchange with the surrounding mantle.

Finally, near-axis seamounts, which are believed to tap the less pooled products of melting beneath the adjacent ridge (e.g., Graham et al., 1988; Batiza and Vanko, 1984; Niu and Batiza, 1997; Karsten et al., 1990; Hekinian et al., 1989; Reynolds et al., 1992), record a wider range of magma compositions than are erupted along the adjacent ridge, including both more depleted and more enriched compositions.

3.2 Melt Extraction and Flow

Melting in peridotite begins at points where three or more different kinds of mineral grains touch, because on the mineral grain scale, it is only at these grain junctions where the minimum melting composition occurs. As melt fraction increases, the melt will eventually spread along grain edges forming an interconnected network. Once melt fraction reaches 0.5% to 3%, depending on interfacial free energies, permeability increases rapidly and the melt will be expelled upward by a combination of buoyancy and compaction (von Bagen and Waff, 1986; Wark et al., 2003). Melt may initially segregate into horizontal melt-rich horizons or sills deep within the melting region (Rabonowicz and Toplis, 2009). Depending on mantle viscosity, these sills may then rise as compaction waves, or rotate and form a set of vertically oriented melt-rich veins or finger-like channels (Rabonowicz and Toplis, 2009; Spiegelman and Kelemen, 2003).

Several lines of evidence suggest that melt transport through the uppermost mantle is indeed through such vertically oriented melt-rich channels. The first is that basalts generally and MORB in particular are not in equilibrium with residual peridotites from the uppermost mantle (e.g., O'Hara, 1968). The second observation is the diversity of melt inclusion compositions mentioned above. A third line of evidence is the abundant dunite veins and channels observed in mantle sections of ophiolites, apparently produced as melt-rock reaction results in dissolution of orthopyroxene and precipitation of olivine (e.g., Kelemen, et al., 1995). At depths greater than 20 km, these melt channels may be harzburgite or lherzolite (Liang et al., 2010). Spiegelman and Kelemen (2003) found that these channel systems could produce significant diversity even from a homogeneous source in complete chemical equilibrium because channelization can

transpose the chemical variability produced by melting throughout the melting column into horizontal variability across the width of the channel. The centers of channels contain trace element–enriched melts from depth, while the edges of the channels transport highly depleted melts extracted from the interchannel regions at shallower levels. Hewitt and Fowler (2009) suggest that the vast majority of melt could be expected to eventually flow into these channels where ascent velocity would be on the order of 100 m/yr, leaving the residual matrix with melt fractions of <0.5%. On the other hand, Jull et al. (2002) concluded that disequilibrium among U-decay series isotopes is best explained if ~60% of the melt travels to the surface slowly via porous flow and the remainder travels more rapidly through these high-porosity channels. The constraints imposed on melt segregation and flow by U-decay series isotopes are discussed in greater detail in Chapter 16.

3.3 Crystallization

As melt rises toward the surface, it eventually encounters a conductive cooling regime where temperatures decrease more rapidly than adiabatic. At that point, which represents P_f , melting ceases and the melts, which are never superheated (i.e., they were always just saturated with at least one mantle phase), begin to crystallize. Because the composition of the phase or phases initially crystallizing is different from that of the bulk liquid composition, the liquid composition evolves through fractional crystallization. At least since the work of O'Hara (1968), it has been understood that essentially all basalts at mid-ocean ridges have experienced at least some fractional crystallization.

The crystallization process is now reasonably well understood, at least in comparison to the melt generation process. This understanding is based on nearly a century of work, which dates back to Bowen (1928). Nevertheless, much of the advance has come in the last two decades as thermodynamics-based computer programs, such as MELTS (Ghiorso and Sack, 1995; Ghiorso et al., 2002) and PETROLOG (Danyushevsky, 2001), calibrated from abundant laboratory experiments and petrological observations, make it possible to numerically simulate the chemical evolution of liquids undergoing fractional crystallization with some success.

Much of this crystallization occurs at relatively low pressure within the oceanic crust. Figure 6 shows an example of chemical variations in recent lava flows from the 9°37'N area of the EPR (Smith et al., 2001). The variation in major elements is well modeled with the MELTS simulation of low-pressure (0.1 GPa) fractional crystallization of olivine, plagioclase, and

clinopyroxene assuming the presence of small amounts of water. These pressures correspond well with the depth of the seismically imaged axial magma chamber in this area. Yet not all chemical variation in MORB is so readily explained by low-pressure fractionation of observable phenocryst phases. In many instances, MORB magmas appeared to have evolved through crystallization of significantly greater amounts of clinopyroxene than would be expected to occur at low pressure (e.g., Fisk et al., 1980, Flower, 1980). Laboratory experiments demonstrated that the range of compositions where clinopyroxene is a stable liquidus phase expands with increasing pressure, implying that crystallization begins well before magmas reach crustal magma chambers (e.g., Grove et al., 1992). The pressure dependence of clinopyroxene saturation has been parameterized by Herzberg (2004) and Villager et al. (2007) in a way that allows calculation of the pressure of crystallization. Herzberg (2004) and Villager et al. (2007) concluded that crystallization may begin at pressures as high as 1 GPa, which corresponds to a depth of roughly 30 km. Consistent with earlier conclusions of Michael and Cornell (1998), they found that the dominant pressure of crystallization is related inversely to spreading rate and magma supply. Thus at fast spreading ridges and slow spreading ridges with robust magma supply such as the Reykjanes Ridges, crystallization occurs primarily within the crust, while at slow spreading ridges, crystallization within the mantle dominates. Crystallization is also deeper in the vicinity of fracture zones. These effects simply reflect greater penetration of conductive cooling where the magmatic heat flux is lower.

Since, as noted above, the beginning of crystallization coincides with the end of melting, these results imply that P_f varies with spreading rate and magma supply. Thus for a given mantle temperature, melting will cease at greater depth, resulting in lower F_{max} and \bar{F} and higher \bar{P} for slow-spreading ridges compared to fast-spreading ones.

Although crystallization appears to begin at greater depth at slow-spreading ridges, the amount of fractional crystallization is generally greater at fast-spreading ridges. A good measure of the extent of fractional crystallization experienced by basaltic magmas is the molar ratio of magnesium to magnesium plus ferrous iron, i.e., $[Mg]/([Mg]+[Fe^{2+}])$; when expressed as a percentage, this is known as the Mg-number (Mg#). For reference, magma in equilibrium with mantle peridotite should have an Mg-number of 70 to 72. Sinton and Detrick (1992) found that the mean Mg-number of basalts erupted along with full spreading rates less than 5 cm/yr was 57.1 and that this decreased to 52.8 for fast-spreading ridges (>8 cm/yr). They found no

difference in mean Mg-number between intermediate and fast-spreading ridges, and no decrease in Mg-number with spreading rate above 8 cm/yr. Rubin and Sinton (2007), using a much more extensive data set, demonstrate a more or less linear decrease in Mg-number with spreading rate through the entire range (Figure 7). The corresponding decrease in MgO concentration suggests that lavas at the slowest spreading ridges erupt rough 20° C hotter than at the fastest-spreading ones. The greater extent of crystallization and lower eruption temperatures of MORB from fast-spreading ridges than slow-spreading ones is likely a direct consequence of the crystallization occurring primarily at shallower depths as discussed in the previous paragraph.

4 The Composition of the Mid-Ocean Ridge Basalts

4.1 The Average Composition of MORB

4.1.1 Major Elements

The average composition of MORB, calculated from 2010 complete whole rock analyses in the PetDB database (<http://www.petdb.org/>), is listed in Table 1. As has been known for 50 years, MORB are predominately hypersthene-normative tholeiites of comparatively uniform composition (e.g., Muir and Tilley, 1964; Engel et al., 1965). Compared to tholeiitic basalts from other tectonic environments, MORB are on average poorer in K₂O, TiO₂, and FeO. K and Ti are moderately incompatible elements, and their low concentrations are consistent with the general incompatible element-poor nature of MORB discussed in the following section. The low FeO concentrations reflect their generation at shallower depth than basalts from other environments (Klein and Langmuir, 1987).

Also listed are the mean values for basalts from the three ocean basins; although there are some differences, comparison between averages from different ocean basins only serves to highlight the remarkable uniformity of MORB major element compositions in comparison to those of basalts from other tectonic environments. Pacific MORB tend to have slightly lower Mg-numbers than MORB from the Indian and the Atlantic Oceans, which likely reflects the higher spreading rates of Pacific spreading centers and the relationship between fractionation and spreading rate discussed in the previous section. SiO₂, MnO, and CaO concentrations are nearly identical in MORB from all ocean basins. There are, however, subtle differences in the other major oxides, the likely causes of which will be discussed below. MORB lavas erupt against cold seawater, chilling the other margins to glass, which provide a convenient sample of the

liquid phase of the lava. The average glass composition, also listed in Table 1, is slightly fractionated compared to the average whole rock composition as might be expected.

4.1.2 Trace Elements

Table 2a lists the mean, log-normal mean, and standard deviations of concentrations of 30 incompatible trace elements in MORB based on a compilation 1975 analyses from the PetDB database and recent literature that have been filtered for data quality. Table 2b lists these values for the 3 ocean basins. Means are computed as:

$$Mean = \sum_{i=1}^n X_i$$

where X is the concentration and n is the number of observations. Log-normal means are computed as:

$$LogNormalMean = 10^{\frac{\sum_{i=1}^n \log(X_i)}{n}}$$

The value of the log-normal mean was explained by Arevalo and McDonough (2010). Unlike the major elements, incompatible element concentrations in MORB can be highly variable. Ba, one of the most incompatible elements, varies by a factor of 660; Lu, which is only moderately incompatible, varies by a factor of 24. Variability also illustrated by the standard deviations, particularly when compared to major elements. The more abundant major elements have standard deviations that are 17% or less of the mean value; the variability of incompatible trace elements ranges from 45% to more than 100% of the mean value. As Arevalo and McDonough (2010) pointed out, this results in incompatible element concentrations that are highly skewed and quite non-Gaussian. Mean values are consequently quite different from the mode and median values and do not characterize the population well. As they show, converting the concentration to a logarithm produces a Gaussian distribution. Thus the log-normal means characterize typical concentrations. The mean value is nonetheless useful when, for example, one wishes to calculate the total mass of an element in a reservoir as, for example, the mass of La in the volcanic layer of the oceanic crust would be calculated by the mass of the layer times the mean, as opposed to median or log-normal mean, La concentration.

Average values from a recent compilation by Arevalo and McDonough (2010) as well as older estimates of average MORB composition are also listed in Table 2. The global average

given here agrees within 10% for all elements with the Arevalo and McDonough values, except for Ba, Ta, U, and Th, for which the Arevalo & McDonough values are 14 to 22% lower.

In addition to a Global MORB average, Table 2 also lists values for NMORB (so-called normal MORB) averages. MORB have long been recognized as being depleted in incompatible elements compared to more compatible ones, and this is reflected in the average values shown in Table 2. Thus for example, average MORB is depleted in light-rare earths compared to heavy rare earths in all estimates (e.g., Figure 8). However, some MORB show light rare earth-enrichments, with $(\text{La}/\text{Sm})_N$ (i.e., chondrite-normalized La/Sm) greater than one. Many of these MORB come from ridge segments adjacent to oceanic islands such as Iceland, the Azores, and the Galapagos. The less incompatible element depleted nature of such samples is generally thought to reflect a mantle plume contribution to their sources. Incompatible element-enriched MORB (EMORB) also occur at ridge segments uninfluenced by plumes with a frequency estimated to be in the range of 3 to 10% (Langmuir et al., 1986; Donnelly et al., 2004); these likely reflect random heterogeneities in the mantle. The term NMORB was originally introduced by Schilling (1975) to refer MORB uninfluenced by mantle plumes, but the definition has evolved over the years to refer to incompatible element-depleted MORB, regardless of their location. Here we adopt the definition of Arevalo and McDonough, namely that NMORB are those MORB with $(\text{La}/\text{Sm})_N < 1$. By this definition, 70% of MORB samples in the PetDB database are classified as NMORB. NMORB are least abundant (64%) in the Atlantic where relatively large areas of the Mid-Atlantic Ridge are influenced mantle plumes and most abundant in the Pacific (86%) where plume influences are more localized.

Another problem with the MORB trace element data set is that most studies report concentrations of only some elements. For example, of the 1976 analyses used in this study, 1709 reported La concentrations, 1421 reported U concentrations, 725 reported Tm concentrations, and 208 reported K concentrations. This can lead to problems in computing elemental ratios. For example, the ratio of global mean K to mean U in Table 2 is 10384. However, the average K/U value for samples in this data set analyzed for both K and U is 16574. Thus, because many analyses are incomplete, average values in Table 2 should not be used to compute trace element ratios. Values of commonly used trace element ratios, computed from only those analyses that include both elements are listed in Table 3.

Incomplete analyses can also lead to problems in rare earth patterns. For example, average rare earth patterns reported by Arevalo and McDonough (2010) exhibit slight negative anomalies in the mono-isotopic rare earths, Pr, Tb, Ho, Tm. These apparent anomalies arise because concentrations of the mono-isotopic rare earths are less often reported and mean rare earth concentrations calculated by Arevalo and McDonough (2010) appears to reflect a sampling bias where, particularly among the Atlantic MORB, samples with overall lower rare earth concentrations were more often analyzed for the mono-isotopic rare earths. Because of that problem, average rare earth concentrations in this work were estimated using only those samples for which concentrations of at least 12 of the 14 rare earths were reported.

Figure 8 compares chondrite-normalized rare earth patterns of global average MORB, global average NMORB, and average MORB from the three ocean basins. All exhibit light rare earth depletion. The Pacific average exhibits the greatest light rare earth depletion ($(\text{La}/\text{Sm})_{\text{N}} = 0.69$), followed by the Atlantic ($(\text{La}/\text{Sm})_{\text{N}} = 0.73$) and the Indian ($(\text{La}/\text{Sm})_{\text{N}} = 0.85$). Overall rare earth abundances are greatest in the Atlantic and lowest in the Indian. The Atlantic and Pacific averages exhibit small negative Eu anomalies of 3% and 4% respectively, and this is reflected in a 3% negative Eu anomaly in the patterns of the global mean and global NMORB means. Indian Ocean MORB show no Eu anomaly on average. This observation contrasts with that of Arevalo and McDonough (2010), who found that the Eu anomaly in global average MORB was less than 1%. Since plagioclase is a common phenocryst in MORB, it seems likely that negative Eu anomalies in MORB result from plagioclase fractionation. As we discuss in a subsequent section, magmas parental to MORB, and the oceanic crust, as a whole appear to have a slight positive Eu, as suggested by Nui and O'Hara (2009).

Table 3a lists a selection of mean and median values of commonly used trace element ratios in global MORB and NMORB. Low ratios of more incompatible elements to less incompatible elements, such as Ba/La reflect the general incompatible element depletion of MORB and, as expected, are lower in NMORB than the global mean MORB. Ratios such as these have high standard deviations, reflecting the heterogeneous nature of MORB trace element concentrations. Other ratios, the so-called “canonical trace element ratios” remain constant or nearly constant, as pointed out in earlier studies. The ratios Ba/Rb, Cs/Rb, Pb/Ce and Nb/U all show mean values quite close to those initially proposed by Hofmann and White (1983), Newsom et al., (1986), and Hofmann et al. (1986). Nb/Ta and Zr/Hf also show only limited

variation; the Zr/Hf ratio in MORB is equal to the chondritic value within uncertainty, while the Nb/Ta value is somewhat lower. Arevalo and McDonough (2010) suggested that a test of the constancy of trace element ratios using log-log correlations. If the ratio of two trace elements is indeed insensitive to magmatic processes, the elements should obey the following equation:

$$\log C_i^{MORB} = \log C_j^{MORB} + \log \frac{C_i^{mantle}}{C_j^{mantle}}$$

where C_i and C_j are the concentrations of the elements of interest and the superscript *mantle* refers to the mantle source. In other words, the slope on a log-log plot should be 1 and the intercept should give the log value of the ratio in both the source and the magma. Using this test, they found that the Pb/Ce and Y/Ho ratios were indeed constant, but that Zr/Hf and Nb/Ta were not. Arevalo and McDonough (2010) found the slope of the Nb-U correlation was 1.05 ± 0.02 , implying a small but real variability in the Nb/U ratio. In this data set, the slope of $\log(U)$ vs. $\log(Nb)$ is 1.017 ± 0.007 with an intercept corresponding to Nb/U of 45.8, the slope of $\log(Rb)$ vs. $\log(Cs)$ is 0.915 ± 0.01 with an intercept corresponding to Cs/Rb of 0.0135, and the slope of $\log(Ba)$ vs. $\log(Rb)$ is 0.998 ± 0.006 with an intercept of 11.3. Thus the Nb/U and Cs/Rb ratio seem to be slightly sensitive to magmatic processes, while the Ba/Rb ratio appears to be constant.

Another test of the constancy of ratios is their correlations with other ratios. Table 3b shows a correlation matrix for trace element ratios in global MORB. Particularly strong correlations are shown in bold (all of these are statistically significant at the 0.5%; however, some correlations not shown in bold are also statistically significant). Ba/Rb, Cs/Rb, Pb/Ce, and Y/Ho do not show strong correlations with other ratios; Nb/U correlates strongly only with Th/U, but this reflects only a general correlation between Nb and U and could well result in part from analytical error in U concentrations. On the other hand, Nb/Ta and Zr/Hf show multiple strong correlations with other trace element ratios implying that they are indeed magmatically fractionated. Thus the data generally support the notion of the constancy or near-constancy of Ba/Rb, Cs/Rb, Pb/Ce and Nb/U ratios proposed by Hofmann and White (1983), Newsom et al., (1986), and Hofmann et al. (1986).

4.1.3 Isotope Ratios

Mean radiogenic and stable isotope ratios of mid-ocean ridge basalts are listed in Table 4. Variations in radiogenic isotope ratios result from variations in parent-daughter ratios over great

lengths of time. For example, to create a 1 ϵ_{Nd} variation in $^{143}\text{Nd}/^{144}\text{Nd}$ would require a variation in $^{147}\text{Sm}/^{144}\text{Nd}$ of 0.02 (about 10%) that existed for 1.4 Ga. Consequently, radiogenic isotope ratios reflect long-standing chemical variations in the mantle source (except where magmas might have recently assimilated crustal material, such as sediment, or have reacted with seawater). Correlations that exist between radiogenic isotope ratios, such as those apparent in Figures 9-12, reflect ancient coupled fractionations in parent-daughter ratios. Sr, Nd, and Hf isotope ratios are generally strongly correlated with one and other, as are the three Pb isotope ratios. On the other hand, correlations between Pb isotope ratios and the Sr, Nd, and Hf isotope ratios are weak in the dataset overall. However, strong, statistically significant correlations between Pb isotope ratios and other isotope ratios do exist within subsets of the data. For example, $^{87}\text{Sr}/^{86}\text{Sr}$ and ϵ_{Nd} correlate strongly with $^{206}\text{Pb}/^{204}\text{Pb}$ within Pacific MORB and within North Atlantic NMORB. Some, but not all, samples that deviate from these correlations come from ridge segments close to oceanic islands and reflect the influence of mantle plumes on those segments (e.g., Schilling, 1985). There are also systematic differences in radiogenic isotope ratios between ocean basins, which will also be discussed below.

The mean ϵ_{Nd} of the global MORB data set is 8.53, implying that the MORB source reservoir is depleted in light rare earths compared to chondrites, consistent with $(\text{La}/\text{Sm})_{\text{N}}$ less than 1. The isotope data indicate that this depletion has existed for a significant fraction of Earth history. However, $^{142}\text{Nd}/^{144}\text{Nd}$ measurements show that the Earth as a whole, or at least the observable part of it, is also light rare earth-depleted (Boyet and Carlson, 2005). These measurements suggest that the $^{147}\text{Sm}/^{144}\text{Nd}$ ratio of the bulk silicate Earth, or at least the observable part of it, is about 0.208, compared with a chondritic value of 0.196 (Boyet and Carlson, 2005; Caro and Bourdon, 2010). This corresponds to a present day ϵ_{Nd} of about +7. The mean MORB ϵ_{Nd} requires $^{147}\text{Sm}/^{144}\text{Nd}$ ratio of 0.211 over the age of the solar system to produce. This implies the MORB source is only slightly depleted in light rare earths compared to the observable Earth.

Lead isotopes provide particular insights into the temporal evolution of mantle sources as the two isotopes of U, ^{238}U and ^{235}U , decay to ^{206}Pb and ^{207}Pb at very different rates. Thus, the relationship between $^{206}\text{Pb}/^{204}\text{Pb}$ and $^{207}\text{Pb}/^{204}\text{Pb}$ reflects the timing of U-Pb fractionations. Indeed slopes on a $^{207}\text{Pb}/^{204}\text{Pb}$ – $^{206}\text{Pb}/^{204}\text{Pb}$ plot are a function of time:

$$\frac{\Delta^{207}\text{Pb} / ^{204}\text{Pb}}{\Delta^{206}\text{Pb} / ^{204}\text{Pb}} = \frac{1}{137.88} \frac{(e^{\lambda_{235}t} - 1)}{(e^{\lambda_{238}t} - 1)}$$

Precise calculation of age using this equation requires that the system of interest must have remained closed to Pb and U over time t ; a condition that is unlikely to be met for the mantle sources of MORB. Nevertheless, the value of t calculated from the slope of the data in Figure 10a provides a qualitative indication of the age of mantle heterogeneity. If the global data set are used, the slope of the data corresponds to an age of 1.43 Ga and very similar ages are calculated from the global NMORB, Atlantic, and Indian data sets. The slope of the Pacific data corresponds to a somewhat older age of 1.91 Ga. These ages are similar to that calculated from the oceanic island basalt data set (White, 2010). These values almost certainly do not represent the ages of discrete events, but they do demonstrate that chemical heterogeneity in the mantle old; it is much older than the age of oceanic crust but yet much younger than the age of the Earth.

$^{208}\text{Pb}/^{204}\text{Pb}$ – $^{206}\text{Pb}/^{204}\text{Pb}$ relationships reflect fractionation between the two parent isotopes: ^{232}Th and ^{238}U . For a system closed to U, Th, and Pb, the slope on a $^{208}\text{Pb}/^{204}\text{Pb}$ – $^{206}\text{Pb}/^{204}\text{Pb}$ plot is a function of time and the $^{232}\text{Th}/^{238}\text{U}$ ratio (κ):

$$\frac{\Delta^{208}\text{Pb} / ^{204}\text{Pb}}{\Delta^{206}\text{Pb} / ^{204}\text{Pb}} = \frac{\kappa(e^{\lambda_{232}t} - 1)}{(e^{\lambda_{238}t} - 1)}$$

If the value of t calculated from the $^{207}\text{Pb}/^{204}\text{Pb}$ – $^{206}\text{Pb}/^{204}\text{Pb}$ slope is used, the $^{208}\text{Pb}/^{204}\text{Pb}$ – $^{206}\text{Pb}/^{204}\text{Pb}$ slope of the global MORB data set (Figure 10b) corresponds to a $^{232}\text{Th}/^{238}\text{U}$ ratio of 2.96. This is comparable to average $^{232}\text{Th}/^{238}\text{U}$ of global MORB, which is 3.14. These isotope ratios can also be used to calculate the $^{232}\text{Th}/^{238}\text{U}$ ratio of the MORB source reservoir time-integrated over the age of the Earth, which is 3.72. This implies, not surprisingly, that the Th/U ratio of the MORB source reservoir decreased at some point in the past (e.g., Galer and O’Nions, 1985).

Variations in stable isotope ratios result from chemical processes, specifically from a reduction in free energy that results when the heavier isotope of an element preferentially enters the phase in which it is more strongly bonded. The magnitude of these isotopic fractionations varies approximately inversely with the square of temperature, so that at magmatic temperatures the fractionations are generally quite small. Not surprisingly then, stable isotope ratios are fairly uniform, particularly when compared with variations observed in these ratios in materials at the

surface of the Earth. Stable isotope ratios are sensitive to processes such as sediment assimilation and weathering, (e.g., Muehlenbachs and Clayton, 1972; Davis et al., 1998), but such samples have been excluded to the extent possible in the dataset assembled for this review. In contrast to the radiogenic isotope ratios, stable isotope ratios show few systematic relationships. $\delta^{18}\text{O}$ and $\delta^{34}\text{S}$ do show statistically significant negative correlations with Mg-number, but the $\delta^{34}\text{S}$ data are so sparse that the latter correlation is questionable. The increase of $\delta^{18}\text{O}$ with decreasing Mg-number is modest, less than 1 per mil across the entire spectrum of compositions, consistent with earlier studies (e.g., Muehlenbachs and Byerly, 1982). There are no statistically significant correlations between stable and radiogenic isotope ratios, although this may in some cases reflect the paucity of data.

4.2 Regional Variations in MORB Composition

Regional variations in the isotope geochemistry of MORB, apparent in Figures 9-12, are further illustrated in Figure 13, which shows MORB isotope compositions from the “continuous” part of the mid-ocean ridge system as a function of angular distance from the northernmost sample as calculated by Meyzen et al. (2007). While there is broad similarity in isotope ratios of MORB from all regions, there are systematic, but sometimes subtle, variations between ocean basins. The most notable of these is the differences between Indian Ocean MORB and MORB from other regions. Indian Ocean MORB have low $^{206}\text{Pb}/^{204}\text{Pb}$ and high $^{207}\text{Pb}/^{204}\text{Pb}$ and $^{208}\text{Pb}/^{204}\text{Pb}$ for a given $^{206}\text{Pb}/^{204}\text{Pb}$ and high $^{87}\text{Sr}/^{86}\text{Sr}$ (Dupré and Allegre, 1983). Hart (1984) used these latter characteristics to define what he called the DUPAL anomaly, which encompasses the South Atlantic and Indian Oceans. MORB, as well as OIB, from this region are characterized by high $\Delta^{208}\text{Pb}$ and high $\Delta^{207}\text{Pb}$, which Hart defined as:

$$\Delta 8/4 = [^{208}\text{Pb}/^{204}\text{Pb} - ^{208}\text{Pb}/^{204}\text{Pb}_{\text{NHRL}}] \times 100$$

$$\Delta 7/4 = [^{207}\text{Pb}/^{204}\text{Pb} - ^{207}\text{Pb}/^{204}\text{Pb}_{\text{NHRL}}] \times 100$$

where NHRL is the Northern Hemisphere Regression Line, i.e., the line defined by northern hemisphere Pb isotope ratios and is given by:

$$^{208}\text{Pb}/^{204}\text{Pb}_{\text{NHRL}} = 15.627 + 1.209 ^{206}\text{Pb}/^{204}\text{Pb}$$

$$\text{and } ^{207}\text{Pb}/^{204}\text{Pb}_{\text{NHRL}} = 13.491 + 0.1804 ^{206}\text{Pb}/^{204}\text{Pb}$$

High $\Delta^{208}\text{Pb}$ and low ϵ_{Nd} and ϵ_{Hf} relative to $^{87}\text{Sr}/^{86}\text{Sr}$ distinguish S. Atlantic MORB from N. Atlantic MORB (Figures 9 and 11). Both S. Atlantic and Indian MORB share high $\Delta 8/4$ and $\Delta 7/4$; Indian MORB is distinguished from S. Atlantic MORB by particularly low $^{206}\text{Pb}/^{204}\text{Pb}$ and

high $^{208}\text{Pb}/^{204}\text{Pb}$, and higher ϵ_{Nd} and ϵ_{Hf} relative to $^{87}\text{Sr}/^{86}\text{Sr}$ compared to S. Atlantic MORB.

Pacific MORB overlap Atlantic MORB in Pb isotopes, but have low $^{87}\text{Sr}/^{86}\text{Sr}$ for a given ϵ_{Nd} (Ito et al., 1987; White et al., 1987) and low ϵ_{Hf} for a given ϵ_{Nd} .

Boundaries between these domains can be sharp or diffuse. The boundary between the Pacific and Indian domains is located within the Australian-Antarctic Discordance and is quite sharp (Klein et al., 1988; Pyle et al., 1992). On the other hand, the boundary between the South Atlantic and Indian provinces, which occurs within the Indian Ocean near the Andrew Bain Fracture Zone at 30°E on the Southwest Indian Ridge (SWIR) rather than at the Bouvet triple junction, appears to be more gradual (Meyzen et al., 2007), as does the boundary between the North and South Atlantic provinces, which occurs around 23°S.

The existence of a small number of isotopic domains reflects a fundamental organization of mantle convection. The isotopic differences reflect differing chemical histories of these regions, which in turn reflect physical processes such as melt extraction and addition of material from crustal or other mantle reservoirs. Upper mantle asthenosphere is continually consumed in the production of oceanic crust and lithosphere; this consumption must be approximately balanced by flow of material into the asthenosphere, either from below or from subduction zones. Yamamoto et al. (2007) have argued that the asthenosphere is replenished by mantle plumes. In the N. Atlantic, oceanic islands have isotopic signatures that either overlap the N. Atlantic MORB field, or plot close to extensions of it. This suggests that the mantle plumes responsible for these islands may be the primary mechanism by which the N. Atlantic asthenosphere is replenished. However, this is only partly true in the S. Atlantic and generally not true in the Indian Ocean, as Meyzen et al. (2007) have pointed out. The more extreme isotopic compositions, particularly the unradiogenic Pb, have no analog in the compositions of oceanic islands of these regions. Meyzen et al. (2007) have suggested that these regions are replenished by flow from the African “superplume”, which manifests itself as a large region of slow seismic velocity extending upward through the upper mantle. This possibility is supported by analysis of shear-wave splitting in the circum-African region, which suggests radial outward flow from beneath Africa at the base of the lithosphere (Behn et al., 2004). The case of the Pacific is less clear-cut. Near ridge plumes, such as the Galapagos and Easter-Sala y Gomez, have isotopic compositions that lie within or on an extension of the Pacific MORB array. But central and south Pacific plumes, such as Hawaii, Society Is., and Samoa, plot well off the

Pacific MORB array. One possible explanation is that the Pacific plume flux is small compared to the volume of the Pacific asthenosphere, so that plumes have minimal compositional influence on it.

Batiza (1984) suggested there was an inverse relationship between spreading rate and isotopic variability. At the time, available isotopic data came mainly from the fast-spreading EPR and the slower-spreading Mid-Atlantic Ridge. Batiza suggested this resulted from more effective homogenization of heterogeneous primary melt batches in magma chambers of fast-spreading ridges, and at the local scale, individual flows do seem to me more homogeneous at fast spreading ridges (Rubin et al., 2001). The EPR is certainly more isotopically uniform than the Mid-Atlantic Ridge at larger scales as well, but in the decades since Batiza's paper, a much richer data set reveals that relationship between isotopic variability and spreading rate is not simple. As Figure 14 shows, Pacific spreading centers are isotopically uniform, despite a range spreading rates. The most heterogeneous areas of the ridge system are the slow spreading SWIR and the southern MAR, but slow-spreading ridges in the North Atlantic are less heterogeneous. New isotopic data from the very slow-spreading ridges of the Arctic region, the Gakkel, the Kolbeinsey, and Mohs Ridges are certainly more isotopically heterogeneous than the Pacific spreading centers, but less heterogeneous than the faster spreading ridges in the Indian and Central and South Atlantic. Furthermore, the slow-spreading northern Mid-Atlantic Ridge (between Iceland and the Azores triple junction) is nearly as homogeneous as the Pacific spreading centers. It certainly seems probable that steady-state magma chambers on fast- and intermediate-spreading ridges tend to homogenize magmas passing through them, but this alone seems unlikely to explain differences in isotopic heterogeneity. Figure 14 suggests that the upper mantle beneath the South Atlantic and Indian Oceans is intrinsically more heterogeneous than upper mantle elsewhere, and that the mantle beneath the Pacific is intrinsically less heterogeneous than elsewhere.

On the 100-100 km scale, the effect of mantle plumes on MORB isotopic and trace element composition has been amply demonstrated, particularly through the work of J-G. Schilling and colleagues (e.g., Schilling, 1973; Hart et al., 1973; White et al., 1978, Schilling et al., 1983). The influence of on- or near-ridge plumes, such as Iceland, the Azores, Tristan da Cunha, Discovery Seamount, and St-Paul Amsterdam, and Easter-Sala y Gomez is amply apparent in Figure 13. The effect of mantle plumes on the oceanic crust, however, goes well

beyond merely isotopic and trace element compositions. Where spreading centers pass near or over mantle plumes, such as Iceland, the Azores, the Galapagos, and Afar, ridges are typically elevated and crustal thickness is greater (e.g., White et al., 1992). Variations in major element chemistry of both MORB and abyssal peridotites also correlate with the proximity of mantle plumes. The connection appears to be that of mantle temperature and extent of melting (Dick et al., 1984). This was best demonstrated by the work of Klein and Langmuir (1987), who showed that correlations between major element chemistry, crustal thickness, and axial depth relate to mantle temperature.

Variations in major element geochemistry are dominated by the effects of fractional crystallization and partial melting. While fractional crystallization also affects trace elements, incompatible trace element variations resulting from this process tend to be small compared to variations resulting from varying extent of melting and mantle source heterogeneity. Thus to use major elements to assess mantle temperature requires first correcting for the effects of fractional crystallization. Klein and Langmuir (1987) did this by projecting the composition of each magma back along a presumed liquid line of descent to 8 wt.% MgO. The calculated $\text{Na}_{8.0}$ value at 8 wt. % MgO is thus referred to as $\text{Na}_{8.0}$. In theory, if the liquid line of descent is known for any major or trace element, a "fractionation-corrected" value of the element can be calculated (producing calculated values of, e.g., $\text{Fe}_{8.0}$, $\text{Al}_{8.0}$, $\text{K}_{8.0}$, $\text{Ce}_{8.0}$, etc.). The few elements for which the slope of the liquid line of descent changes sign as the fractionating phases change, such as CaO (due to the appearance of Ca-bearing phases on the liquidus), are more difficult to model in this way and therefore produce less reliable fractionation-corrected values. Nevertheless, most major and trace elements display fairly regular liquid lines of descent and their fractionation corrected values reveal relative differences in parental magma compositions that result from differences in melting systematics or source composition. Figure 15 shows the example of $\text{Na}_{8.0}$ and $\text{Fe}_{8.0}$ calculated from samples from a number of different regions.

Once corrected for fractional crystallization, major elements correlate in predictable ways. In general, regions with low mean $\text{Na}_{8.0}$ are also characterized by high mean $\text{Fe}_{8.0}$ (as well as low $\text{Si}_{8.0}$ and $\text{Al}_{8.0}$, and higher $\text{Ca}_{8.0}$), while other regions exhibit the opposite characteristics, as well as a continuum of compositions in between (Klein and Langmuir, 1987; Langmuir et al., 1992). Furthermore, these major element variations correlate with physical characteristics of the ridge axis from which they were recovered. Regional averages of $\text{Na}_{8.0}$ and $\text{Fe}_{8.0}$, for example,

show a positive and an inverse correlation, respectively, with the average ridge depth from which the lavas were recovered (Fig. 16). In addition, $\text{Na}_{8.0}$ correlates inversely with seismically and geologically determined estimates of the crust thickness in each region (Fig. 17). Thus, some of the most fundamental physical and chemical parameters studied at ocean ridges suggest a common origin in their variability.

The chemical systematics can be understood as the interplay of two main factors affecting the style of mantle melting: the extent of melting and the pressure of melting. Elements such as sodium are moderately incompatible during melting of the mantle minerals ($D \sim 0.02\text{--}0.03$), and therefore will be concentrated in the melt at small extents of melting. Iron varies in the melt as a function of the pressure of melting (e.g., Langmuir and Hanson, 1980). Thus, the inverse correlation between mean $\text{Na}_{8.0}$ and mean $\text{Fe}_{8.0}$ suggests that there is a positive correlation between the mean extent of melting and the mean pressure of melting. This is readily understood with reference to Figure 4: if melting begins at great depth, both the mean extent and mean depth of melting will be greater than when melting begins shallower. The correlations shown in Figure 16 suggest that melts from bathymetrically deep ridges tend to be produced by smaller extents of melting (high $\text{Na}_{8.0}$) and low pressure (low $\text{Fe}_{8.0}$), while melting beneath shallower ridges leads to larger extents of melting (low $\text{Na}_{8.0}$) at higher pressures of melting (high $\text{Fe}_{8.0}$). A region that experiences a small extent of melting would have thinner oceanic crust than a region that experiences a larger extent of melting. This, in turn, would lead to the observed correlation between a chemical parameter indicative of the extent of melting (e.g., $\text{Na}_{8.0}$) and crustal thickness seen in Fig. 17. Furthermore, if the crust is isostatically compensated, thinner crust would lead to greater ridge depth below sea level, and therefore the correlation between chemistry and axial depth (Fig. 16).

The global correlations among regional averages of major elements can in turn be related to lateral variations in the sub-solidus temperature of the mantle (Klein and Langmuir, 1987; McKenzie and Bickle, 1988). As we pointed out in an earlier section, hotter mantle intersects the solidus deeper and melts more upon ascent than cooler mantle temperatures (Figs. 4 and 5), leading to the associated correlations with axial depth and crustal thickness.

A number of studies have used the major element (and trace element) systematics of MORB to constrain the mean extent and mean pressure of melting, as well as potential temperature and the depth and temperature of intersection of the mantle solidus, both for a given

region and for the global ocean ridge system as a whole (e.g., Klein and Langmuir, 1987; McKenzie and Bickle, 1988; Langmuir et al., 1992; Kinzler and Grove, 1992; Asimow et al., 2001; Asimow and Langmuir, 2003; Putirka et al., 2007; Herzberg et al., 2007). A thorough evaluation of these parameters requires numerous assumptions that are subject to uncertainty. These include, for example, assumptions about the physical form of the melting regime including variables such as active vs. passive upwelling and variations in the final depth of melting (e.g., Scott and Stevenson, 1989; Plank and Langmuir, 1992); the processes of melt extraction and mixing (e.g., batch vs. fractional melting, percentages of melt retention, incomplete focusing of melt); a melt generation function, and the effects of source mineralogy and composition including volatile species (e.g., Langmuir et al., 1992; Asimow et al., 2001; Asimow and Langmuir, 2003). Earlier studies noted above estimated the global range in the pressure of intersection of the solidus as ~1.5 to 3.6 GPa, in the temperature of intersection of the solidus as ~1300°C to 1550°C, in the mean extent of melting as ~8% to 22%, and in the mean pressure of melting as ~0.5 to 1.6 GPa. More recently, Petirka et al. (2007), using olivine geothermometry, concluded that the average potential temperature beneath mid-ocean ridges was 1454°C and that most MORB were generated within narrow range of $\pm 34^\circ\text{C}$. They estimated the potential temperature beneath Iceland to 1616°C and the overall temperature range from the coldest mid-ocean ridges to Iceland to be 215–246°C, in good agreement with 250°C range estimated by Klein and Langmuir (1987). They suggested that effect of H₂O could reduce the estimated temperature range and lower the mean temperature estimate by 25°C. Herzberg et al. (2007) concluded that melting begins for most MORB in the range of 2.0–3.0 GPa at potential temperatures of 1280–1400°C, but under Iceland, the mantle is hotter (potential temperature of 1460°C) and melting begins at greater pressure (3.6 GPa).

Niu and O'Hara (2008) showed that regional average Mg-numbers also correlate with axial depth. They argue that the procedure used by Klein and Langmuir (1987) did not completely correct for fractional crystallization and that when this correction is done (to liquid Mg-numbers of 72), the corrected FeO concentrations (which they call Fe₇₂) show a much smaller range of variation and shallower correlation with axial depth. From this they argue that the range of potential temperatures beneath mid-ocean ridges (excluding Iceland and ridges less than 250 m deep) is no more than 70°C – too small, they argue to account for the variation in axial depth. Using their approach, however, the range of fractionation-corrected Na₂O

concentrations remains similar to that found by Klein and Langmuir (1987). They argue that rather than temperature, mantle fertility controls both axial depth and Na_2O : more fertile mantle is richer in Na_2O and is denser resulting in greater axial depth.

The difficulty with this interpretation is that more fertile mantle should melt more extensively than more depleted mantle if potential temperature is nearly constant as Niu and O'Hara (2008) assume. In this case, axial depth should correlate negatively with crustal thickness. As Figure 18 shows, the opposite is true: crust is thinnest where axial depth is greatest. Iceland, with thick crust and low Na_2O concentrations poses a particular problem for the Niu and O'Hara model and they admit, "We do not have an answer to the Iceland paradox." Furthermore, if mantle fertility rather than mantle potential temperature were to explain the variations in axial depth rather, one would expect correlations between incompatible trace element ratios and isotope ratios with axial depth. Figure 19 shows that there is no correlation between $^{87}\text{Sr}/^{86}\text{Sr}$ and axial depth; other isotope ratios and trace element ratios such as La/Sm correlate with neither axial depth nor crustal thickness. While some of the chemical variability among MORB almost certainly results from variations in mantle fertility or other chemical or mineralogical heterogeneity of the mantle (e.g., Shen and Forsyth, 1995), the weight of current evidence supports the idea that the first order trends in regional topography, basalt chemistry, and crustal thickness result from mantle temperature variations. Uncertainly remains, however, as to just what the mean potential temperature is beneath ridges and how much it varies.

4.4 Estimating the Bulk Composition of the Oceanic Crust

The compositions of MORB listed in Tables 1 and 2 represent the composition of only the volcanic layer of the oceanic crust, not the entire oceanic crust. It has been understood at least since the work of O'Hara (1968) that MORB are not primary mantle melts, rather they must have evolved through fractional crystallization from primary parents. *Prima fascia* evidence that this is so comes from the Mg-numbers of MORB. The various average compositions in Table 1 have Mg-numbers of about 60 or a little lower. These compositions would be in equilibrium with olivine having a forsterite content of about 80-85%. Mantle olivine, by contrast, typically has a forsterite content in the range of 90 to 92, which would be in equilibrium with a melt with an Mg-number around 72. Thus magmas erupted at mid-ocean ridges must have cooled and crystallized olivine, as well as other phases since leaving the mantle. Cumulates created by this process make up much of the lower oceanic crust (Chapter 15). The bulk composition of the

oceanic crust is thus the composition of lavas erupted at the surface plus cumulate minerals in the lower crust. The average composition of the oceanic crust should equal the composition of average parental magma extracted from the mantle.

A first order estimate of the average composition of the overall oceanic crust can be made by attempting to reconstruct the composition of a parental magma that would give rise to an average MORB composition through fractional crystallization. We begin by assuming that parental magmas extracted from the mantle have an Mg-number of 72. Even this assumption is problematic since MORB magmas could evolve to lower Mg-numbers during high pressure crystallization within the mantle. However, subsequent compositional evolution during fractional crystallization depends not only on parental composition, but also the pressures at which crystallization occurs, i.e., the P-T path. Constraints on this P-T path are sparse. This makes reconstruction of the exact composition of the average parental magma difficult, but a first order *estimate* is possible using the Mg-number constraint together with thermodynamics-based numerical models of magma evolution.

The estimated parental MORB magma composition, and therefore bulk oceanic crust composition listed in Table 5, was determined in the following manner. The mean glass composition listed in Table 1 was taken as a starting point (since it presumably represents a liquid composition whereas bulk rock compositions do not). A first estimate of the parental magma composition with Mg-number of 72 was made using the polynomial regression procedure of Niu and O'Hara (2008). This is a merely empirical approach based on observed trends in MORB glasses. Fractional crystallization of this composition was then simulated in version 5 of MELTS (Ghiorso and Sack, 1995; Asimow and Ghiorso, 1998) from its liquidus temperature (1266°C at 0.18 MPa) until the remaining liquid had an Mg-number of 60 (roughly that of the glass). Simulations at a variety of pressures and oxygen fugacities suggested that a pressure of 0.18 GPa, which corresponds roughly to the base of the oceanic crust, and an oxygen fugacity fixed at the quartz-magnetite-fayalite buffer produced the daughters most closely matching average glass composition. Nevertheless, the daughter liquid composition initially calculated using these conditions did not match the average glass composition well, so the composition of the parent was adjusted and the simulation repeated until an optimal result was obtained. The final parental composition listed in Table 5 fractionates to a composition matching the glass composition in Table 2 within a few percent for all oxides except CaO (the

daughter liquid is 6% poorer in CaO than the average glass composition). This is achieved at a temperature of 1202°C after 41% of the magma had crystallized. The fractionated solid phases would form a gabbro made up of 13.3% olivine, 45.5% plagioclase, 41.0% clinopyroxene, and 0.05% spinel, whose composition is listed as “cumulate” in Table 5.

The bulk oceanic crust composition should be intermediate between the average MORB composition, presumably representative of layer 2 (the volcanic layer), and layer 3 (gabbroic layer). This is the case for most oxides in the estimated bulk oceanic crust composition in Table 5, with two exceptions: MgO and Na₂O. The estimated bulk crustal composition is richer in MgO and poorer in Na₂O than either the mean or median of lower crustal gabbros listed in Table 2 of Chapter 15 (although it falls within 1 standard deviation of the latter). This suggests that the bulk ocean crust composition listed in Table 5 may be slightly too mafic. This would be the case if magmas experience some fractional crystallization in the mantle before rising into the crust. The average MORB glass composition listed in Table 1 has significantly more Na₂O (and TiO₂) than the average MORB whole rock, despite having rather similar concentrations of most major oxides. Thus it is possible that by using the glass rather than the whole rock MORB composition, the bulk crust Na₂O has been overestimated.

Trace elements Cr, Ni, and Co were estimated using the MELTS simulations. The remaining trace elements in the parental magma were estimated using the equation for trace element distribution during fractional crystallization:

$$\frac{C_i^L}{C_i^O} = (1 - X)^{D-1}$$

where C^L is the liquid composition, C^O is the parental magma composition, X is the fraction of liquid remaining, and D is the bulk partition coefficient. Partition coefficients used in the calculation are listed in Table 5 and were selected from the GERM partition coefficient database (<http://earthref.org/GERM/>) based on temperature, pressure, composition, and self-consistency. Calculated trace element concentrations of the bulk crust fall, as they should, between the MORB average concentrations in Table 2 and the lower crustal gabbro average or median concentrations listed in Table 2 of Chapter 15 with the exception of Cu, for which the bulk crustal estimate appears too low, and Zn, for which the bulk crustal estimate appears too high. The explanation in the case of copper may be the small amounts of a sulfide phase have fractionated; in the case of Zn the problem most likely lies in the partition coefficients used.

Figure 20 illustrates MORB, NMORB, and bulk oceanic crust trace element compositions from Tables 2 and 5 along with previous estimates of MORB composition in a “spider” or “extended rare earth” plot in which concentrations are normalized to the estimated bulk silicate Earth composition of Lyubetskaya and Korenaga (2007). All show some degree of increasing depletion with increasing incompatibility. It should be pointed out that Lyubetskaya and Korenaga (2007) estimate of bulk silicate Earth composition, like earlier ones such as McDonough and Sun (1995), is based partly on the assumption of chondritic relative abundances of refractory lithophile elements. However, the non-chondritic $^{142}\text{Nd}/^{144}\text{Nd}$ ratios of all modern terrestrial material (Boyet and Carlson, 2005) make this assumption questionable and raised the possibility that the Earth is depleted in highly incompatible elements relative to chondrites (Caro and Bourdon, 2010, O’Neill and Palme, 2008). If so, MORB and the oceanic crust may be less incompatible element-depleted relative to the bulk silicate Earth than this figure suggests.

All estimated of MORB composition exhibit strong negative Pb anomalies and, to varying extents, negative Sr anomalies. As was noted in an early section, average MORB also appears to have a small negative Eu anomaly. The Pb anomaly is also present in the bulk crust estimate, but is less pronounced. This reflects the compatibility of Pb in plagioclase and consequently its relatively high bulk partition coefficient during fractional crystallization within the oceanic crust. Thus the negative Pb anomaly in MORB is due in part to plagioclase fractionation.

In contrast to the negative Sr and Eu anomalies seen in MORB, the bulk oceanic crust appears to have a positive Sr and Eu anomalies of 28% and 11%, respectively, somewhat smaller than that deduced by Nui and O’Hara (2009). Thus both the negative Sr and Eu anomalies in average MORB appear to be due to plagioclase fractionation. The question of whether the Sr and Eu excesses (as well as Ta and Nb excesses) in the MORB and its mantle source balance the observed deficits in average continental crust (see Chapter 1), as argued by Niu and O’Hara (2009) is beyond the scope of this paper.

4.5 The Composition of Back-Arc Basin Crust

Behind a number of intra-oceanic subduction zones, basins have opened through a rifting and spreading process much like that at the principal mid-ocean ridges. These “back-arc basins” are floored by oceanic crust whose structure and composition largely resembles oceanic crust created elsewhere. Back-arc basins and their associated spreading centers do differ from other

ocean basins in a few respects: spreading is often highly asymmetric, the lithosphere may behave non-rigidly, and spreading is often episodic rather than steady-state. The back-arc basin spreading centers for which data exists in the PetDB database are shown in Figure 1.

A statistical summary of these data are presented in Table 6, as well as averages for three specific back-arc spreading centers that help to illustrate the range of compositions that occur. Back-arc basin basalts (BABB) are similar to MORB in many ways, but also exhibit some significant differences (Tarney et al., 1977; Tarney et al., 1981, Hawkins and Mechior, 1985; Sinton and Fryer, 1987). Comparison of averages in Tables 1 and 6 shows that BABB are, on average, somewhat richer in SiO_2 , Al_2O_3 , and Na_2O and poorer in FeO , MgO , and CaO than are mid-ocean ridge basalts. The biggest distinctions are, however, the lower TiO_2 and higher K_2O and H_2O of back-arc basin basalts. Some of these differences, notably the higher average SiO_2 and Na_2O and lower MgO appear to be related to the somewhat greater average extent of fractional crystallization. Thus while average Na_2O is lower in BABB than MORB, there is essentially complete overlap at a given MgO value (Figure 21). On the other hand, the lower FeO and TiO_2 appears to be more intrinsic, with BABB generally having lower FeO and TiO_2 than MORB at a given MgO value, although there is considerable scatter and overlap in both data sets. Comparison of trends of Al_2O_3 vs. MgO of the two dataset is particularly interesting. At the highest MgO , BABB have systematically lower Al_2O_3 , but while many or most BABB follow the MORB trend of decreasing Al_2O_3 below 8% MgO , many BABB plot well above this trend, so that the more fractionated BABB, those with less than 6% MgO have systematically higher Al_2O_3 . This effect may reflect the suppression of plagioclase crystallization by the higher H_2O content of BABB.

As has often been pointed out (e.g., Hawkins and Melchior, 1985; Fryer et al., 1990), BABB bear some similarity to lavas from island arcs, most likely because they, like arc magmas, contain a component derived (albeit indirectly) from subducting lithosphere. There is, however, considerable variation between back-arc spreading centers, as well as along individual spreading centers (Vallier et al., 1991; Sinton et al., 2003). Basalts from the North Fiji Basin have lower mean SiO_2 and higher TiO_2 than average MORB and Al_2O_3 , FeO , MgO , and CaO nearly identical average MORB, although the higher H_2O . Lavas from the Okinawa Trough show the greatest average deviation from MORB.

A number of workers have noted a relationship between the age of rifting, distance from the island arc, and lava chemistry (e.g., Tarney et al., 1977; Gill, 1976; Sinton et al., 2003). Because back-arc rifting often initiates near or within the island arc itself and migrates away through asymmetric spreading, age of rifting and distance from the arc are often related. In general, young rifts close to the arc erupt lavas with more arc-like chemistry while mature back-arc spreading centers erupt lavas closest in composition to MORB (e.g., Tarney et al., 1977; Gill, 1976). This suggests the “slab-derived component” may become progressively diluted over time (Sinton et al., 2003). This relationship is, however, not uniformly observed. For example, the lavas from Sumisu and Torishima rifts in the Izu Bonin arc display a wide range of compositions although these rifts are quite young and located virtually within the arc itself (Fryer et al., 1990). Here the variation appears to be primarily geographic rather than temporal.

Table 7 and Figure 22 compare the trace element composition of BABB and MORB and illustrate both the similarities and differences between them. Average trace element ratios in BABB are listed in Table 3. For the rare earths, BABB and MORB are remarkably similar, although BABB are on average slightly more LREE-enriched than average MORB (La/Sm_N of 1.13 vs 0.90). BABB have similar Y concentrations and are just slightly poorer in Zr and Hf than MORB. On a spider diagram such as Figure 22, both MORB and NMORB display negative Pb and Sr anomalies, whereas BABB display positive ones. MORB and BABB diverge in composition for elements more incompatible than La. Most of these highly incompatible elements, are particularly Cs, Rb, Ba, and K, are present in higher concentrations in average BABB than in average MORB, but average BABB has lower Ta and Nb concentrations than average MORB. In terms of trace element ratios, BABB have notably higher K/La, Ba/La and Pb/Ce and lower K/Rb, Nb/La, and Nb/U than MORB. Elevated concentrations of the alkalis, alkaline earths, and Pb and low concentrations of Nb and Ta are characteristic of island arc lavas; hence the average composition of BABB does indeed differ from average MORB in that it contains a “slab-derived component”, albeit less than typical island arcs.

Figure 22 also demonstrates some of the regional diversity in BABB. Although all three regions illustrated share the enrichment in alkalis and alkaline earths and depletion in Nb and Ta that distinguished BABB from MORB, the extent of this difference varies considerably. The lavas from the Okinawa Trough show particularly strong alkali enrichment; at the other extreme, lavas from the Lau Basin spreading center differ in composition from typical MORB only

slightly, although they still exhibit a small negative Ta-Nb anomaly and excess of K, Rb, Cs, and Ba.

Average isotope ratios in back-arc basin basalts are listed in Table 4. BABB have statistically significant higher mean $\delta^{18}\text{O}$, $^{87}\text{Sr}/^{86}\text{Sr}$, and Pb isotope ratios than MORB and statistically significant lower ϵ_{Nd} , $\delta^{13}\text{C}$, and δD than MORB. As Figure 23 shows, BABB typically have somewhat higher $^{87}\text{Sr}/^{86}\text{Sr}$ for a given ϵ_{Nd} . All these isotopic features also typify island arc lavas in comparison to MORB. Thus the isotopic data are consistent with the trace element data in suggesting that BABB contain a dilute slab-derived component.

Interestingly, the BABB Sr-Nd isotopic array is also somewhat more confined and extends to neither the very “enriched” isotopic signatures nor to the extremely “depleted” isotopic signatures of the MORB array. The lack of enriched isotopic signatures may in part reflect the complete absence of mantle plumes in back-arc basin environments — perhaps due to subducting lithosphere shielding these regions from deep mantle upwellings.

Figure 24 shows that Pb isotopic compositions of BABB plot within the MORB field. There is some tendency for BABB to have slightly high $^{207}\text{Pb}/^{204}\text{Pb}$ and $^{208}\text{Pb}/^{204}\text{Pb}$ for a given $^{206}\text{Pb}/^{204}\text{Pb}$ compared to typical MORB; in this sense they resemble Indian Ocean MORB more than other MORB. Continental material, which could find its way into a subduction zone either through sediment subduction or subduction erosion of the overlying plate, typically has higher $^{207}\text{Pb}/^{204}\text{Pb}$ and $^{208}\text{Pb}/^{204}\text{Pb}$ for a given $^{206}\text{Pb}/^{204}\text{Pb}$ than does MORB. Thus explanation for the slight differences in Pb isotopic composition between MORB and BABB is most likely the same as the explanation for the other isotopic differences, namely a dilute slab-derived component present in BABB.

References

- Alt, J.C., et al. (1993). Proc. Ocean Drill. Program Initial Rep., 148. College Station, TX: Ocean Drilling Program.
- Arevalo Jr, R. and McDonough, W.F. (2011). Chemical variations and regional diversity observed in MORB. *Chemical Geology* **271**: 70-85.
- Asimow, P.D. and Ghiorso, M.S. (1998). Algorithmic modifications extending MELTS to calculate subsolidus phase relations. *Amer. Mineral.* **83**: 1127-1131.

- Asimow P.D. and Langmuir C.H. (2003) The importance of water to oceanic mantle melting regimes. *Nature* **421**, 815-820.
- Asimow P.D., Hirschmann M.M., and Stolper E.M. (2001) Calculation of peridotite partial Melting from thermodynamic models of minerals and melts, IV. Adiabatic decompression and the composition and mean properties of mid-ocean ridge basalts. *J. Petrol.* **42**, 963-998.
- Asimow, P.D., Dixon, J.E. and Langmuir, C.H. (2004) A hydrous melting and fractionation model for mid-ocean ridge basalts: Application to the Mid-Atlantic Ridge near the Azores. *Geochem. Geophys. Geosyst.* **5**: Q01E16 doi:10.1029/2003GC000568.
- Batiza R. and Vanko D. (1984) Petrology of young Pacific seamounts. *J. Geophys. Res.* **89**, 11235-11260.
- Batiza, R. (1984) Inverse relationship between Sr isotope diversity and rate of oceanic volcanism has implications for mantle heterogeneity. *Nature* **309**: 440-441.
- Batiza, R. (1996) Magmatic segmentation of mid-ocean ridges: a review. In: MacLeod, C.J., Tyler, P.A. and Walker, C.L. (eds.) *Geological Society Special Publication* **103**: Tectonic, Magmatic, Hydrothermal and Biological Segmentation of Mid-Ocean Ridges. pp. 103-130. London: Geological Society of London.
- Behn, M.D., Conrad, C.P. and Silver, P.G. (2004) Detection of upper mantle flow associated with the African Superplume. *Earth Planet. Sci. Lett.* **224**: 259-274.
- Bergmanis, E.C., Sinton, J. and Rubin, K.H. (2007) Recent eruptive history and magma reservoir dynamics on the southern East Pacific Rise at 17°30'S. *Geochem. Geophys. Geosyst.* **8**: Q12O06 doi: 10.1029/2007gc001742.
- Bowen, N.L. (1928) *The Evolution of the Igneous Rocks*. Princeton: Princeton University Press, Princeton.
- Boyet, M. and Carlson, R.W. (2005) ¹⁴²Nd evidence for early (>4.53 Ga) global differentiation of the silicate Earth. *Science* **309**: 576-581.
- Canales J. P., Detrick R. S., Bazin S, Harding A. J., and Orcutt J. A. (1998) Off-axis crustal thickness across and along the East Pacific Rise within the MELT area. *Science* **280**: 1218–1221.
- Carbotte, S. M., Detrick, R. S., Harding, A., Canales, J. P., Babcock, J., Kent, G., Van Ark, E., Nedimovic, M., and Diebold, J. (2006) Rift topography linked to magmatism at the intermediate spreading Juan de Fuca Ridge. *Geology* **34**: 209-212.

- Caro, G. and Bourdon, B. (2010) Non-chondritic Sm/Nd ratio in the terrestrial planets: Consequences for the geochemical evolution of the mantle crust system. *Geochim. Cosmochim. Acta* **74**: 3333-3349.
- Castillo, P. R., Klein, E., Bender, J., Langmuir, C., Shirey, S., Batiza, R., and White, W. (2000) Petrology and Sr, Nd and Pb isotope geochemistry of mid-ocean ridge basalt glasses from the 11°45'N to 15°00'N segment of the East Pacific Rise. *Geochem. Geophys. Geosyst.* **1**: doi: 1999GC000024.
- Christeson, G.L., McIntosh, K.D. and Karson, J.A. (2007) Inconsistent correlation of seismic layer 2a and lava layer thickness in oceanic crust. *Nature* **445**: 418-421.
- Cogley, J.G. (1984) Continental margins and the extent and number of the continents. *Rev. Geophys. Space Phys.* **22**: 101-122.
- Cogné, J.-P., Humler, E. and Courtillot, V. (2006) Mean age of oceanic lithosphere drives eustatic sea-level change since Pangea breakup. *Earth Planet. Sci. Lett.* **245**: 115-122.
- Danyushevsky, L. V. (2001) The effect of small amounts of H₂O on crystallisation of mid-ocean ridge and backarc basin magmas. *J. Volcan. Geotherm. Res.* **110**: 265-280.
- Darbyshire F. A., White R. S., and Priestley K. F. (2000) Structure of the crust and uppermost mantle of Iceland from a combined seismic and gravity study. *Earth Planet. Sci. Lett.* **181**: 409-428.
- Davis, A. S., Clague, D. A. and White, W. M. (1998) Geochemistry of Basalt from Escanaba Trough: Evidence for Sediment Contamination. *J. Petrol.* **39**: 841-858.
- Detrick, R. S., Buhl, P., Vera, E., Mutter, J., Orcutt, J., Madsen, J., and Brocher, T. (1987) Multi-channel seismic imaging of a crustal magma chamber along the East Pacific Rise. *Nature*. **326**, 35-41.
- Detrick R. S., Sinton J. M., Ito G., Canales J. P., Behn M., Blacic T., Cushman B., Dixon J. E., Graham D. W., and Mahoney J. J. (2002) Correlated geophysical, geochemical, and volcanological manifestations of plume-ridge interaction along the Galapagos spreading center. *Geochem. Geophys. Geosyst.* **3**, doi:10.1029/2002GC000350
- Dick, H. J.B., Fisher, R.L. and Bryan, W.B. (1984) Mineralogic variability of the uppermost mantle along mid-ocean ridges. *Earth Planet. Sci. Lett.* **69**: 88-106.
- Dick, H. J. B., Lin, J. and Schouten, H. (2003) An ultraslow-spreading class of ocean ridge. *Nature*, **426**: 405-412.

- Donnelly, K. E., Goldstein, S. L., Langmuir, C. H., and Spiegelman, M. (2004) Origin of enriched ocean ridge basalts and implications for mantle dynamics. *Earth Planet. Sci. Lett.* **226**: 347-366.
- Dupré, B. and Allègre, C.J. (1983) Pb-Sr isotope variations in Indian Ocean basalts and mixing phenomena. *Nature* **303**: 142-146.
- Edwards, M.H., Kurras, G. J., Tolstoy, M., Bohnenstiehl, D. R., Coakley, B. J., and Cochran, J. R. (2001) Evidence of recent volcanic activity on the ultraslow-spreading Gakkel ridge. *Nature*, **409**: 808-812.
- Embley, R.W. and Chadwick, W.W., Jr. (1994) Volcanic and hydrothermal processes associated with a recent phase of seafloor spreading at the northern Cleft segment: Juan de Fuca Ridge. *J. Geophys. Res.* **99**: 4741-4760.
- Embley, R.W., Chadwick, W.W., Perfit, M.R., Smith, M.C. and Delaney, J.R. (2000) Recent eruptions on the CoAxial segment of the Juan de Fuca Ridge: Implications for mid-ocean ridge accretion processes. *J. Geophys. Res.* **105**: 16501-16525.
- Engel, A. E. J., Engel, C. G. and Havens, R. G. (1965) Chemical characteristics of oceanic basalts and the upper mantle. *Geol. Soc. Amer. Bull.* **76**: 719-734.
- Fisk, M.R., Schilling, J.G. and Sigurdsson, H. (1980) An experimental investigation of Iceland and Reykjanes Ridge tholeiites: I. Phase relations. *Contrib. Mineral. Petrol.* **74**: 361-374.
- Flower, M.F.J. (1980) Thermal and kinematic control on ocean-ridge magma fractionation: contrasts between Atlantic and Pacific spreading axes. *J. Geol. Soc. Lond.* **138**: 695-712.
- Fowler C. M. R. and Keen C. E. (1979) Oceanic crustal structure: Mid-Atlantic Ridge at 45 degrees N. *Geophys. J. Roy. Astronom. Soc.* **56**: 219-226.
- Fornari D. J., Perfit M. R., Allan J. F., Batiza R., Haymon R., Barone A., Ryan W. B. F., Smith J. Srinken J., and Puckman M. (1988) Geochemical and structural studies of the Lamont seamounts: seamounts as indicators of mantle processes. *Earth Planet. Sci. Lett.* **89**: 63-83.
- Fornari, D.J., Haymon, R.M., Perfit, M.R., Gregg, T.K.P. and Edwards, M.H., (1998) Axial summit trough of the East Pacific Rice 9°–10°N: Geological characteristics and evolution of the axial zone on fast spreading mid-ocean ridge. *J. Geophys. Res.* **103**: 9827-9855.
- Forsyth, D. and the MELTS Seismic Team (1998) Imaging the Deep Seismic Structure Beneath a Mid-Ocean Ridge: The MELT Experiment. *Science*, **280**: 1215-1218.

- Fox, C.G., Chadwick, W.W. and Embley, R.W. (2001) Direct observation of a submarine volcanic eruption from a sea-floor instrument caught in a lava flow. *Nature*, **412**: 727-729.
- Fryer, P., Taylor, B., Langmuir, C. H., and Hochstaedter, A. G. (1990) Petrology and geochemistry of lavas from the Sumisu and Torishima backarc rifts. *Earth Planet. Sci. Lett.* **100**: 161-178.
- Galer, S.J.G. and O'Nions, R.K. (1985) Residence time of thorium, uranium and lead in the mantle with implications for mantle convection. *Nature* **316**: 778-782.
- Ghiorso, M.S. and Sack, R.O. (1995) Chemical mass transfer in magmatic processes IV. A revised and internally consistent thermodynamic model for the interpolation and extrapolation of liquid-solid equilibria in magmatic systems at elevated temperatures and pressures. *Contrib. Mineral. Petrol.* **119**: 197-212.
- Ghiorso, M.S., Hirschmann, M.M., Reiners, P.W. and Kress, V.C. (2002) The pMELTS: a revision of MELTS for improved calculation of phase relations and major element partitioning related to partial melting of the mantle to 3 GPa. *Geochem. Geophys. Geosyst.* **3**: doi: 10.1029/2001GC000217.
- Gill, J. B. (1976) Composition and age of Lau Basin and Ridge volcanic rocks: Implications for evolution of an interarc basin and remnant arc. *Geol. Soc. Am. Bull.* **87**: 1384-1395.
- Graham D., Zindler A., Kurz M., Jenkins W., Batiza R., and Staudigel H. (1988) He, Pb, Sr, and Nd isotope constraints on magma genesis and mantle heterogeneity beneath young Pacific seamounts. *Contrib. Mineral. Petrol.* **99**, 446-463.
- Grove, T.L., Kinzler, R.J. and Bryan, W.B. (1992) Fractionation of mid-ocean ridge basalt (MORB). Mantle flow and melt generation at mid-ocean ridges. In: J. Phipps Morgan, D.K. Blackman and J.M. Sinton (Eds) *Geophysical Monograph* **71**: Mantle Flow and Melt Generation at Mid-Ocean Ridges. pp: 281–310 Washington: AGU.
- Gu, Y.J., Webb, S.C., Lerner-Lam, A. and Gaherty, J.B. (2005) Upper mantle structure beneath the eastern Pacific Ocean ridges. *J. Geophys. Res.* **110**: B06305.
- Hart, S.R. (1984) The DUPAL anomaly: A large-scale isotopic mantle anomaly in the Southern Hemisphere. *Nature* **309**: 753-757.
- Hart, S.R., Schilling, J.G. and Powell, J.L. (1973) Basalts from Iceland and along the Reykjanes Ridge: Sr isotope geochemistry. *Nature Physical Science* **246**: 104-107.

- Hawkins, J.W. and Melchior, J.T. (1985) Petrology of Mariana Trough and Lau Basin basalts. *J. Geophys. Res.* **90**: 431-468.
- Haymon, R.M., Fornari, D. J., Von Damm, K. L., Lilley, M. D., Perfit, M. R., Edmond, J. M., Shanks Iii, W. C., Lutz, R. A., Grebmeier, J. M., Carbotte, S., Wright, D., McLaughlin, E., Smith, M., Beedle, N., and Olson, E. (1993) Volcanic eruption of the mid-ocean ridge along the East Pacific Rise crest at 9°45-52'N: Direct submersible observations of seafloor phenomena associated with an eruption event in April, 1991. *Earth Planet. Sci. Lett.* **119**: 85-101.
- Hekinian R., Thompson G., and Bideau D. (1989) Axial and off-axial heterogeneity of basaltic rocks from the East Pacific Rise at 12°35'N-12°51'N and 11°26'N-11°30'N, *J. Geophys. Res.* **94**, 17437-17463.
- Herzberg, C. (2004) Partial Crystallization of Mid-Ocean Ridge Basalts in the Crust and Mantle. *J. Petrol.* 45: 2389-2405.
- Herzberg, C., Asimow, P.D., Arndt, N., Niu, Y., Leshner, C.M., Fitton, J.G., Cheadle, M.J. and Saunders, A.D. (2007) Temperatures in ambient mantle and plumes: Constraints from basalts, picrites, and komatiites. *Geochem. Geophys. Geosyst.* **8** doi: 10.1029/2006gc001390.
- Hess, H.H. (1962) History of ocean basins. In: Engel, A. E. J., James, H. L., and Leonard, B.F. (eds), *Petrologic studies: a volume in honor of A. F. Buddington*. pp. 599–620. Boulder, CO: Geological Society of America.
- Hewitt, I.J. and Fowler, A.C. (2009) Melt channelization in ascending mantle. *J. Geophys. Res.* **114**: B06210.
- Hofmann, A. W., and White, W. M. (1982) Mantle plumes from ancient oceanic crust: *Earth Planet. Sci. Lett.* **57**: 421-436.
- Hofmann, A.W. and White, W.M. (1983) Ba, Rb, and Cs in the Earth's mantle. *Z. Naturforsch.* **38**: 256-266.
- Hofmann, A.W. (1988) Chemical differentiation of the Earth: the relationship between mantle, continental crust, and oceanic crust. *Earth Planet. Sci Lett.* **90**: 297-314.
- Hofmann, A.W., Jochum, K.P., Seufert, M. and White, W.M. (1986) Nb and Pb in oceanic basalts: new constraints on mantle evolution. *Earth. Planet. Sci. Lett.* **79**: 33-45.
- Holmes, R. C., Tolstoy, M., Cochran, J. R., and Floyd, J. S. (2008) Crustal thickness variations along the Southeast Indian Ridge (100°–116°E) from 2-D body wave tomography: *Geochem. Geophys.*

- Geosyst.* **9**: Q12020, doi: 10.1029/2008gc002152.
- Hooft E. E. E., Detrick R. S., Toomey D. R., Collins J. A., and Lin J. (2000) Crustal thickness and structure along three contrasting spreading segments of the Mid-Atlantic Ridge, 33.5 degrees–3.5 degrees N. *J. Geophys. Res.* **105**: 8205–8226.
- Ito, E., White, W.M. and Goepel, C. (1987) The O, Sr, Nd and Pb isotope geochemistry of MORB. *Chem. Geol.* **62**: 157-176.
- Johnson K.T.M. and Dick H.J.B. (1992) Open system melting and temporal and spatial variation of peridotite and basalt at the Atlantis II fracture zone. *J. Geophys. Res.* **97**, 9219-9241.
- Jokat W., Ritzmann O., Schmidt-Aursch M. C., Drachev S., Gauger S., and Snow J. (2003) Geophysical evidence for reduced melt production on the Arctic ultraslow Gakkel mid-ocean ridge. *Nature* **423**: 962–965.
- Jull, M., Kelemen, P.B. and Sims, K. (2002) Consequences of diffuse and channelled porous melt migration on uranium series disequilibria. *Geochim. Cosmochim. Acta* **66**: 4133-4148.
- Karson, J. A., Klein, E. M., Hurst, S. D., Lee, C. E., Rivizzigno, P. A., Curewitz, D., Morris, A. K., and the Hess Deep '99 Scientific Party (2002) Structure of uppermost fast-spread oceanic crust exposed at the Hess deep Rift: Implications for subaxial processes at the East Pacific Rise. *Geochem. Geophys. Geosyst.* **3**, doi:10.1029/2001gc000155.
- Karson, J.A. (2002) Geologic structure of the uppermost oceanic crust created at fast- to intermediate-rate spreading centers. *Ann. Rev. Earth Planet. Sci.* **30**: 347-384.
- Karsten J. L., Delaney J. R., Rhodes J. M., and Lias R. A. (1990) Spatial and temporal evolution of magmatic systems beneath the Endeavour Segment, Juan de Fuca Ridge: Tectonic and petrologic constraints. *J. Geophys. Res.* **95**, 19235-19256.
- Kelemen, P.B., Shimizu, N. and Salters, V.J.M. (1995) Extraction of mid-ocean-ridge basalt from the upwelling mantle by focused flow of melt in dunite channels. *Nature* **375**: 747-753.
- Kent, G.M., Harding, A.J. and Orcutt, J.A. (1990) Evidence for a smaller magma chamber beneath the East Pacific Rise at 9° 30'N. *Nature* **344**: 650-652.
- Kinzler R. J. and Grove T. L. (1992) Primary magmas of mid-ocean ridge basalts 2. Applications. *J. Geophys. Res.* **97**: 6907-6926.
- Klein, E. M. and Langmuir, C. H. (1987) Ocean ridge basalt chemistry, axial depth, crustal thickness and temperature variations in the mantle. *J. Geophys. Res.* **92**: 8089-8115.

- Klein, E. M., Langmuir, C. H., Zindler, A. and Staudigel, B.H. (1988) Isotope evidence of a mantle convection boundary at the Australian-Antarctic Discordance. *Nature* **333**: 632-629.
- Klingelhöfer F. Géli L., Matias L., Steinsland N., and Mohr J. (2000) Crustal structure of a super-slow spreading centre: a seismic refraction study of Mohns Ridge, 72°N. *Geophys. J. Int.* **141**: 509–526.
- Kodaira S., Mjelde R., Gunnarsson K., Shirobara H., and Shimamura H. (1997) Crustal structure of the Kolbeinsey Ridge, North Atlantic, obtained by use of ocean bottom seismographs. *J. Geophys. Res.* **102**: 3131–3151.
- Koppers, A. A. P., Staudigel, H. and Duncan, R. A. (2003) High-resolution $^{40}\text{Ar}/^{39}\text{Ar}$ dating of the oldest oceanic basement basalts in the western Pacific basin. *Geochem. Geophys. Geosyst.* 4: doi: 10.1029/2003gc000574.
- Lachenbruch, A. H. (1976) Dynamics of a passive spreading center. *J. Geophys. Res.* **81**, 1883-1902.
- Langmuir, C. H., Bender, J. F., and Batiza, R. (1986) Petrologic and tectonic segmentation of the East Pacific Rise between 5°30'–14°30'N. *Nature* **322**, 422-429.
- Langmuir, C. H. and Hanson, G. N. (1980) An evaluation of major element heterogeneity in the mantle sources of basalts. *Phil. Trans. R. Soc. Lond.*, **297**, 383-407.
- Langmuir, C. H., Klein, E. M., and Plank, T. (1992) Petrological systematics of mid-ocean ridge basalts: constraints on melt generation beneath oceanic ridges, In Morgan, J. P., Blackman, D. K., and Sinton, J. M. (eds) *Geophysical Monograph 71*: Mantle flow and melt generation at mid-ocean ridges. p. 183-280. AGU: Washington.
- Laubier, M., Schiano, P., Doucelance, R., Ottolini, L. and Laporte, D. (2007) Olivine-hosted melt inclusions and melting processes beneath the FAMOUS zone (Mid-Atlantic Ridge). *Chem. Geol.* **240**: 129-150.
- Liang, Y., Schiemenz, A., Hesse, M.A., Parmentier, E.M. and Hesthaven, J.S. (2010) High-porosity channels for melt migration in the mantle: Top is the dunite and bottom is the harzburgite and lherzolite. *Geophys. Res. Lett.* **37**: L15306 doi: 10.1029/2010gl044162.
- Lyubetskaya, T. and Korenaga, J. (2007) Chemical composition of Earth's primitive mantle and its variance: 1. Method and results. *J. Geophys. Res.* **112**: B03211 doi: 10.1029/2005jb004223.

- McClain K. J. and Lewis B. T. R. (1982) Geophysical evidence for the absence of a crustal magma chamber under the northern Juan de Fuca Ridge: a contrast with ROSE results *J. Geophys. Res.* **87**: 8477–8489.
- McDonough, W.F. and Sun, S.-S. (1995) The composition of the Earth. *Chem. Geol.* **120**: 223-253.
- Macdonald, K.C. et al. (1988) A new view of the mid-ocean ridge from the behaviour of ridge-axis discontinuities. *Nature* **335**: 217-225.
- Macdonald, K.C., Scheirer, D.S. and Carbotte, S.M. (1991) Mid-ocean ridges: Discontinuities, segments and giant cracks. *Science* **253**: 986-994.
- McKenzie D. and Bickle M. J. (1988) The volume and composition of melt generated by extension of the lithosphere. *J. Petrol.* **29**, 625-679.
- Meyzen, C.M., Blichert-Toft, J., Ludden, J. N., Humler, E., Mevel, C. and Albarede, F. (2007) Isotopic portrayal of the Earth's upper mantle flow field. *Nature* **447**: 1069-1074.
- Michael P. J. and Bonatti E. (1985) Peridotite composition from the North Atlantic: Regional and tectonic variations and implications for partial melting. *Earth Planet. Sci. Lett.* **73**: 91-104.
- Michael, P. J. and Cornell, W. C. (1998) Influence of spreading rate and magma supply on crystallization and assimilation beneath mid-ocean ridges: Evidence from chlorine and major element chemistry of mid-ocean ridge basalts. *J. Geophys. Res.* **103**: 18325-18356.
- Michael, P. J. et al. (2003) Magmatic and amagmatic seafloor generation at the ultraslow-spreading Gakkel ridge, Arctic Ocean. *Nature*, **423**: 956-961.
- Morgan, J. P. and Chen, Y. J. (1993) The genesis of oceanic crust: magma injection, hydrothermal circulation, and crustal flow. *J. Geophys. Res.* **98**: 6283-6297.
- Muehlenbachs, K. and Byerly, G. (1982) ¹⁸O enrichment of silicic magmas caused by crystal fractionation at the Galapagos Spreading Center. *Contrib. Mineral. Petrol.* **79**: 76-79.
- Muehlenbachs, K. and Clayton, R. N. (1972) Oxygen isotope studies of fresh and weathered submarine basalts. *Can. J. Earth Sci.* **9**: 172-184.
- Muir, E. D. and Tilley, C. E. (1964) Basalts from the northern part of the rift zone of the Mid-Atlantic Ridge. *J. Petrol.* **5**: 409-434.
- Muller M. R., Minshull T. A., Timothy A., and White R. S. (1999) Segmentation and melt supply at the Southwest Indian Ridge. *Geology (Boulder)* **27**: 867–870.

- Müller, R. D., Sdrolias, M., Gaina, C., Steinberger, B. and Heine, C. (2008a) Long-Term Sea-Level Fluctuations Driven by Ocean Basin Dynamics. *Science* **319**: 1357-1362.
- Müller, R. D., Sdrolias, M., Gaina, C. and Roest, W. R. (2008b) Age, spreading rates, and spreading asymmetry of the world's ocean crust. *Geochem. Geophys. Geosyst.* **9**: Q04006 doi: 10.1029/2007gc001743.
- Navin D. A., Peirce C., and Sinha M. C. (1998) The RAMESSES experiment II. Evidence for accumulated melt beneath a slow spreading ridge from wide-angle refraction and multichannel reflection seismic profiles. *Geophys. J. Int.* **135**: 746–772.
- Newsom, H. E., White, W. M., Jochum, K. P. and Hofmann, A. W. (1986) Siderophile and chalcophile element abundances in oceanic basalts, Pb isotope evolution and growth of the Earth's core. *Earth Planet. Sci. Lett.* **80**: 299-313.
- Nielsen R. L., Crum J., Bourgeois R., Hascall K., Forsythe L. M., Fisk M. R., and Christie D. M. (1995) Melt inclusions in high-An plagioclase from the Gorda Ridge: an example of the local diversity of MORB parent magmas. *Contrib. Mineral. Petrol.* **122**, 34–50.
- Niu Y. and Batiza R. (1997) Trace element evidence from seamounts for recycled oceanic crust in the eastern Pacific mantle. *Earth Planet. Sci. Lett.* **148**, 471-483.
- Niu, Y. and O'Hara, M. J. (2008) Global Correlations of Ocean Ridge Basalt Chemistry with Axial Depth: a New Perspective. *J. Petrol.* **49**: 633-664.
- Niu, Y. and O'Hara, M. J. (2009) MORB mantle hosts the missing Eu (Sr, Nb, Ta and Ti) in the continental crust: New perspectives on crustal growth, crust-mantle differentiation and chemical structure of oceanic upper mantle. *Lithos* **112**: 1-17.
- O'Hara, M. J. (1968) The bearing of phase equilibria studies in synthetic and natural systems on the origin and evolution of basic and ultrabasic rocks. *Earth Sci. Rev.*, **4**: 69-133.
- O'Neill, H. S. C. and Palme, H. (2008) Collisional erosion and the non-chondritic composition of the terrestrial planets. *Philos. Trans. R. Soc. London*, **366A**: 4205-4238.
- Oxburgh E.R. (1965) Volcanism and mantle convection. *Philos. Trans. R. Soc. London* **258A**, 142-144.
- Oxburgh E.R. (1980) Heat flow and magma genesis. In *Physics of Magmatic Processes* Hargraves, R. B. (ed.) pp. 161-199. Princeton: Princeton University Press.
- Perfit, M. R. and Chadwick, W. W. (1998) Magmatism at mid-ocean ridges: Constraints from volcanological and geochemical investigations. In: Buck, W.R., Delaney, P.T. and Karson,

- J.A. (eds), *Geophysical Monograph* **106**: Faulting and Magmatism at Mid-Ocean Ridges. pp. 59-115. Washington: AGU.
- Phipps Morgan, J. and Chen, Y. J. (1993) The genesis of oceanic crust; magma injection, hydrothermal circulation, and crustal flow. *J. Geophys. Res.* **98**: 6283-6297.
- Plank, T. and Langmuir, C. H. (1992) Effects of the melting regime on the composition of oceanic crust. *J. Geophys. Res.* **97**: 19749-19770.
- Putirka, K. D., Perfit, M., Ryerson, F. J., and Jackson, M. G. (2007) Ambient and excess mantle temperatures, olivine thermometry, and active vs. passive upwelling. *Chem. Geol.*, **241**: 177-206.
- Pyle, D., Christie, D.M. and Mahoney, J.J. (1992) Resolving an isotopic boundary within the Australian-Antarctic Discordance. *Earth Planet. Sci. Lett.* **112**: 161-178.
- Rabinowicz, M. and Toplis, M.J. (2009) Melt Segregation in the Lower Part of the Partially Molten Mantle Zone beneath an Oceanic Spreading Centre: Numerical Modelling of the Combined Effects of Shear Segregation and Compaction. *J. Petrol.* **50**: 1071-1106.
- Reynolds J. R., Langmuir C. H., Bender J. F., Kastens K. A., and Ryan W. B. F. (1992) Spatial and temporal variability in the geochemistry of basalt from the East Pacific Rise. *Nature* **359**: 493-499.
- Rowley, D. B. (2002) Rate of plate creation and destruction: 180 Ma to present. *Geol. Soc. America Bull.* **114**: 927-933.
- Rowley, D. B. (2008) Extrapolating Oceanic Age Distributions: Lessons from the Pacific Region. *J. Geology* **116**: 587-598.
- Rubin, K. H. and Sinton, J.M. (2007) Inferences on mid-ocean ridge thermal and magmatic structure from MORB compositions. *Earth Planet. Sci. Lett.* **260**: 257-276.
- Rubin, K. H., Smith, M. C., Bergmanis, E. C., Perfit, M. R., Sinton, J. M., and Batiza, R. (2001) Geochemical heterogeneity within mid-ocean ridge lava flows: insights into eruption, emplacement and global variations in magma generation. *Earth Planet. Sci. Lett.* **188**: 349-367.
- Rubin, K. H., Sinton, J. M., MacLennan, J. and Hellebrand, E. (2009) Magmatic filtering of mantle compositions at mid-ocean-ridge volcanoes. *Nature Geosci.* **2**: 321-328.
- Schilling, J-G. (1973) Iceland mantle plume: geochemical study of the Reykjanes Ridge. *Nature* **242**: 565-571.

- Schilling, J-G. (1975) Rare-earth variations across 'normal segments' of the Reykjanes Ridge, 60°-53°N, mid-Atlantic ridge, 29°S, and East Pacific Rise, 2°-19°S, and evidence on the composition of the underlying low-velocity layer. *J. Geophys. Res.* **80**: 1459-1473.
- Schilling, J-G. (1985) Upper mantle heterogeneities and dynamics. *Nature* **314**: 62-67.
- Schilling, J-G., Zajac, M., Evans, R., Johnston, T., White, W. M., Devine, J. D. and Kingsley, R. (1983) Petrologic and geochemical variations along the Mid-Atlantic Ridge from 29°N to 73°N. *Am. J. Sci.* **283**: 510-586.
- Scott, D. R. and Stevenson, D. J. (1989) A self-consistent model of melting, magma migration, and buoyancy-driven circulation beneath mid-ocean ridges. *J. Geophys. Res.* **94**: 2973-2988.
- Shank, T. et al. (2003) Deep Submergence Synergy: Alvin and ABE Explore the Galápagos Rift at 86° W. *Eos Trans. AGU*, **41**(84): 425.
- Shen Y. and Forsyth D. W. (1995) Geochemical constraints on initial and final depth of melting beneath mid-ocean ridges. *J. Geophys. Res.* **100**, 2211-2237.
- Shimizu N. (1998) The geochemistry of olivine-hosted melt inclusions in a FAMOUS basalt ALV519-4-1. *Phys. Earth Planet. Int.* **107**, 183-201.
- Singh, S.C., Crawford, W. C., Carton, H., Seher, T., Combier, V., Cannat, M., Pablo Canales, J., Dusunur, D., Escartin, J., and Miguel Miranda, J. (2006) Discovery of a magma chamber and faults beneath a Mid-Atlantic Ridge hydrothermal field. *Nature* **442**: 1029-1032.
- Sinton C.W., Christie D.M., Coombs V.L., Nielsen R.L., and Fisk M.R. (1993) Near primary melt inclusions in anorthite phenocrysts from the Galapagos Platform. *Earth Planet. Sci. Lett.* **119**: 527-537.
- Sinton J. M. and Detrick R. S. (1992) Mid-ocean ridge magma chambers. *J. Geophys. Res.* **97**: 197-216.
- Sinton J. M., Smaglik S. M., and Mahoney J. J. (1991) Magmatic processes at superfast spreading mid-ocean ridges: glass compositional variations along the East Pacific Rise 13-23 S. *J. Geophys. Res.* **96**: 6133-6155.
- Sinton, J. and Fryer, P. (1987) Mariana Trough lavas from 18°N: implications for the origin of back-arc basin basalts. *J. Geophys. Res.* **92**: 12782-12802.
- Sinton, J. M., Ford, L. L., Chappell, B. and McCulloch, M. T. (2003) Magma Genesis and Mantle Heterogeneity in the Manus Back-Arc Basin, Papua New Guinea. *J. Petrol.* **44**: 159-195.

- Smallwood J. R. and White R. S. (1998) Crustal accretion at the Reykjanes Ridge, 61 degrees–62 degrees N. *J. Geophys. Res.* **103**: 5185–5201.
- Smith, M. C., Perfit, M. R., Fornari, D. J., Ridley, W. I., Edwards, M. H., Kurras, G. J., Von Damm, K. L. (2001) Magmatic processes and segmentation at a fast spreading mid-ocean ridge: Detailed investigation of an axial discontinuity on the East Pacific Rise crest at 9°37' N. *Geochem. Geophys. Geosyst.* **2** doi:10.1029/2000gc000134 .
- Sobolev A.V. and Shimizu N. (1993) Ultra-depleted primary melt included in an olivine from the Mid-Atlantic Ridge. *Nature* **363**, 151-154.
- Sours-Page R., Johnson K.T.M., Nielsen R.L., and Karsten J.L. (1999) Local and regional variation of MORB parent magmas; evidence from melt inclusions from the Endeavour Segment of the Juan de Fuca Ridge. *Contrib. Mineral. Petrol.* **134**: 342-363.
- Spiegelman M. and McKenzie D. (1987) Simple 2-D models for melt extraction at mid-ocean ridges and island arcs. *Earth Planet. Sci. Lett.* **83**: 137-152.
- Spiegelman, M. and Kelemen, P. B. (2003) Extreme chemical variability as a consequence of channelized melt transport. *Geochem. Geophys. Geosyst.* **4**: doi: 10.1029/2002gc000336.
- Sun, S.-S. and McDonough, W.F. (1989) Chemical and isotopic systematics of oceanic basalts: implications for mantle composition and processes. In: Saunders, A. D. and Norry, M. J. (eds) *Geological Society Special Publication* **42**: Magmatism in the Ocean Basins. pp. 313-345 London: Geological Society of London.
- Tarney, J., Saunders, A.D. and Weaver, S.D. (1977) Geochemistry of volcanic rocks from the island arcs and marginal basins of the Scotia Sea region. In: Talwani, M. and Pitman, W. C. (eds), *Island Arcs, Deep Sea Trenches, and Backarc Basins*. pp. 367-377. Washington: AGU.
- Tarney, J., Saunders, A. D., Mathey, D. P., Wood, D. A. and Marsh, N. G. (1981) Geochemical aspects of back-arc spreading in the Scotia Sea and western Pacific. *Philos. Trans. R. Soc. London* **300A**: 263-285.
- Tolstoy, M. et al. 2006. A Sea-Floor Spreading Event Captured by Seismometers. *Science* **314**: 1920-1922.
- Toomey, D. R., Purdy, G. M., Solomon, S. C. and Wilcock, W. S. D. (1990) The three-dimensional seismic velocity structure of the East Pacific Rise near latitude 9°30'N. *Nature*, **347**: 639-645.

- Umino, S. Crispini, L., Tartarotti, P., Teagle, D. A. H., Alt, J. C., Miyashita, S., and Banerjee, N. R. (2008) Origin of the sheeted dike complex at superfast spread East Pacific Rise revealed by deep ocean crust drilling at Ocean Drilling Program Hole 1256D. *Geochem. Geophys. Geosyst.* **9**: Q06O08 doi: 10.1029/2007gc001760.
- Vallier, T. L., Jenner, G. A., Frey, F. A., Gill, J. B., Davis, A. S., Volpe, A. M., Hawkins, J. W., Morris, J. D., Cawood, P. A., Morton, J. L., Scholl, D. W., Rautenschlein, M., White, W. M., Williams, R. W., Stevenson, A.J. and White, L. D. (1991) Subalkaline andesite from Valu Fa Ridge, a back-arc spreading center in southern Lau Basin: petrogenesis, comparative chemistry and tectonic implications. *Chem. Geol.* **91**: 227-256.
- Van Ark, E. M., Detrick, R. S., Canales, J. P., Carbotte, S. M., Harding, A. J., Kent, G. M., Nedimovic, M. R., Wilcock, W. S. D., Diebold, J. B., and Babcock, J. M. (2007) Seismic structure of the Endeavour Segment, Juan de Fuca Ridge: Correlations with seismicity and hydrothermal activity. *J. Geophys. Res.* **112**: B02401.
- Villiger, S., Müntener, O. and Ulmer, P. (2007) Crystallization pressures of mid-ocean ridge basalts derived from major element variations of glasses from equilibrium and fractional crystallization experiments. *J. Geophys. Res.* **112**: B01202.
- von Bargen, N. and Waff, H.S. (1986) Permeabilities, interfacial areas and curvatures of partially molten systems: results of numerical computations of equilibrium microstructures. *J. Geophys. Res.* **91**: 9261-92756.
- Wark, D. A., Williams, C. A., Watson, E. B. and Price, J. D. (2003) Reassessment of pore shapes in microstructurally equilibrated rocks, with implications for permeability of the upper mantle. *J. Geophys. Res.* **108**: doi: 10.1029/2001jb001575.
- White, R.S., McKenzie, D. and O'Nions, R.K. (1992) Oceanic Crustal Thickness From Seismic Measurements and Rare Earth Element Inversions. *J. Geophys. Res.* **97**: 19683-19715.
- White, R. S., Minshull, T. A., Bickle, M. J. and Robinson, C. J. (2001) Melt Generation at Very Slow-Spreading Oceanic Ridges: Constraints from Geochemical and Geophysical Data. *J. Petrol.* **42**: 1171-1196.
- White, W.M. (2010) Oceanic Island Basalts and Mantle Plumes: The Geochemical Perspective. *Ann. Rev. of Earth Planet. Sci.* **38**: 133-160.
- White, W. M., Hofmann, A. W., and Puchelt, H. (1987) Isotope geochemistry of Pacific mid-ocean ridge basalts. *J. Geophys. Res.* **92**: 4881-4893.

- White, W. M., and Schilling, J.-G. (1978) The nature and origin of geochemical variation in Mid-Atlantic Ridge basalts from the Central North Atlantic: *Geochim. Cosmochim. Acta* **42**: 1501-1516.
- Yamamoto, M., Morgan, J.P. and Morgan, W.J. (2007) Global plume-fed asthenosphere flow II. Application to the geochemical segmentation of ridges. In: Foulger, G. R. and Jurdy, D. M. (eds) *Geological Society of America Special Paper* **430**: Plates, plumes, and planetary processes. pp. 189-208. Boulder, CO: Geological Society of America.
- Yang, Y., Forsyth, D.W. and Weeraratne, D.S. (2007) Seismic attenuation near the East Pacific Rise and the origin of the low-velocity zone. *Earth Planet. Sci. Lett.* **258**: 260-268.
- Zhang, G.-L., Zeng, Z.-G., Beier, C., Yin, X.-B. and Turner, S. (2010) Generation and evolution of magma beneath the East Pacific Rise: Constraints from U-series disequilibrium and plagioclase-hosted melt inclusions. *J. Volcan. Geotherm Res.* **193**: 1-17.

Figures

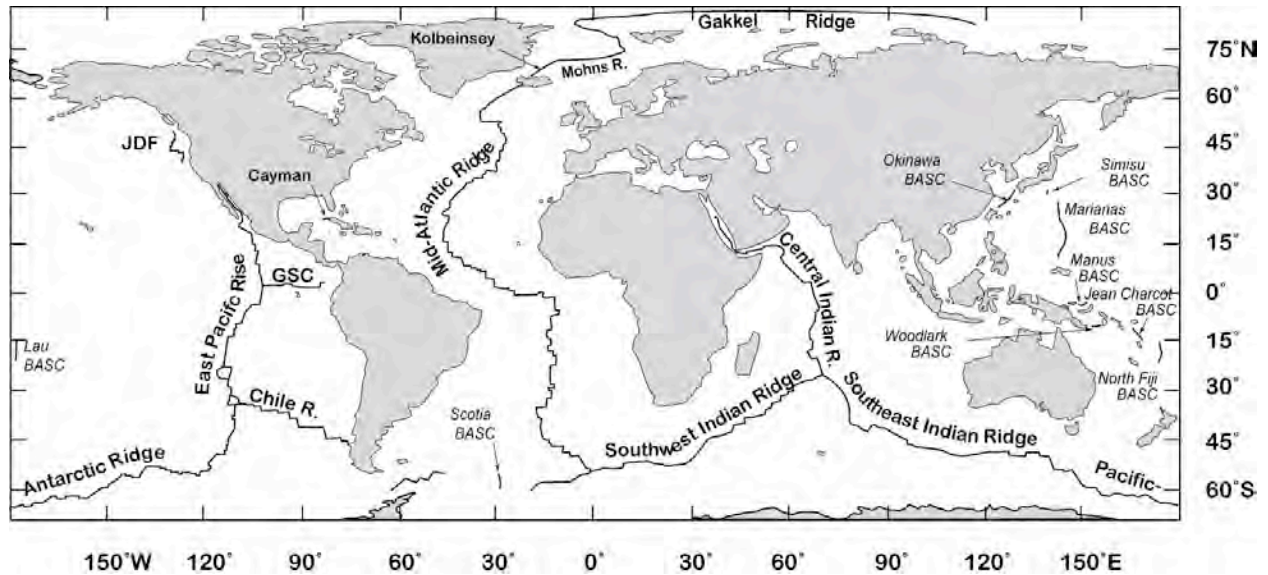


Figure 1. Map of the Global Mid-ocean Ridge System. Names of back-arc basin spreading centers are shown in italics.

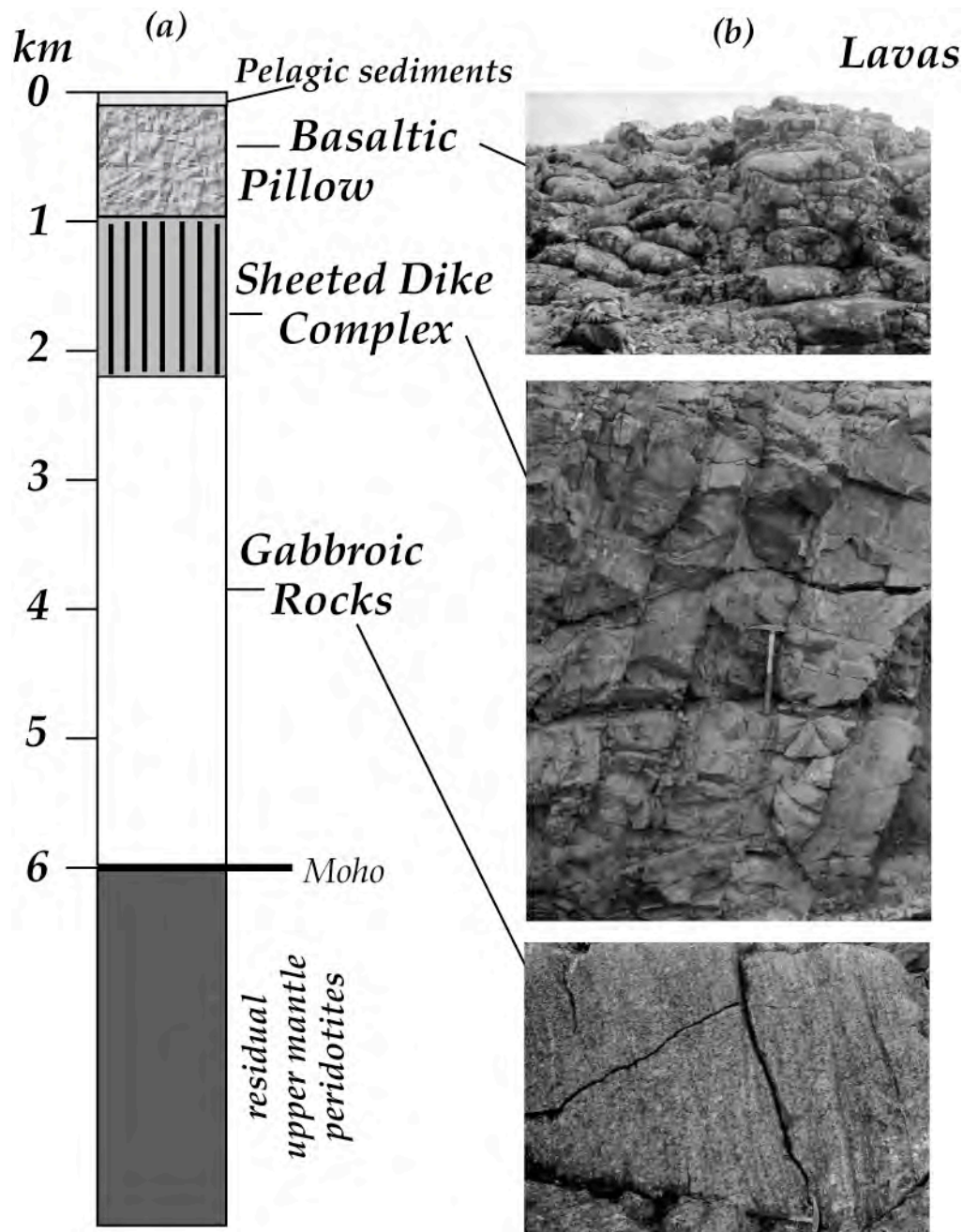


Fig. 2 a) Generalized internal structure and interpretation of the oceanic crust derived from studies of ophiolite complexes and interpretations of marine seismic and geologic data. b) Outcrop photographs of crustal rocks from ophiolites; top: pillow lavas, Macquarie Island; middle: sheeted dike complex, Oman; bottom: gabbroic rocks, Bay of Islands. After Karson (2002).

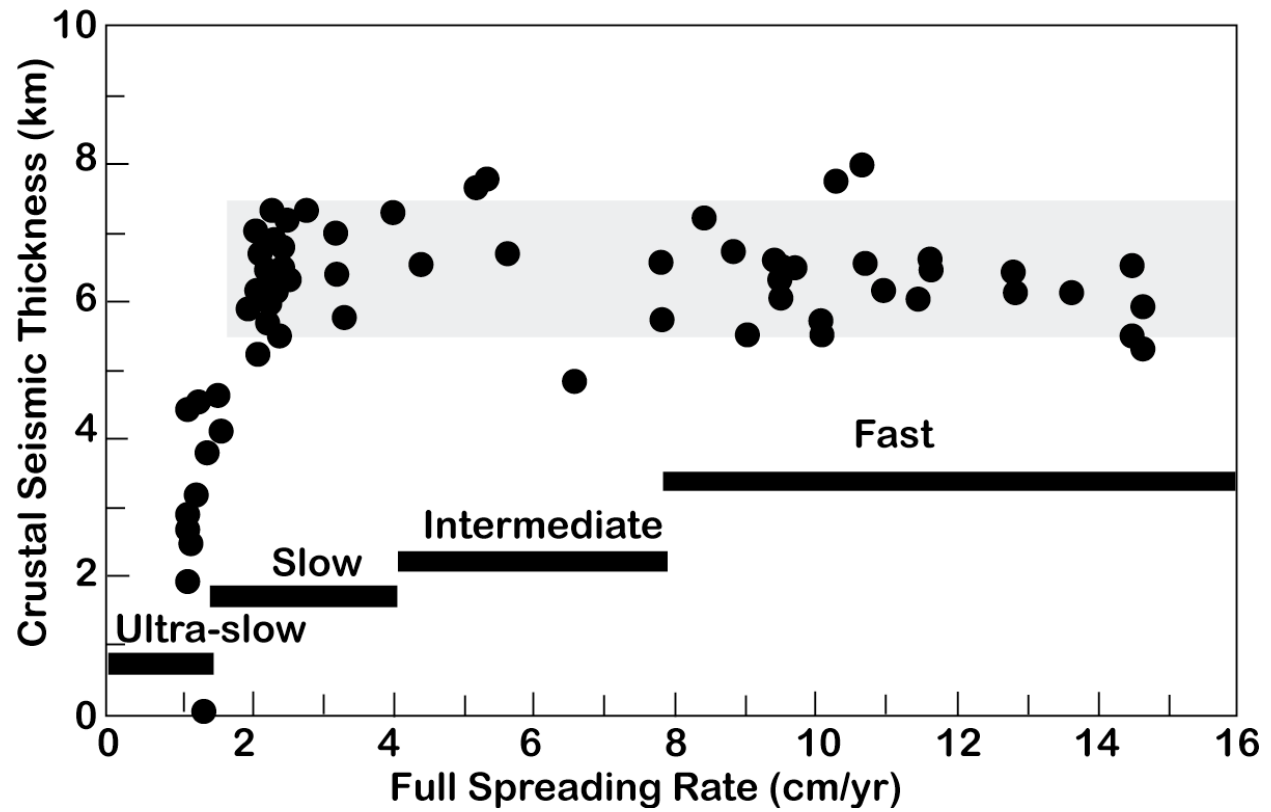


Figure 3. Crustal seismic thickness as a function of full spreading rate. Crustal thickness appears to be independent of spreading rate above 2 cm/yr. Modified from White et al. (2001) and Dick et al. (2003).

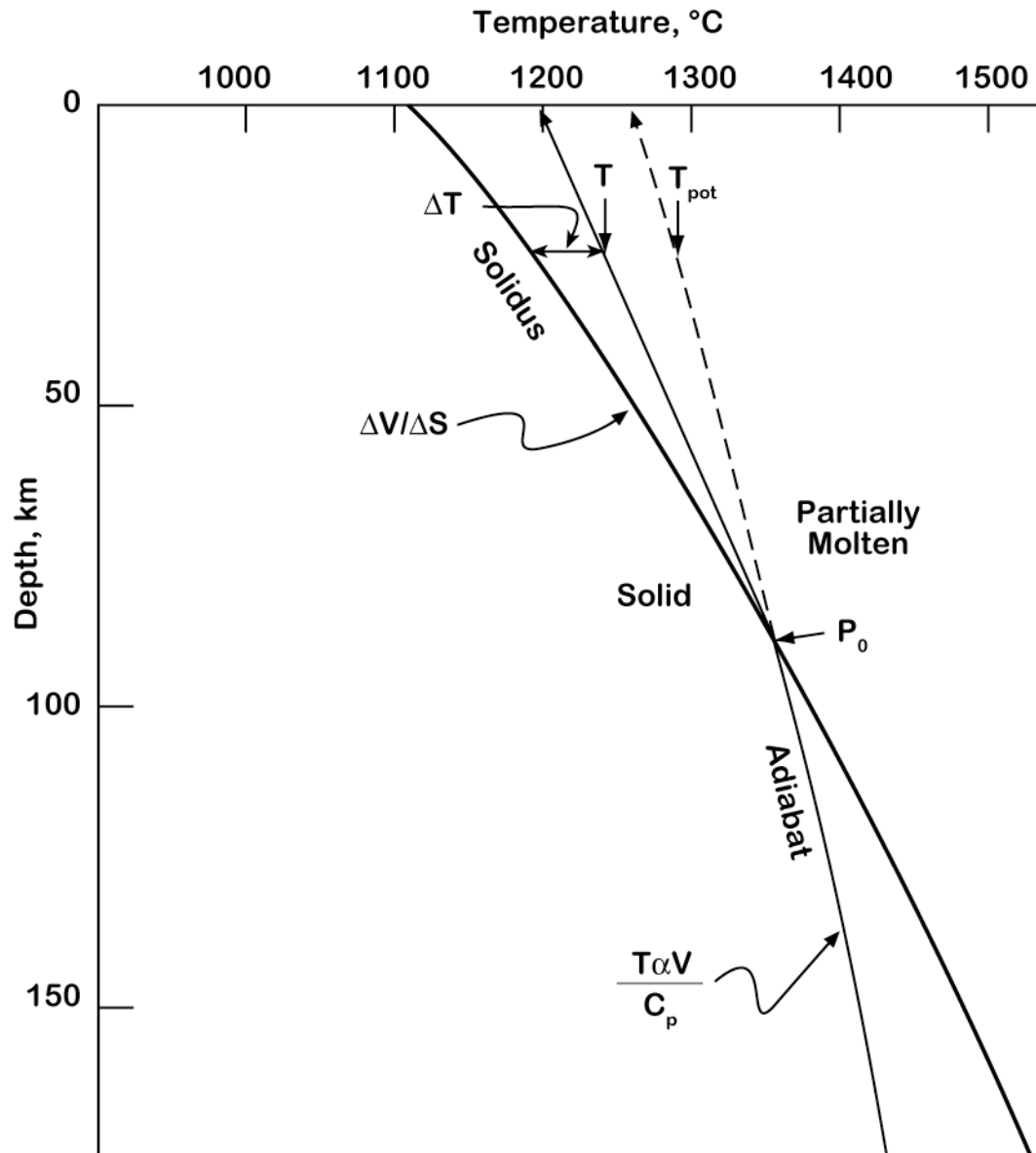


Figure 4. Thermodynamics of mantle upwelling and melting beneath a mid-ocean ridge. P_0 is the pressure at which melting begins, ΔT is the excess temperature of the mantle relative to the solidus. The extent of melting will depend on ΔT . T_{pot} is the mantle potential temperature: the temperature of mantle rock brought to the surface without melting. See text for further explanation.

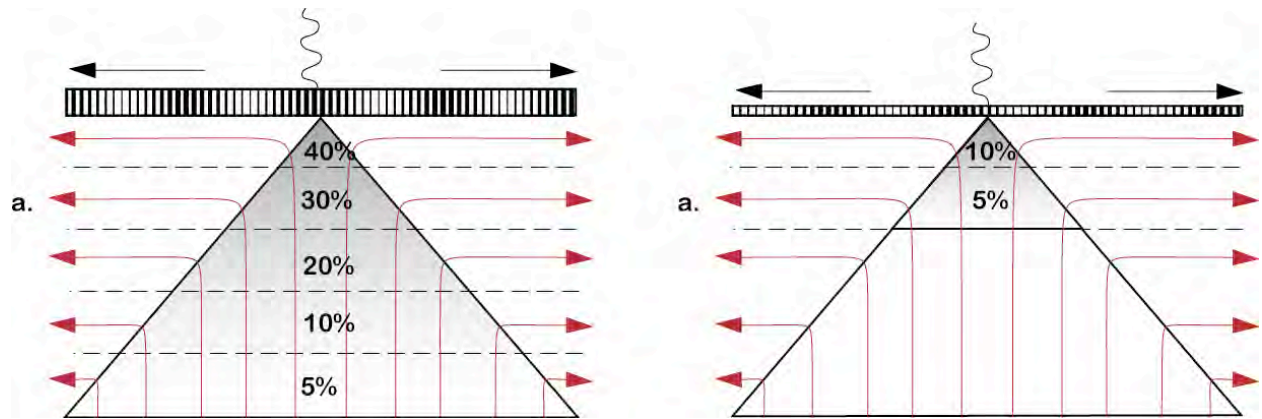


Figure 5. Steady-state passive upwelling and melting regime model beneath mid-ocean ridge. Solid red curves with arrows are mantle flow paths through the melting regime; dashed lines are contours of the extent of melting. The cartoon illustrates melting for two different mantle temperatures. On the left, hotter mantle intersects the solidus deeper (Fig. 4), leading to greater extents of melting; on the right, colder mantle intersects the solidus at shallower depth, leading to less extents of melting and a thinner crust. After Plank and Langmuir (1992).

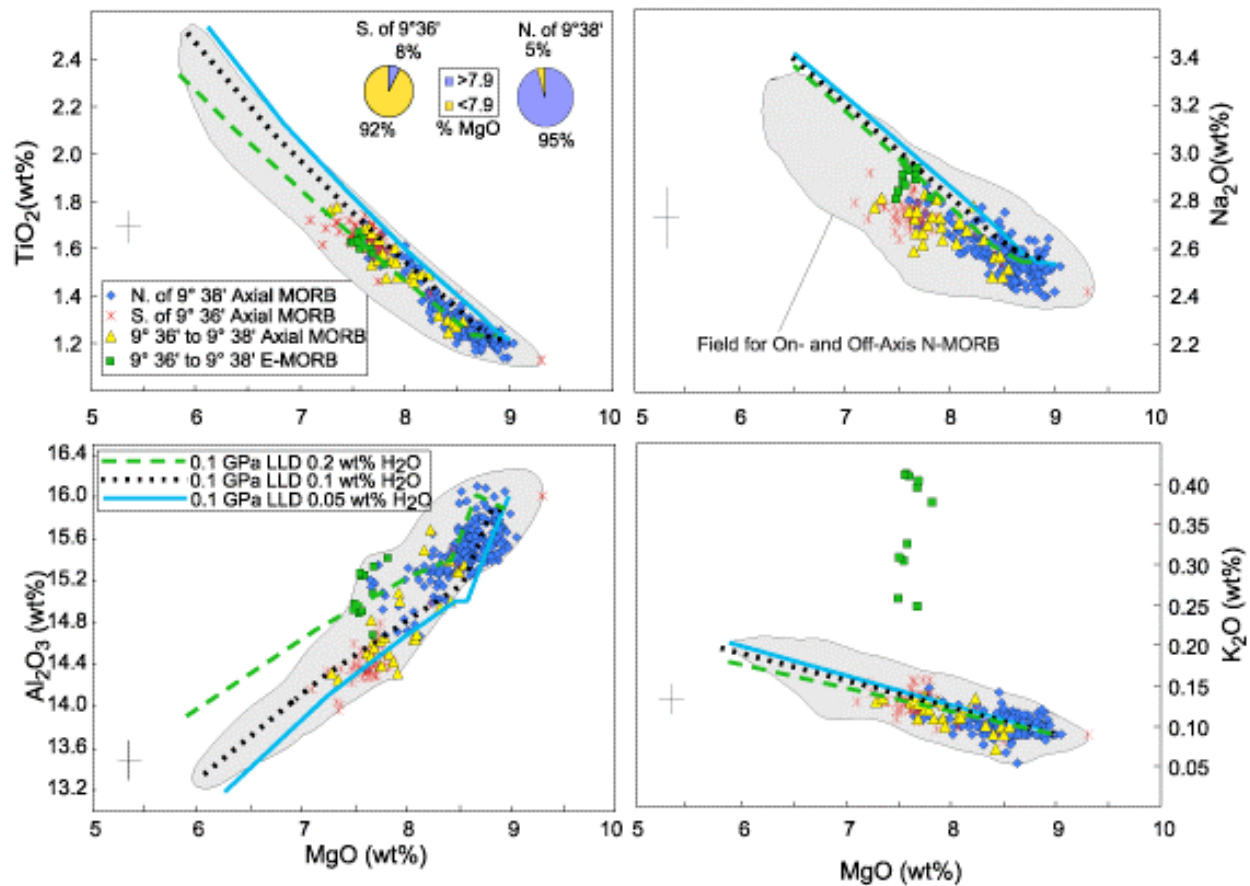


Figure 6. Covariation of TiO₂, Na₂O, Al₂O₃, and K₂O with MgO for MORB recovered by submersible near 9° 27'N on the EPR. Field denotes compositional range for all rock core or submersible samples from the EPR. Crossed lines indicating ± 2 -sigma errors are shown and indicate approximately $\pm 2\%$ of MgO and Al₂O₃, $\pm 4\%$ of TiO₂, $\pm 5\%$ of Na₂O, and $\pm 15\%$ of K₂O. Colored lines represent liquid lines of descent calculated using MELTS for parents with 0.05 (blue solid line), 0.1 (black short dashed line), and 0.2 (green long dashed line) wt.% H₂O (see text for details of models). Pie diagrams in upper right show relative percentages of samples with less than (yellow) and greater than (blue) 7.9 wt.% MgO. From Smith et al. (2001).

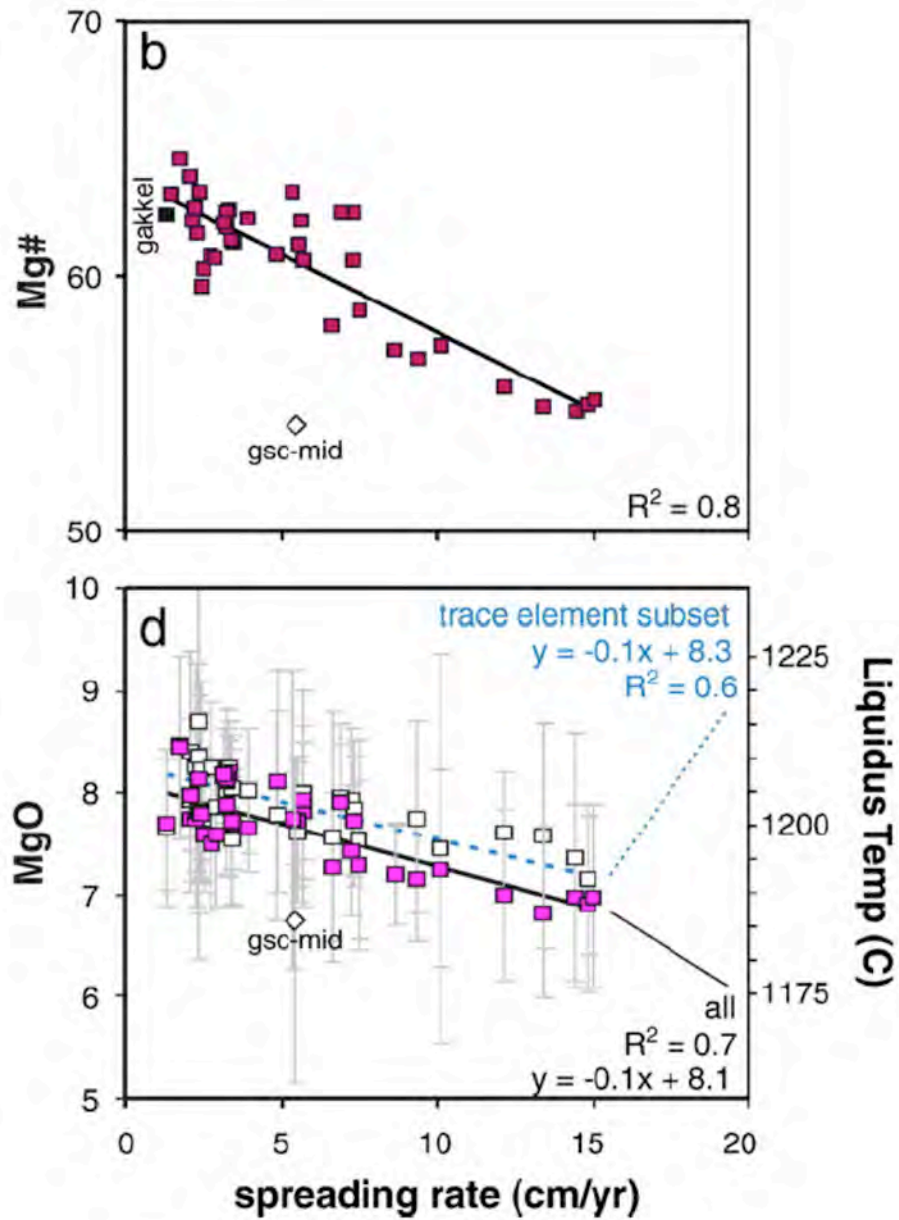


Figure 7. Regional averages of MgO and Mg# from >11,000 MORB samples display strong linear relationships with spreading rate Gakkai datum in panel b estimated from Michael et al., 2003. Panel d also shows mean MgO for both the entire >11,000 sample suite (solid symbols) and the 2100 sample glass/whole rock subset for which trace element and isotopic data also exist (open symbols). The same inverse correlation is observed in both. From Rubin and Sinton (2007).

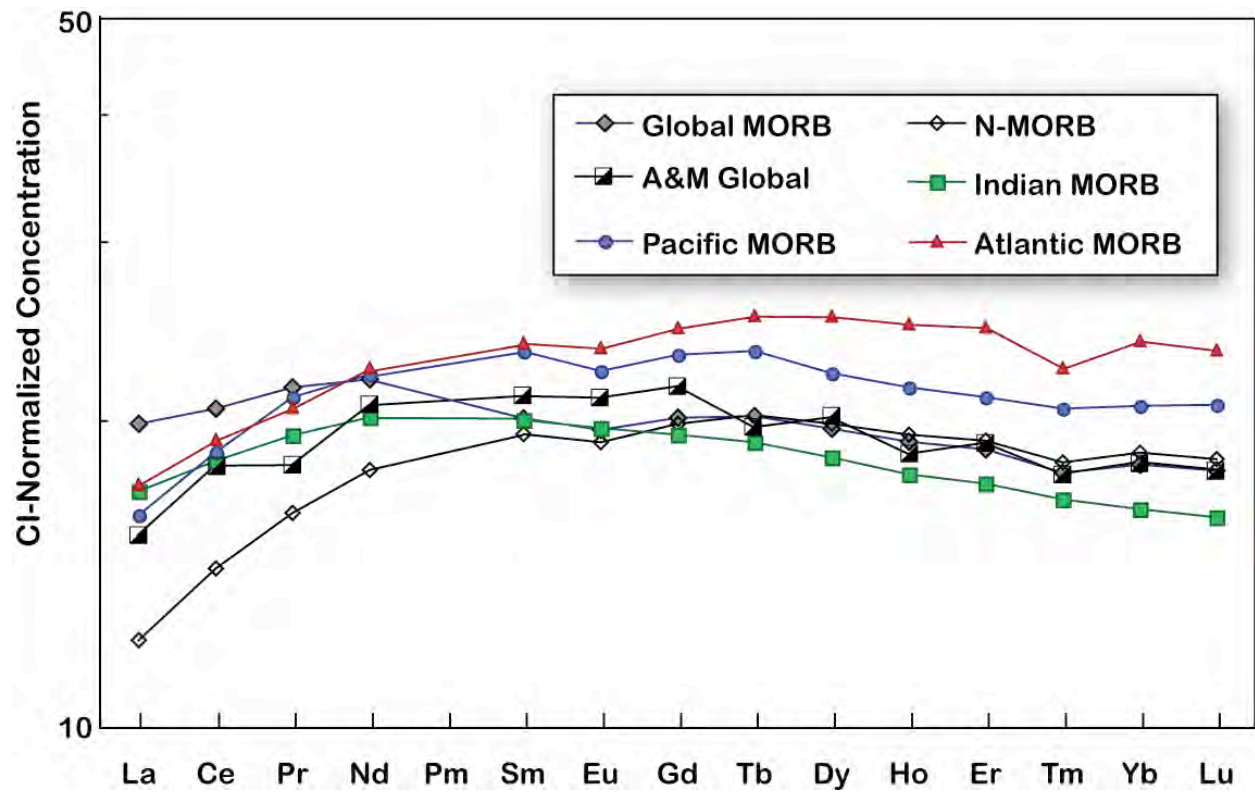


Figure 8. CI-normalized rare earth patterns of the global and regional MORB average listed in Table 2. A&M is the log-normal average MORB of Arevalo and McDonough (2010).

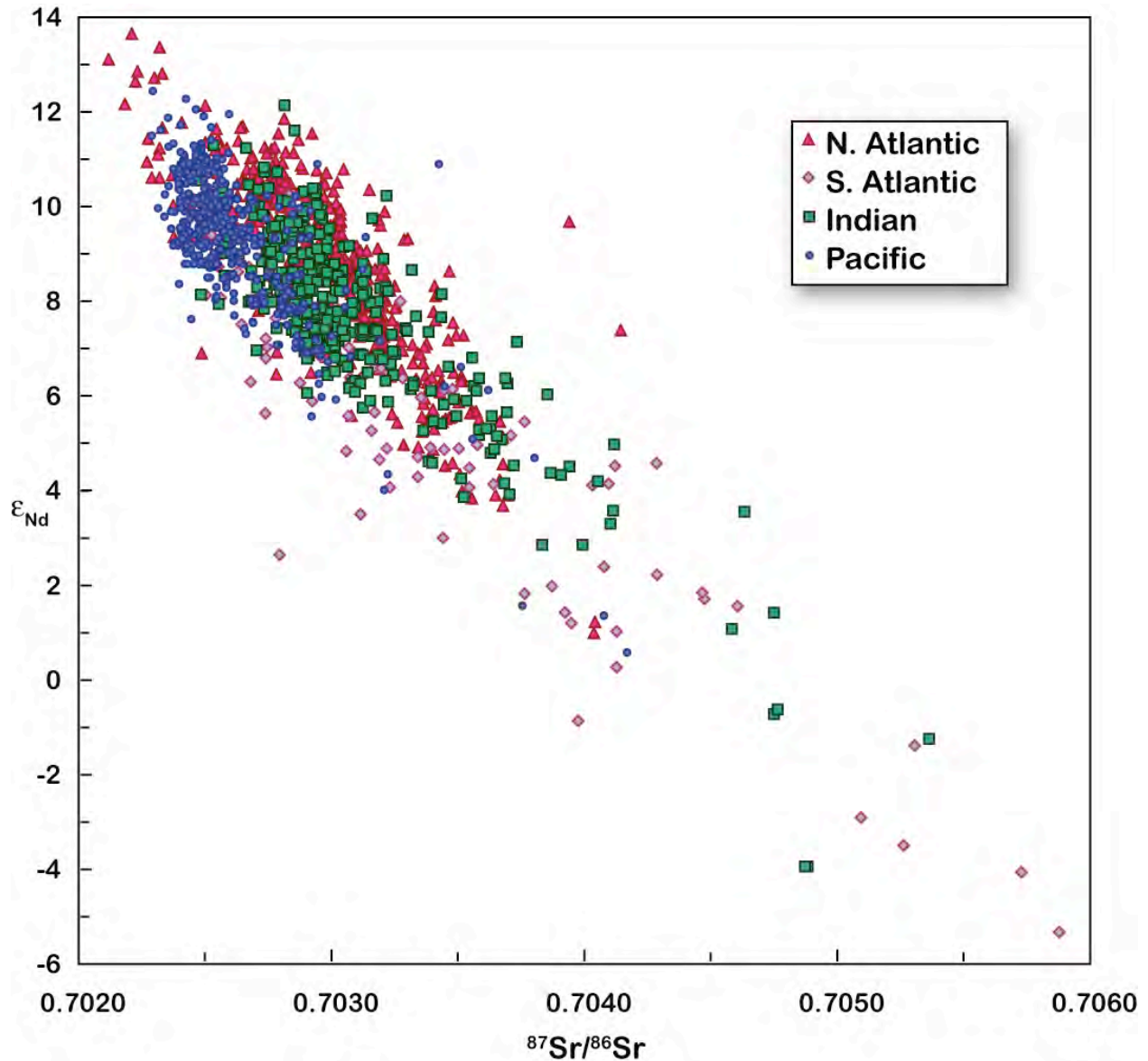


Figure 9. Sr and Nd isotope ratios in mid-ocean ridge basalts. Plotting symbols are assigned such that samples north of 23°S in the Atlantic are “N. Atlantic” and the Bouvet triple junction and the Australian Antarctic Discordance at 127°E are taken as the west and east, respectively, boundaries of the Indian Ocean. The actual boundary between the “S. Atlantic mantle domain” and “Indian mantle domain” may be the Andrew Bain Fracture Zone at 30°E (Meyzen et al., 2007). Data from the PetDB database.

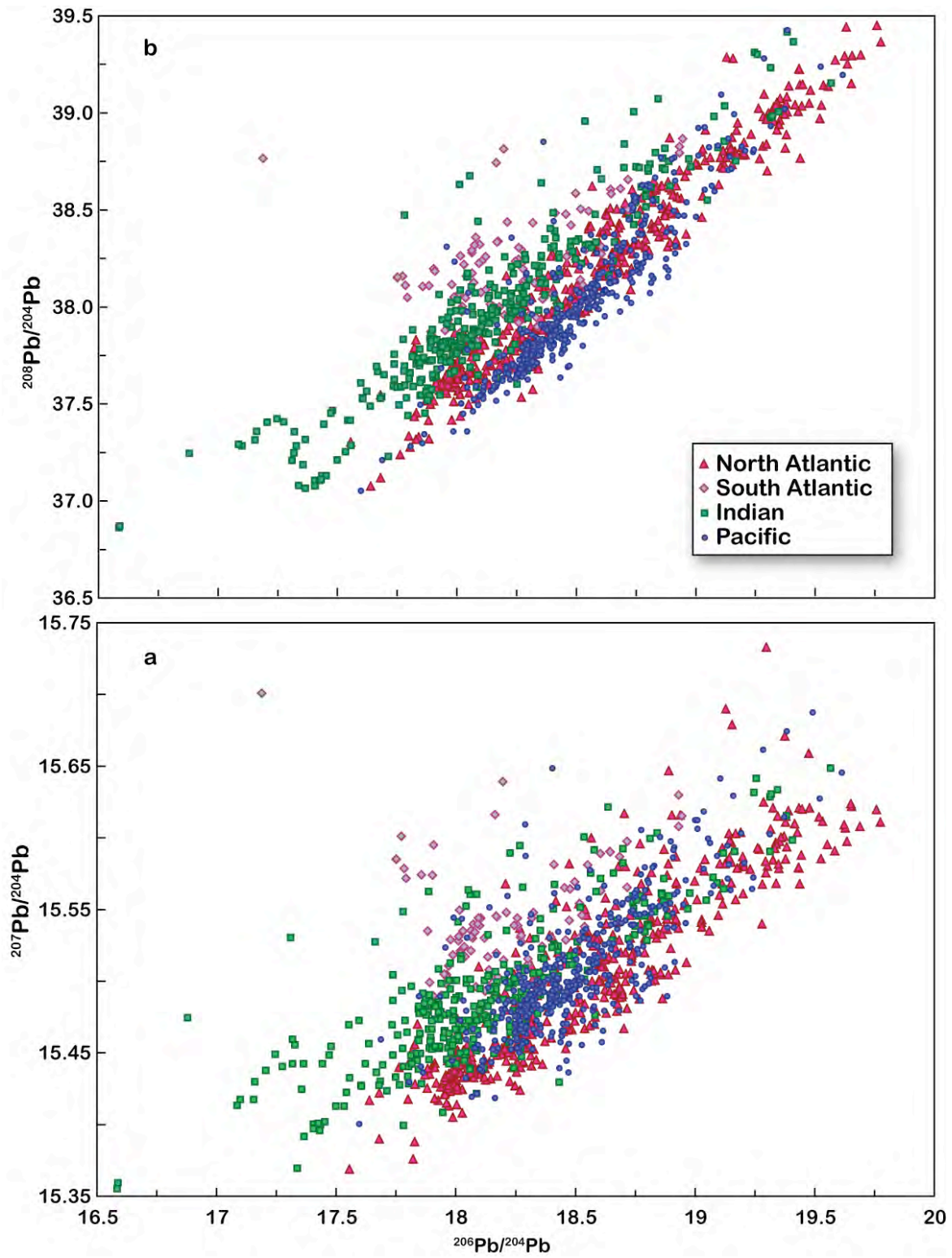


Figure 10. Pb isotope ratios in mid-ocean ridge basalts. Data from the PetDB database.

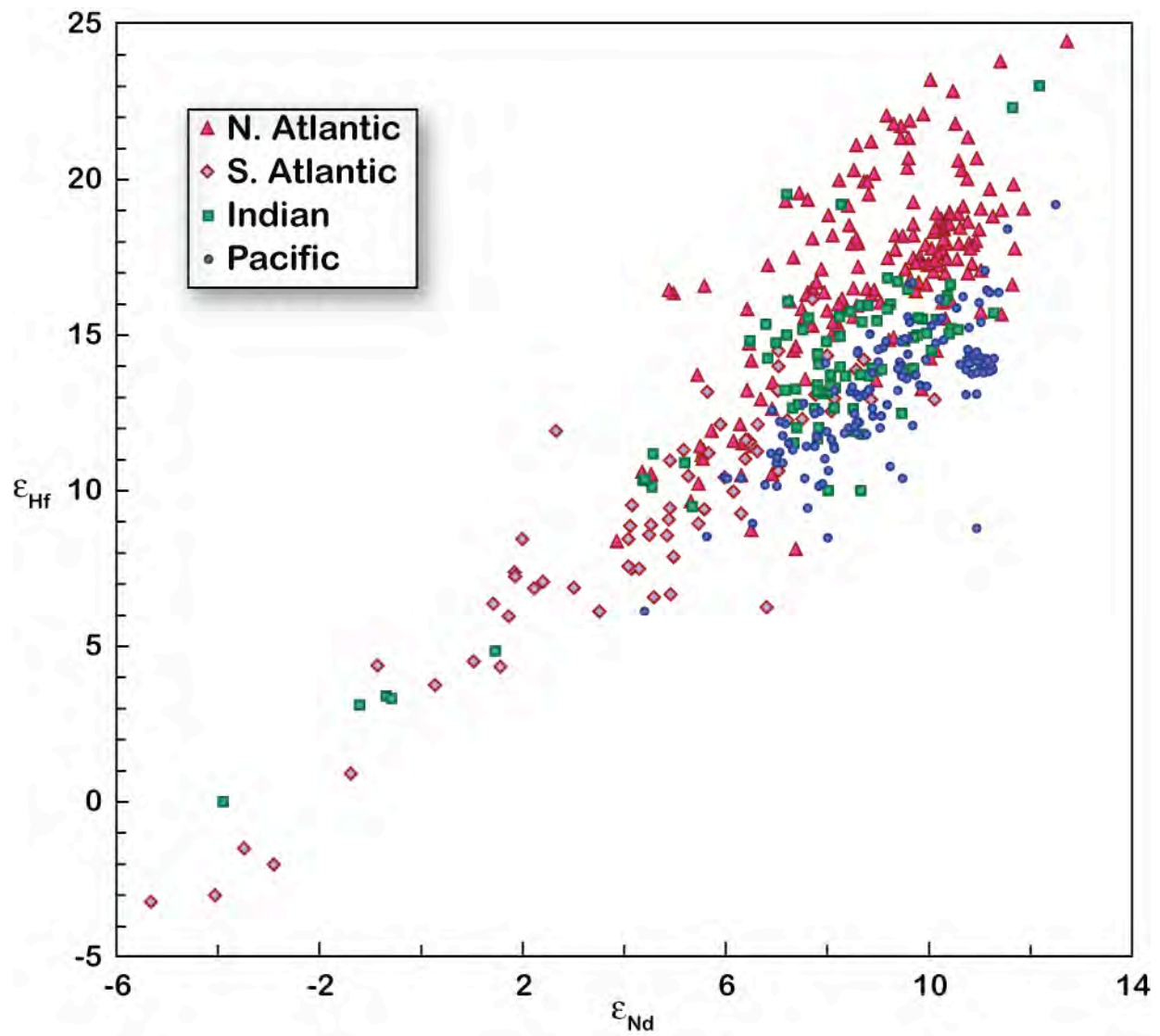


Figure 11. Hf and Nd isotope ratios in mid-ocean ridge basalts. Data from the PetDB database.

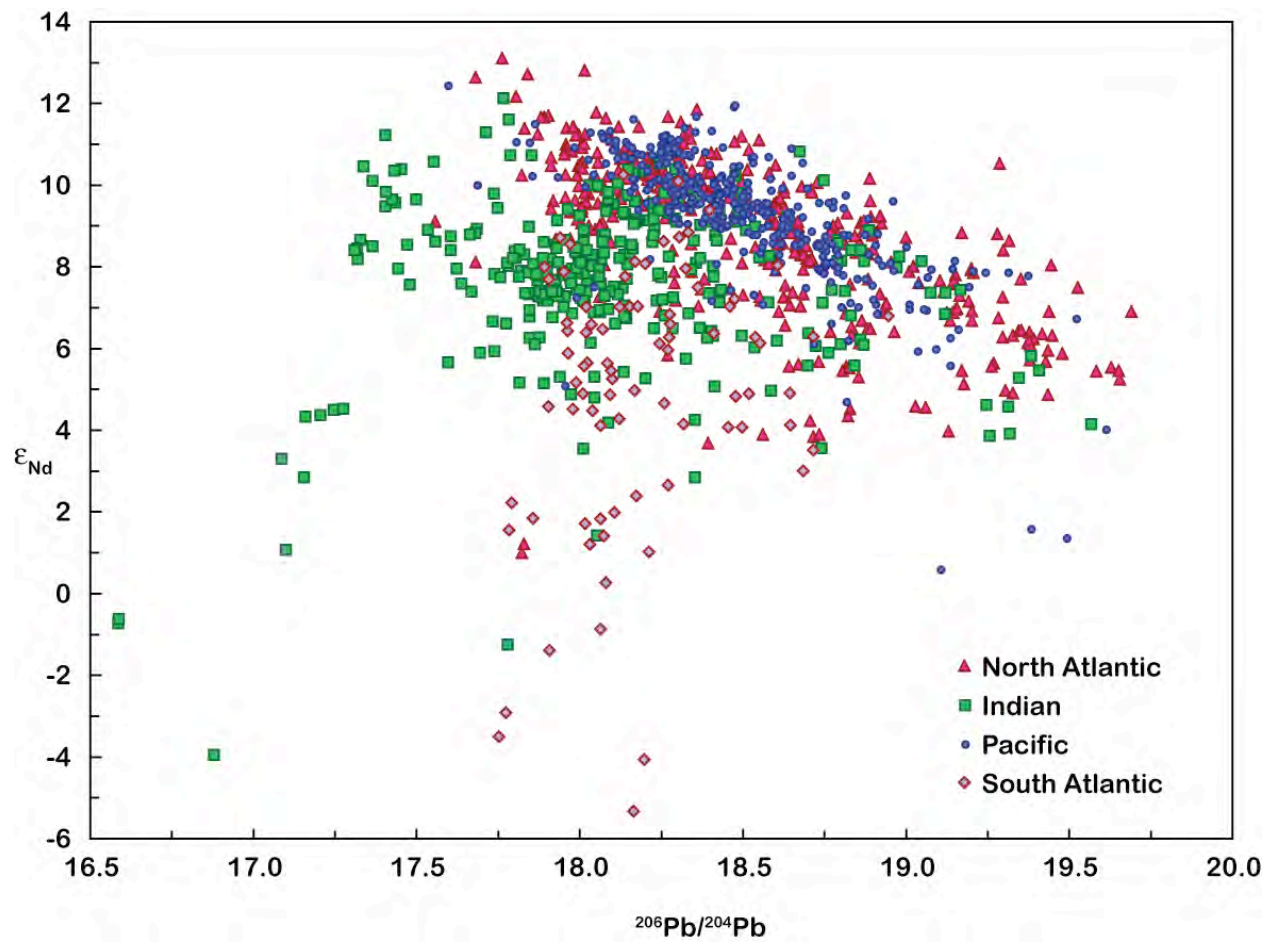


Figure 12. Nd and Pb isotope ratios in mid-ocean ridge basalts. Data from the PetDB database.

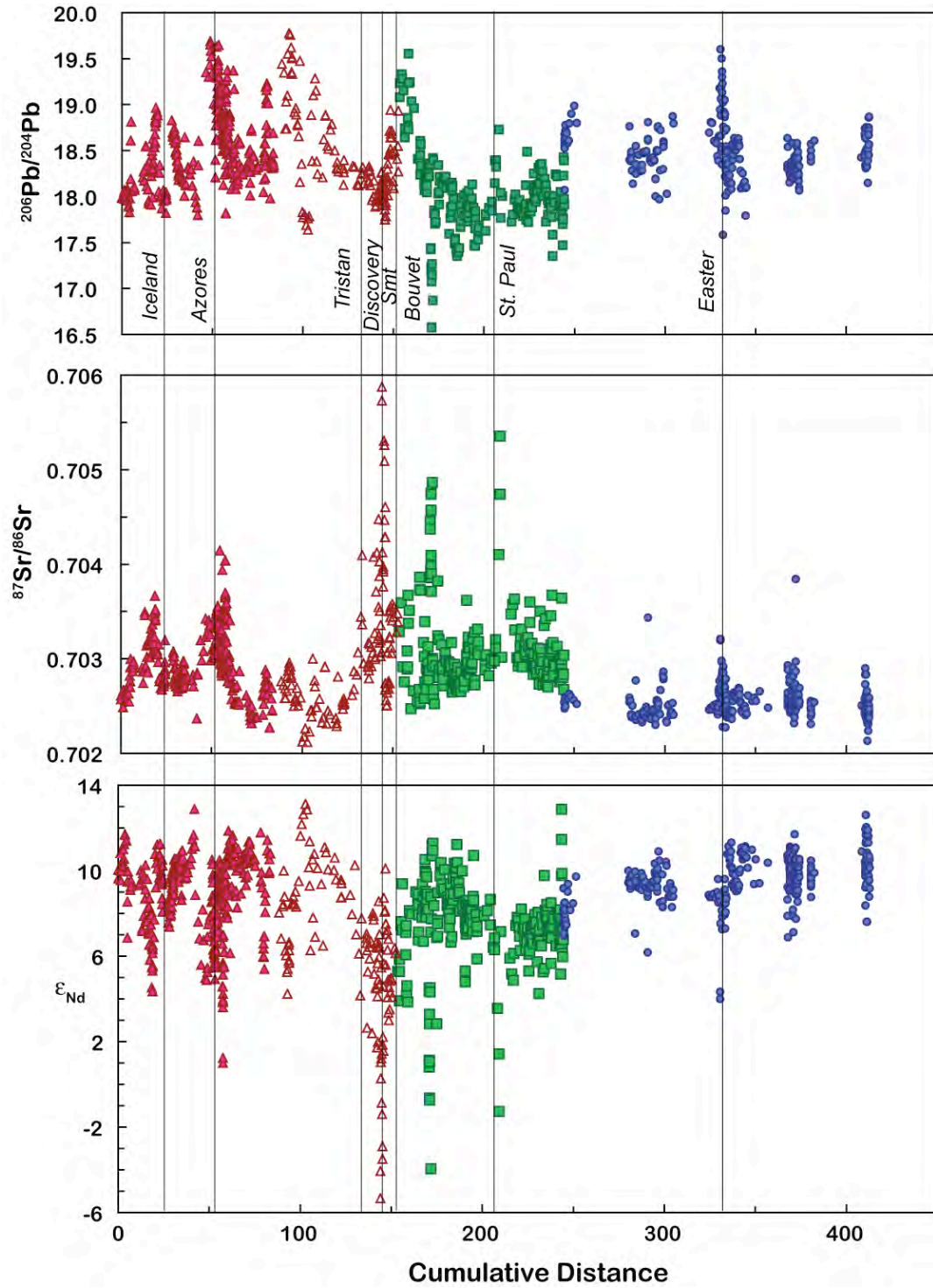


Figure 13. ϵ_{Nd} , $^{87}\text{Sr}/^{86}\text{Sr}$, and $^{206}\text{Pb}/^{204}\text{Pb}$ from the “continuous” part of the mid-ocean ridge system as a function of angular distance from the northernmost sample as calculated by Meyzen et al. (2007). The “0” point is the location of the northernmost sample site of the Gakkel Ridge at 85.64°N, 85.05 E.

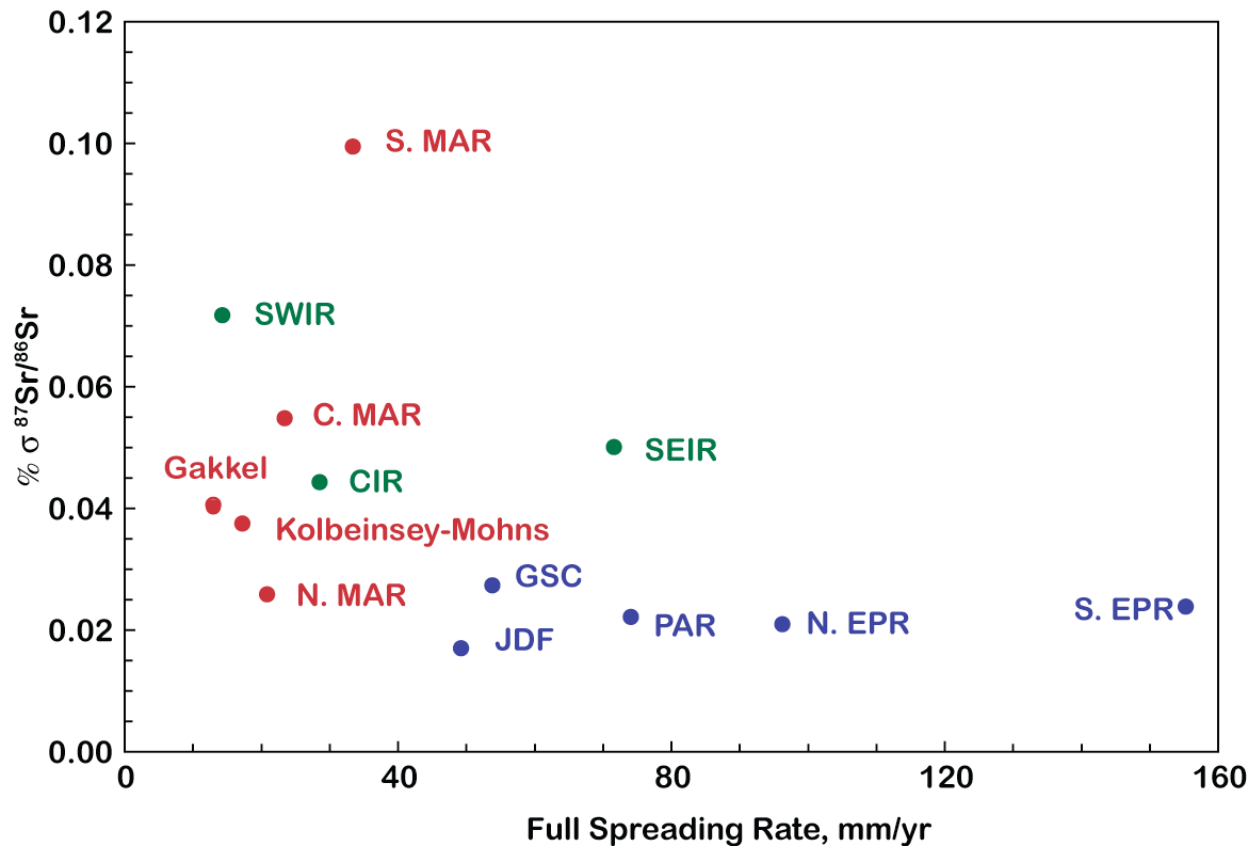


Figure 14. Standard deviation of $^{87}\text{Sr}/^{86}\text{Sr}$ for samples from various mid-ocean ridges as a function of spreading rate. MAR: Mid-Atlantic Ridge, SWIR: Southwest Indian Ridge, CIR: Central Indian Ridge, SEIR: Southeast Indian Ridge, JDF: Juan de Fuca Ridge, GSC: Galapagos Spreading Center, PAR: Pacific-Antarctic Ridge, EPR: East Pacific Rise.

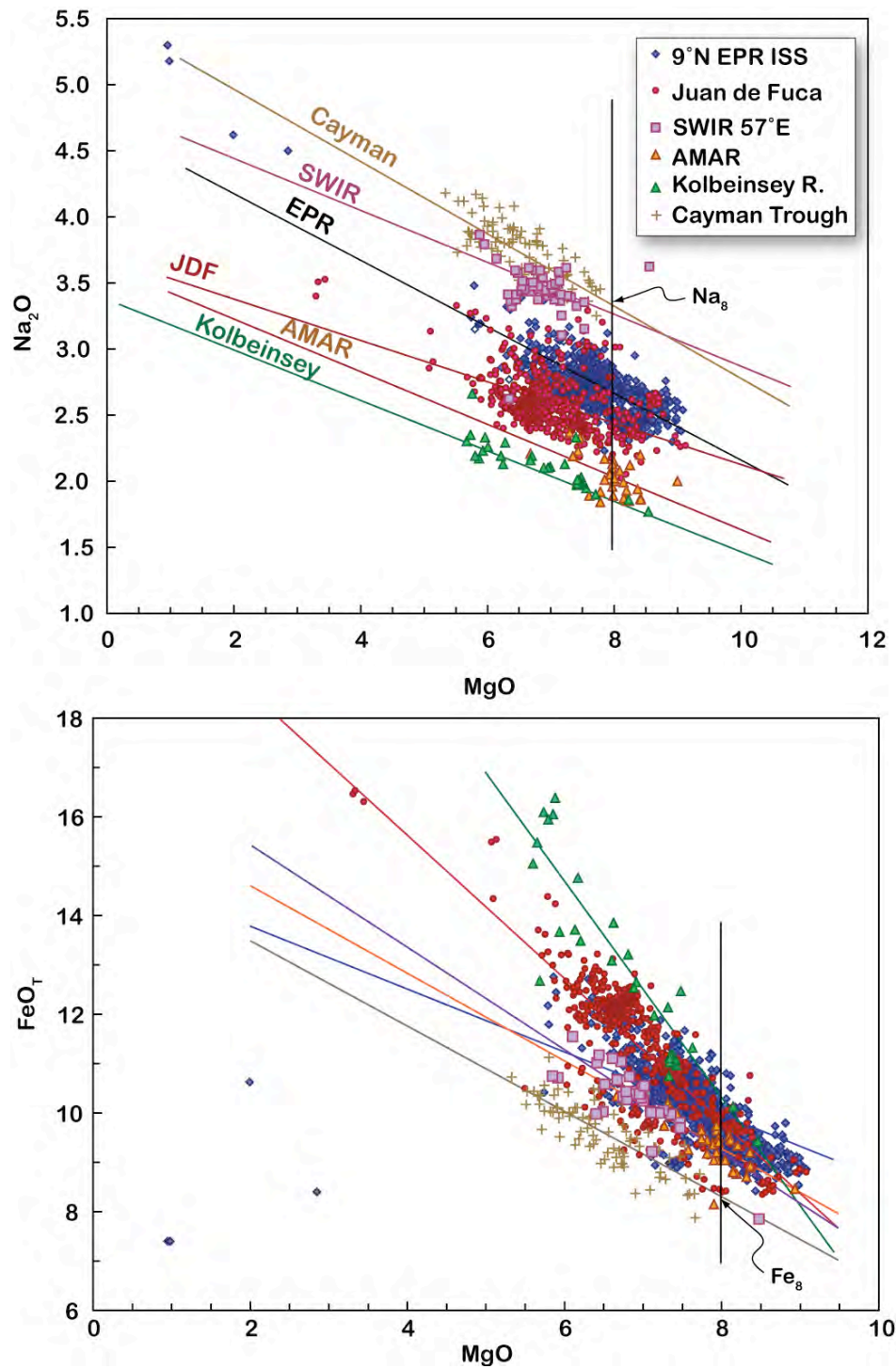


Figure 15. Na_2O and FeO vs. MgO in MORB from various regions of the mid-ocean ridge system plot along liquid lines of descent of varying slopes. $\text{Fe}_{8.0}$ and $\text{Na}_{8.0}$ are the value of Na_2O and FeO , respectively, of the lines at 8.0% MgO . The AMAR region is located at 37-38° N on the Mid-Atlantic Ridge.

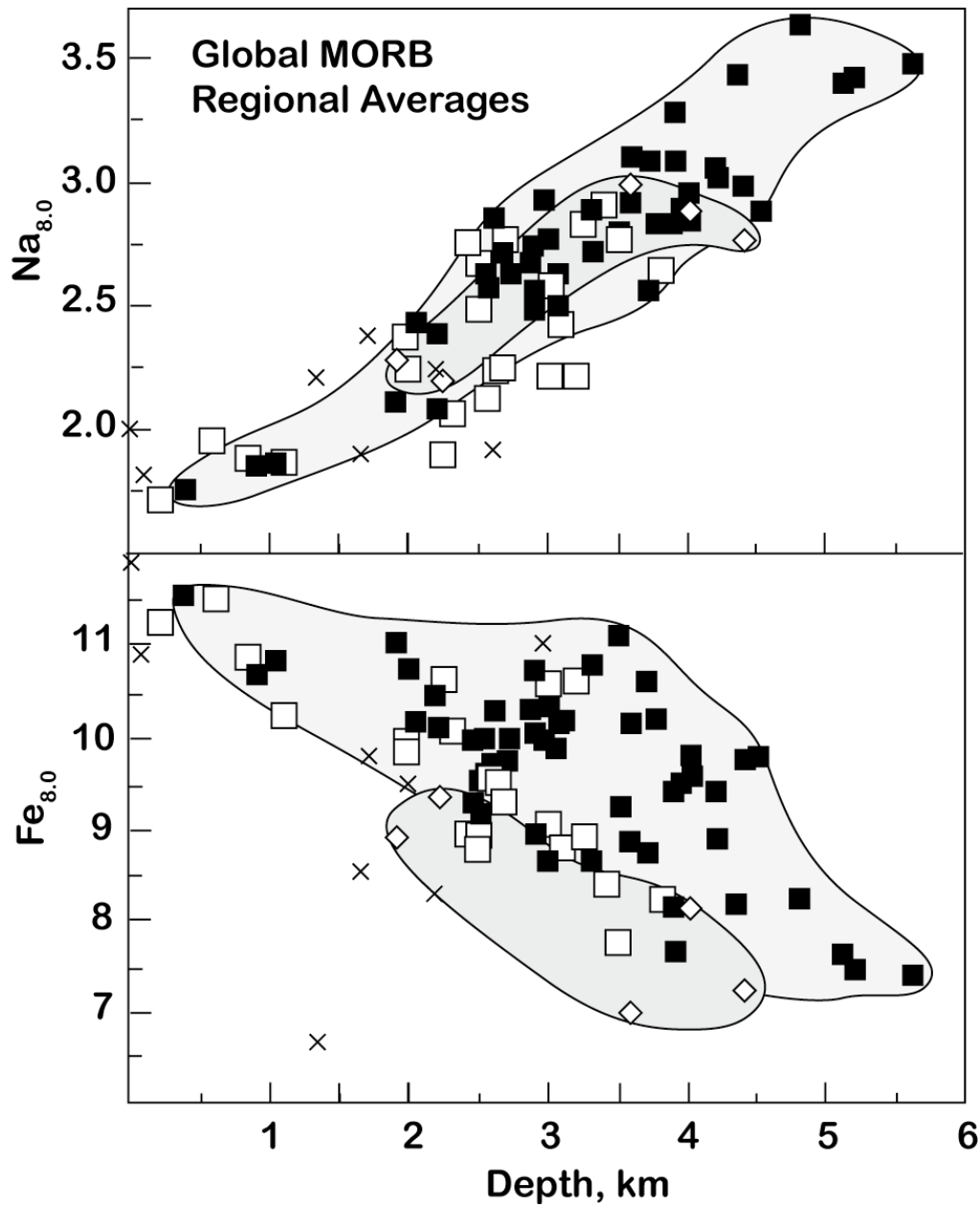


Figure 16. Regional average $\text{Fe}_{8.0}$ and $\text{Na}_{8.0}$ as a function of regional average axial depth in the mid-ocean ridge system. This figure is the same as figure 2 in Klein and Langmuir (1987), except all analyses have been recalculated to sum to 100% (all iron as FeO) and have been corrected for interlaboratory differences. solid boxes are MORB from “normal” ridge segments; diamonds are from back-arc basins; open squares are from ridges influenced by the Galapagos, Azores, Jan Mayen, Tristan, Iceland, and Bouvet hotspots; Xs are from ridge segments immediately adjacent to these hotspots. Darker grey field encompasses back-arc basin basalts; light grey field encompasses normal ridge basalts.

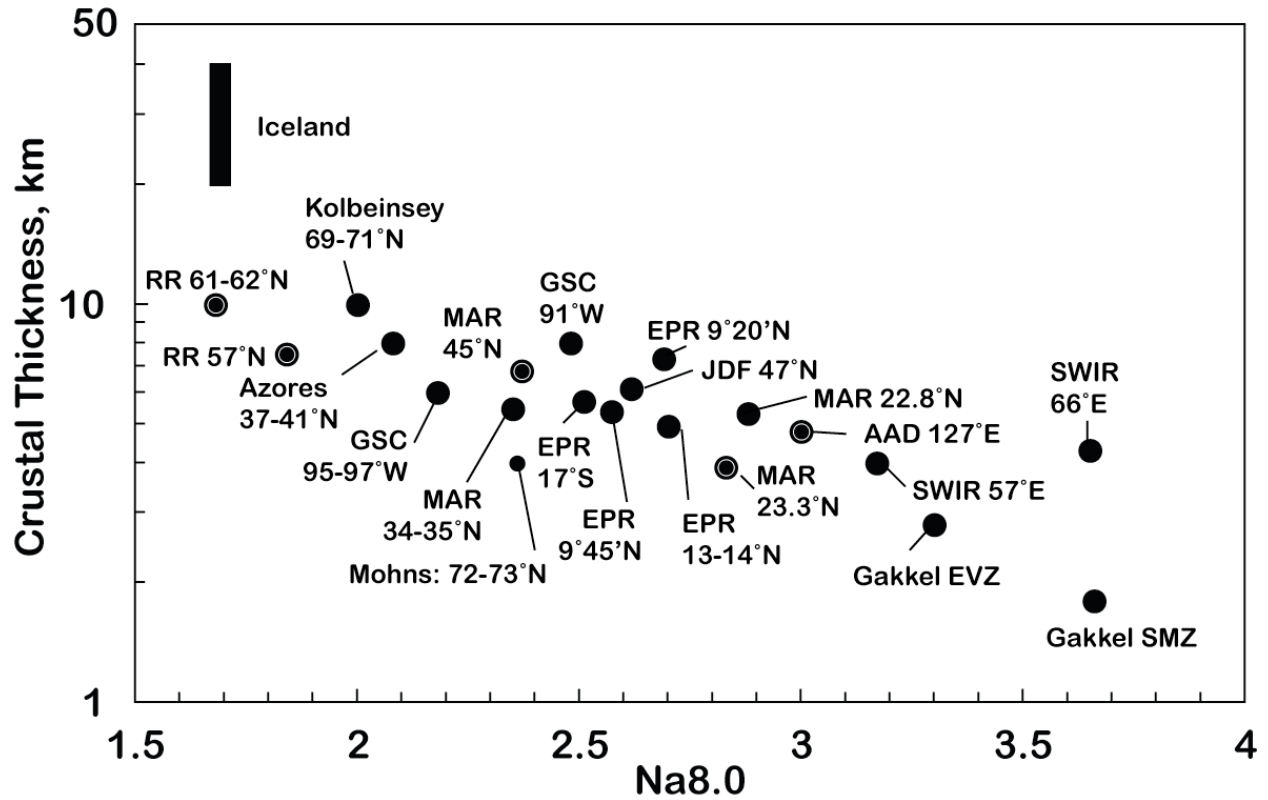


Figure 17. Regional averages of seismically determined crustal thickness versus Na8.0 (the Na_2O content of basalts normalized to 8 wt.% MgO; Klein and Langmuir, 1987). Sources for seismic determinations of crustal thickness are from Klein and Langmuir (1987), augmented and/or superceded by the following: Smallwood and White (1998); Navin et al. (1998); Darbyshire et al. (2000); Detrick et al. (2002); Muller et al. (1999); Hooft et al. (2000); Fowler and Keen (1979); Canales et al. (1998); McClain and Lewis (1982); Kodaira et al. (1997); Klingelhöfer et al. (2000); Jokat et al. (2003); Michael et al. (2003); Holmes (2008).

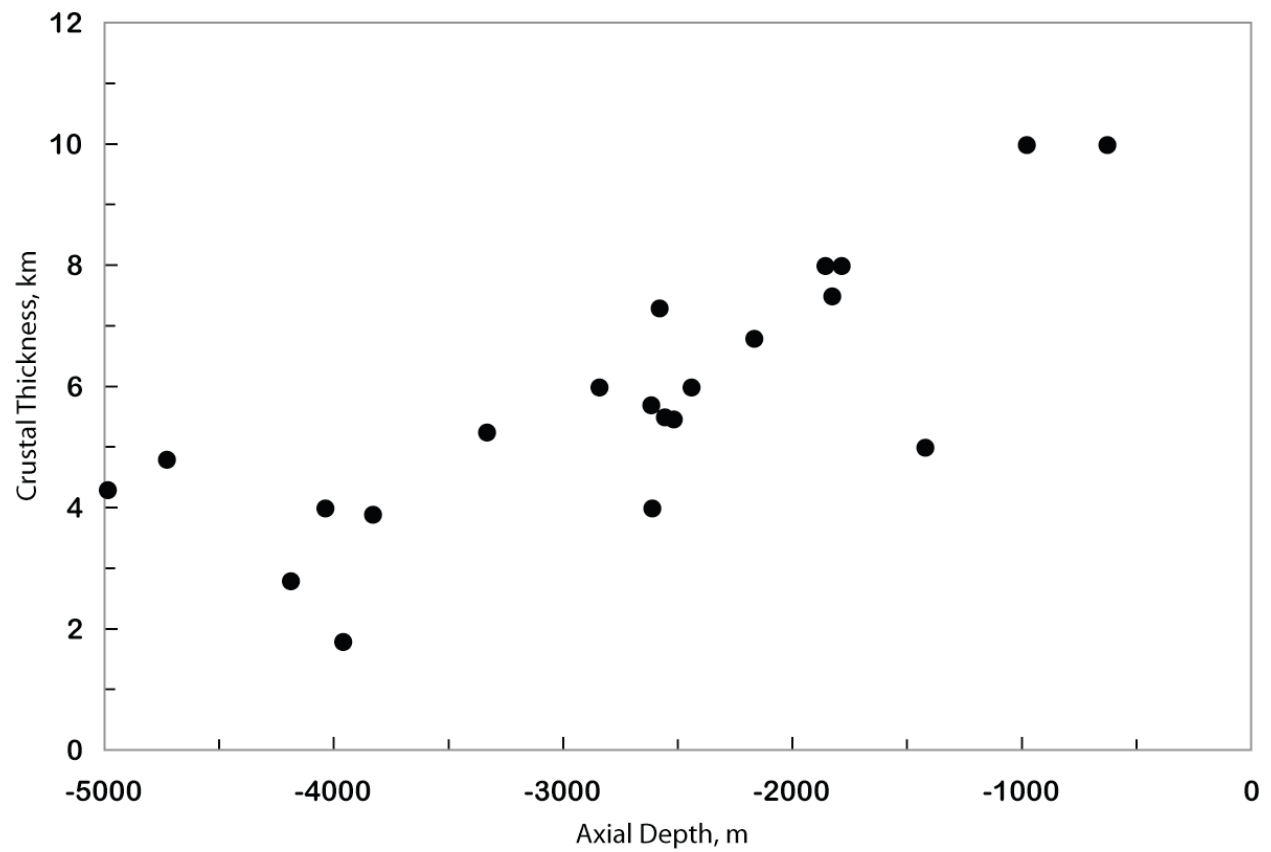


Figure 18. Relationship between axial depth and seismically determined crustal thickness along mid-ocean ridges. The thickest crust, and by implication the greatest extents of melting, occur at the shallowest axial depths. Crustal thickness data sources are the same as in Figure 17.

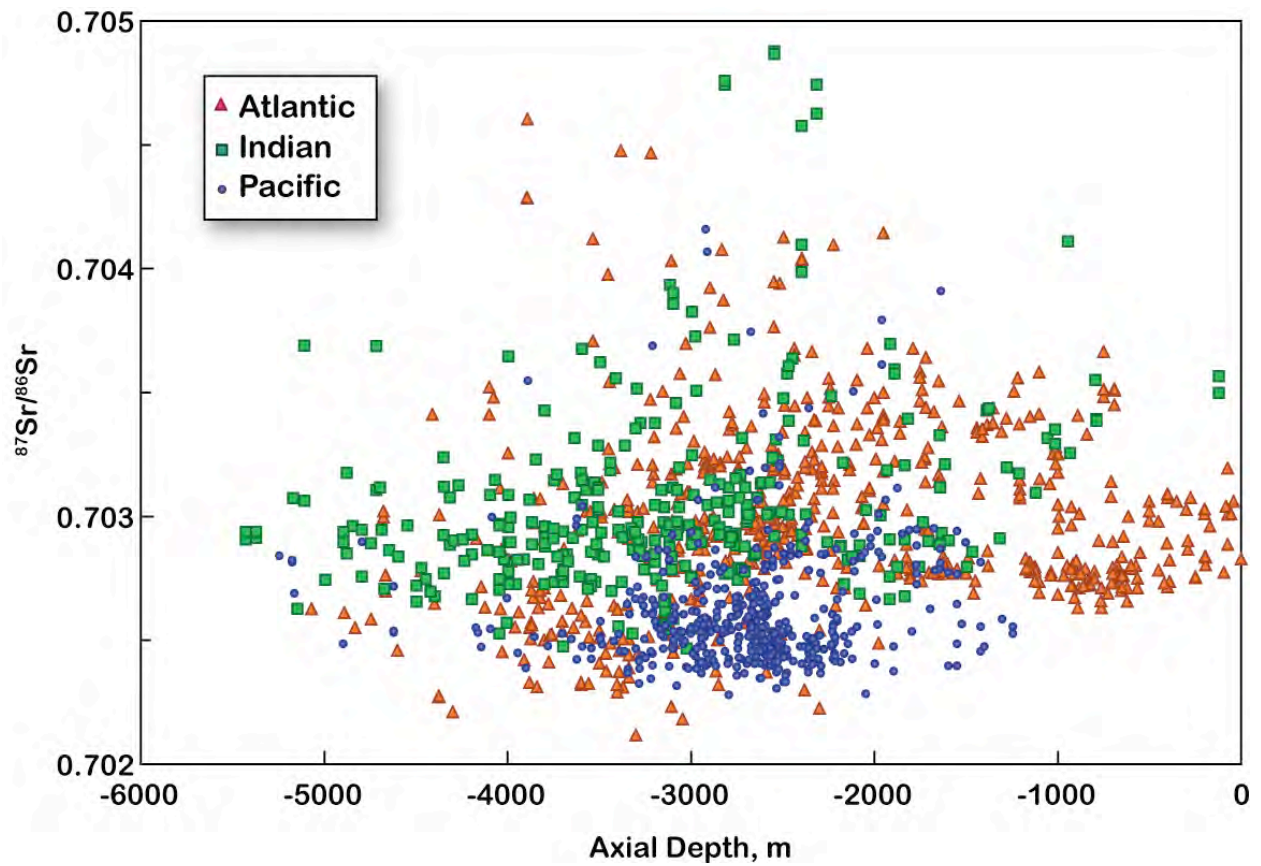


Figure 19. $^{87}\text{Sr}/^{86}\text{Sr}$ shows no correlation with axial depth; instead maximum values tend to occur at intermediate axial depth. This suggests that mantle composition is not related to axial depth.

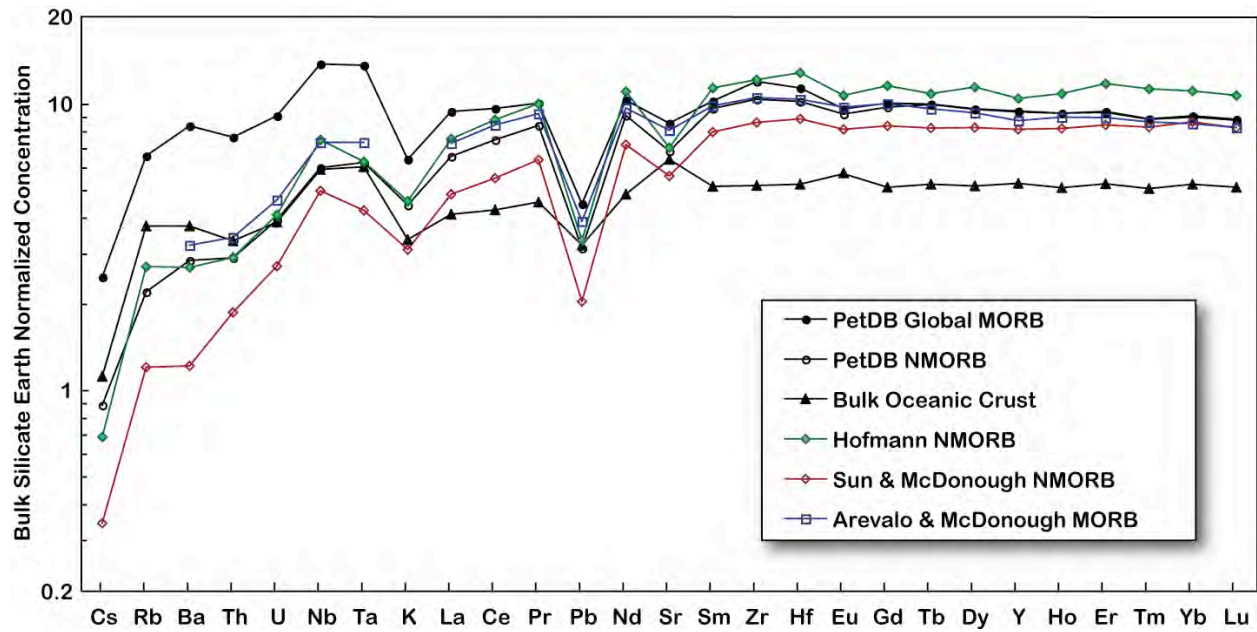


Figure 20. Comparison of the estimated bulk ocean crust composition with various average MORB compositions from Table 2 on “Spider” or “extended rare Earth” diagram in which the elements are arranged in order of increasing compatibility. Element concentrations are normalized to the bulk silicate Earth composition estimate of Lyubetskaya and Korenaga (2007). Bulk oceanic crust has a much smaller negative Pb anomaly than average MORB and positive Sr and Eu anomalies in place of the negative ones seen in average MORB. Thus the negative Pb, Eu, and Sr anomalies are due partly (Pb) or wholly (Sr, Eu) to plagioclase fractionation. Bulk oceanic crust also has a positive Ta, Nb anomaly.

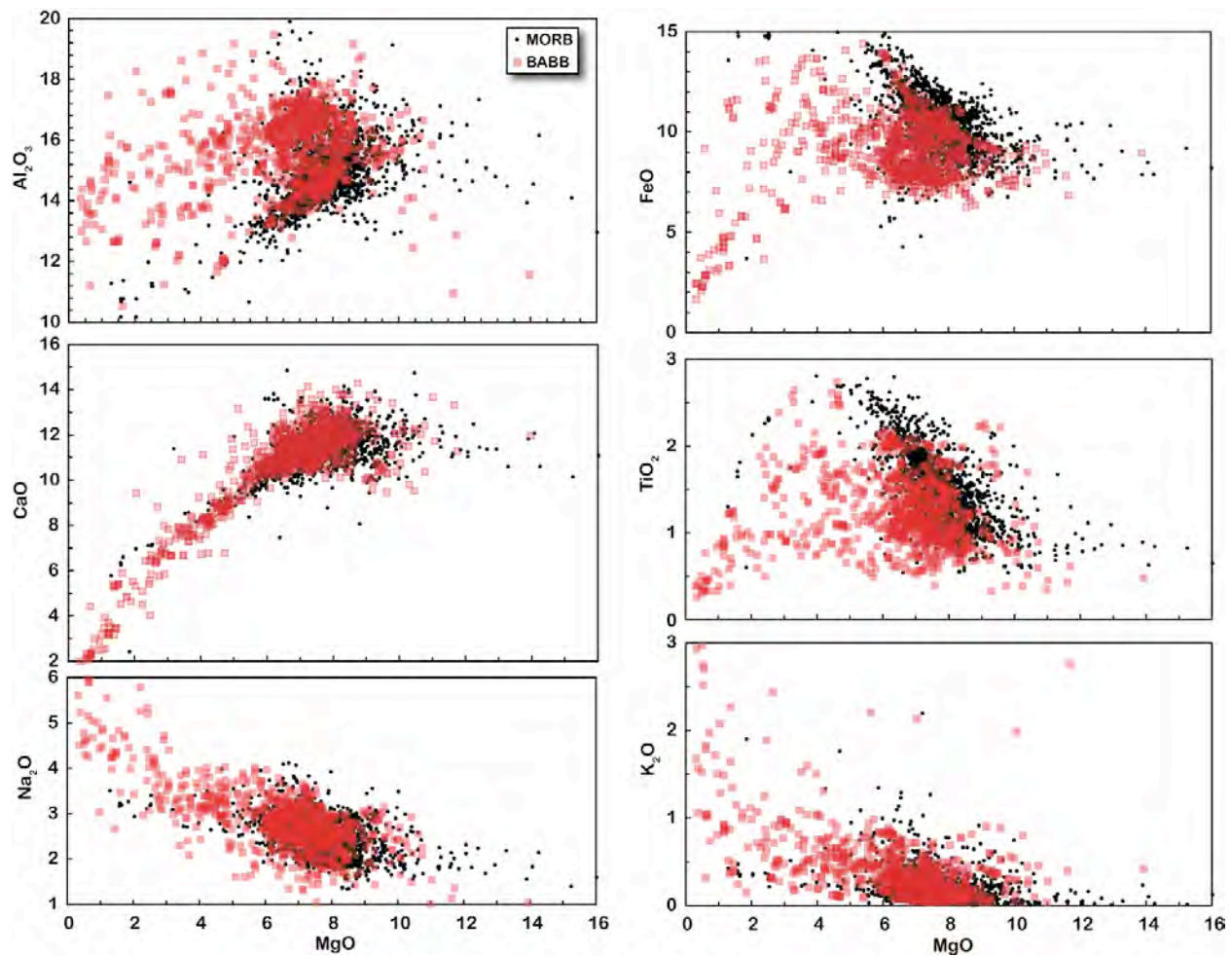


Figure 21. Comparison of major element variations in MORB and BABB. BABB generally having lower FeO and TiO_2 than MORB at a given MgO value. There is also some tendency for greater Al_2O_3 enrichment among differentiated BABB, but compositions are otherwise similar to MORB. Data from the PetDB database.

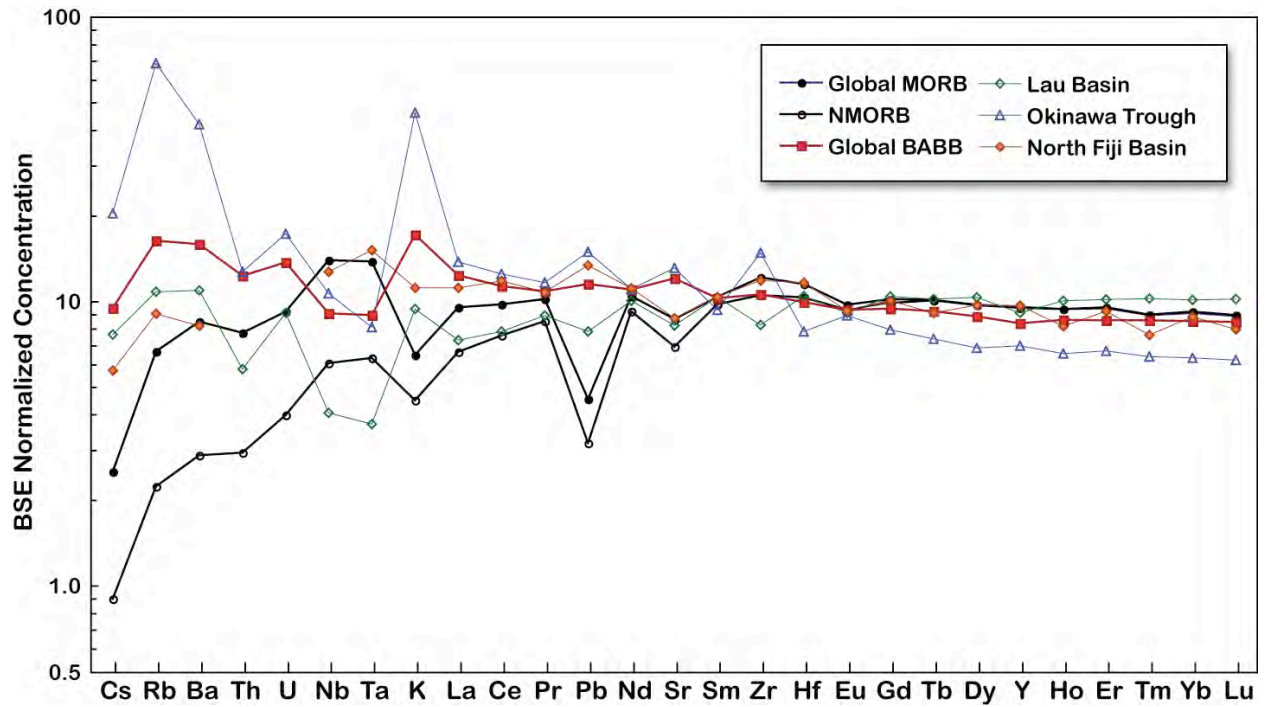


Figure 22. Comparison of incompatible element concentrations in BABB and MORB, normalized to the bulk silicate Earth composition of Lyubetskaya and Korenaga (2007). In contrast to MORB, BABB generally show relative depletions in Ta and Nb, slight enrichments in Pb and Sr, and more pronounced enrichments in K, Rb, Cs, and Ba. Comparison of average compositions from the Lau Basin, Okinawa Trough and North Fiji Basin show, however, that these effects can vary considerably in BABB.

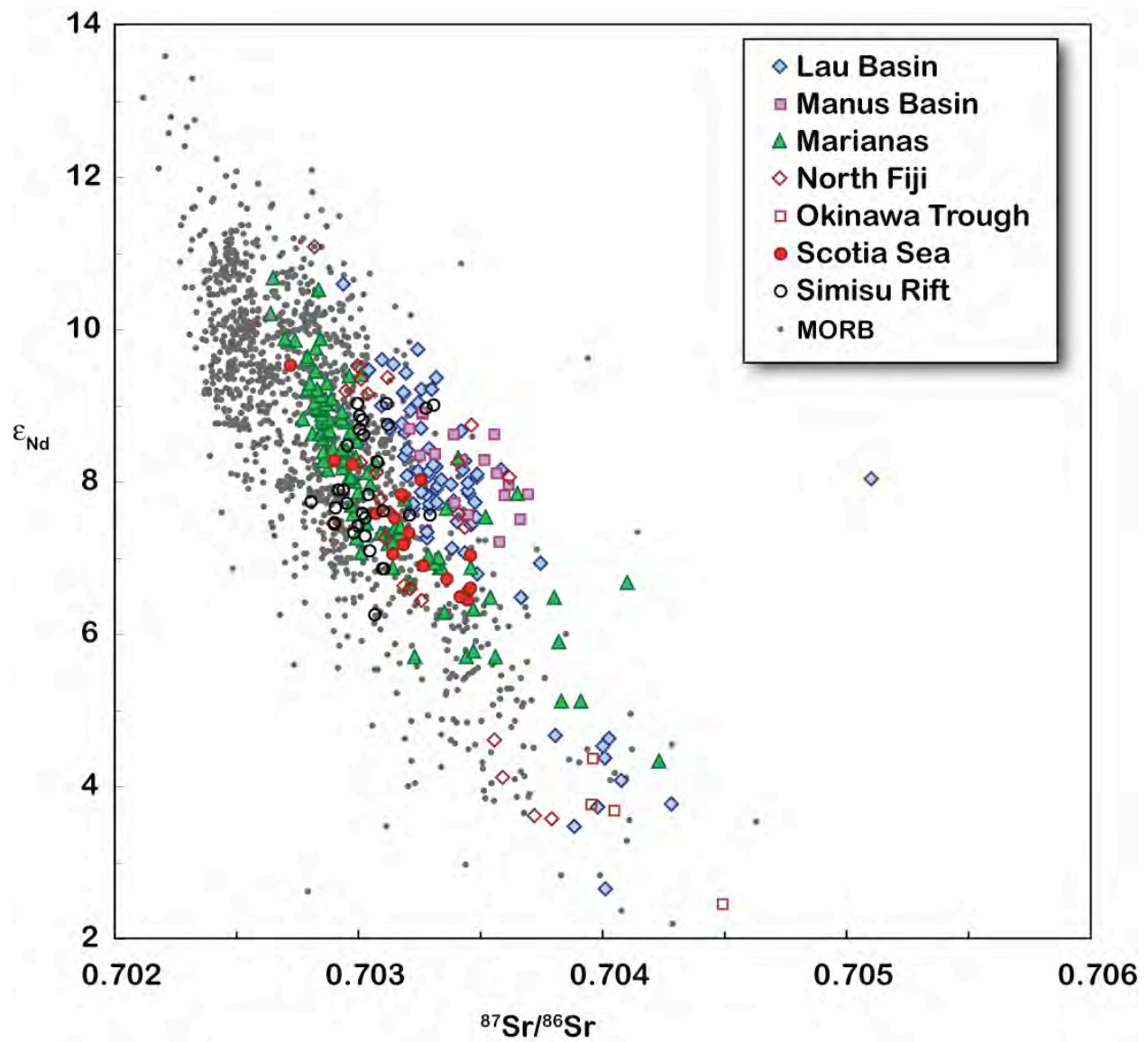


Figure 23. Sr and Nd isotope ratios in BABB. BABB largely overlap the MORB field, but tend to have higher $^{87}Sr/^{86}Sr$ for a given ϵ_{Nd} . Data from the PetDB database.

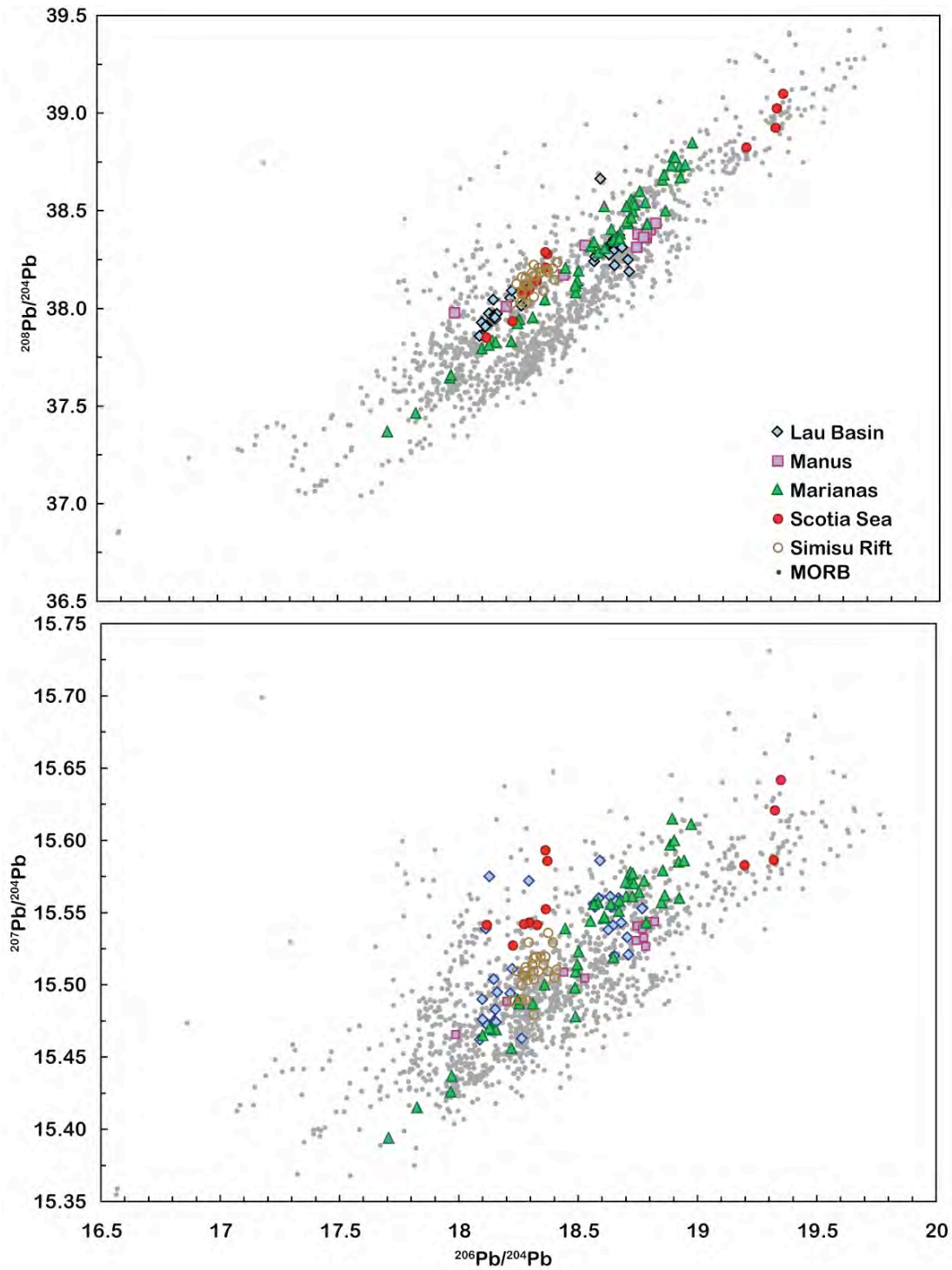


Figure 24. Pb isotope ratios in BABB. BABB have Pb isotope ratios that are similar to MORB, although there is a tendency for BABB to have higher $^{208}\text{Pb}/^{204}\text{Pb}$ for a given $^{206}\text{Pb}/^{204}\text{Pb}$ and some tendency for BABB to scatter to higher $^{207}\text{Pb}/^{204}\text{Pb}$. Data from the PetDB database.

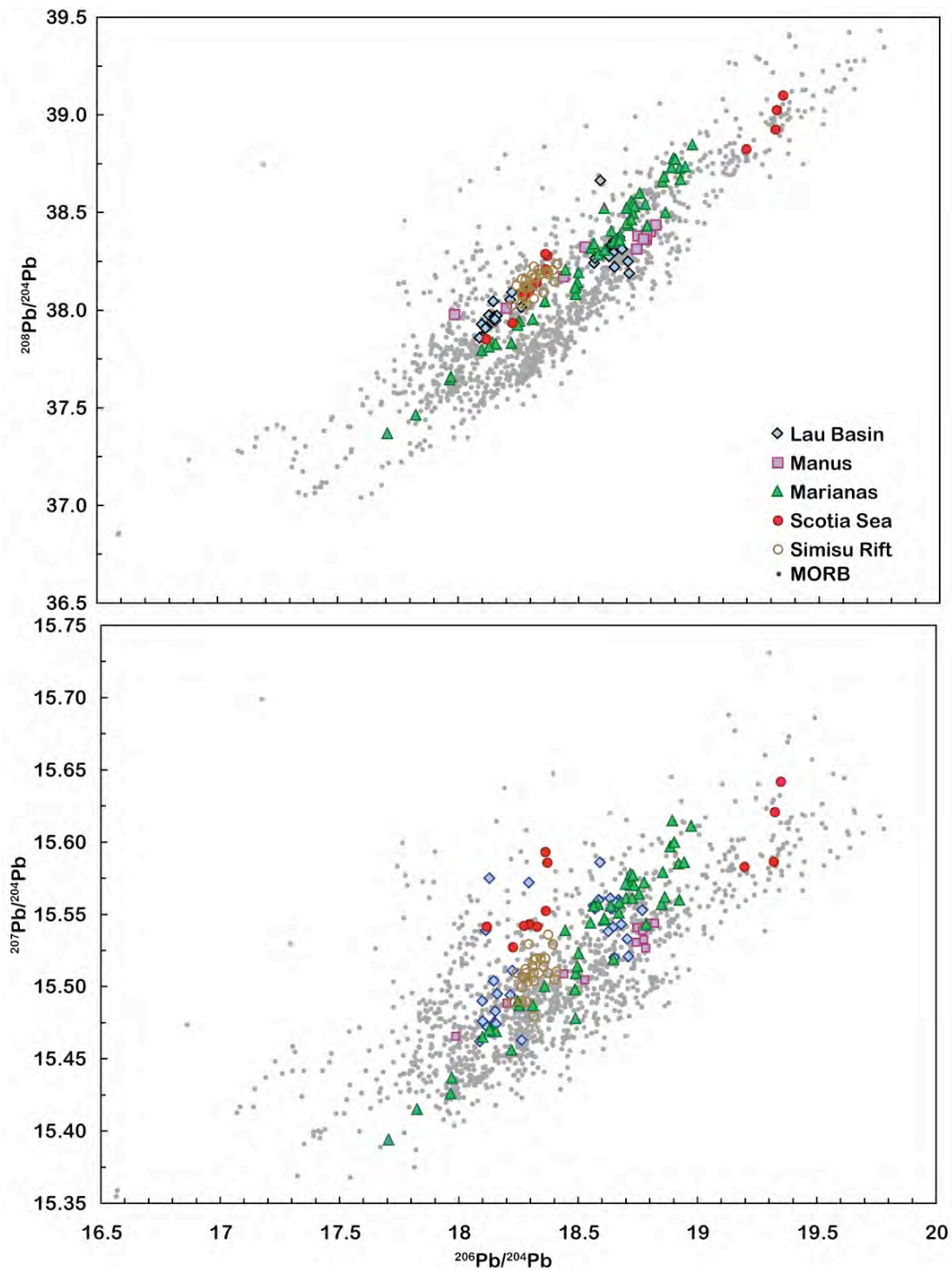


Figure 24. Pb isotope ratios in BABB. BABB have Pb isotope ratios that are similar to MORB, although there is a tendency for BABB to have higher $^{208}\text{Pb}/^{204}\text{Pb}$ for a given $^{206}\text{Pb}/^{204}\text{Pb}$ and some tendency for BABB to scatter to higher $^{207}\text{Pb}/^{204}\text{Pb}$. Data from the PetDB database.

Table 1. Major Element Chemistry of Mid-Ocean Ridge Basalts

	All Whole Rocks					Atlantic		Indian		Pacific		Glasses	Arevalo & McDonough
	Mean	Median	Mode	σ	% σ	Mean	σ	Mean	σ	Mean	σ	Mean	Mean
SiO₂	50.06	50.06	49.90	1.13	2.3	50.04	0.75	49.93	0.89	50.10	1.42	50.60	50.57
TiO₂	1.52	1.50	1.54	0.43	28.5	1.33	0.34	1.41	0.50	1.71	0.42	1.67	1.46
Al₂O₃	15.00	14.83	14.40	1.25	8.3	15.20	1.08	16.03	1.34	14.63	1.24	14.79	15.51
FeO_T	10.36	10.31	9.59	1.57	15.1	10.18	1.36	9.10	1.53	10.74	1.61	10.46	9.50
MnO	0.19	0.18	0.19	0.03	14.4	0.18	0.02	0.17	0.03	0.19	0.03	0.19	0.16
MgO	7.71	7.66	7.24	1.31	17.0	7.98	1.14	7.83	1.25	7.45	1.41	7.42	7.69
CaO	11.46	11.57	11.50	0.91	8.0	11.59	0.78	11.24	0.98	11.37	1.00	11.38	11.39
Na₂O	2.52	2.54	2.47	0.41	16.4	2.37	0.40	2.86	0.63	2.61	0.31	2.77	2.74
K₂O	0.19	0.14	0.06	0.18	96.3	0.19	0.18	0.35	0.31	0.16	0.14	0.19	0.18
P₂O₅	0.16	0.15	0.15	0.08	52.6	0.14	0.06	0.18	0.11	0.18	0.10	0.18	0.15
H₂O	0.45	0.39	0.25	0.26	58.0	0.46	0.26	0.57	0.19	0.40	0.29	—	—
Total	99.15	99.14	99.57			99.20		99.09	0.48	99.12	0.62	99.65	99.35
Mg#	59	60	56	7	11.5	61		63	6	58	8	58	59
number	2010					877		152			967	3129	712

	C.I.P.W Norms					
Anorthite	28.53	29.81	29.33	27.21	26.70	28.90
Albite	27.68	29.02	24.49	26.99	25.70	25.70
Plagioclase	50.76	50.67	54.50	50.20	50.95	52.93
Orthoclase	1.12	1.12	2.07	0.95	1.12	1.06
Diopside	22.06	21.64	20.29	22.75	22.95	21.36
Hypersthene	16.89	18.00	9.16	17.30	15.57	15.53
Olivine	4.21	4.03	9.37	3.37	4.15	4.43
Ilmenite	2.91	2.54	2.70	3.29	3.17	2.79
Magnetite	1.68	1.65	1.48	1.74	1.70	1.54
Apatite	0.37	0.32	0.42	0.42	0.42	0.35

Table 2. Average Trace Element Concentrations in Mid-Ocean Ridge Basalts in ppm.

	Global Mean	Global LN Mean	σ	n	NMORB LN Mean	NMORB Mean	σ	n	Arevalo & McDonough* LN Mean	Sun & McDonough* NMORB	Hofmann* NMORB
Li	6.63	6.39	2.07	399	6.38	6.64	2.19	249			
Be	0.64	0.55	0.40	358	0.45	0.50	0.28	231			
B	1.80	1.62	0.80	259	1.38	1.53	0.62	150			
K	1237	932	1179	203	731	857	536	147	1620	600	884
Sc	36.8	36.4	5.00	507	38.1	38.3	4.0	377			
V	299	290	63.9	685	308	314	55.3	468			
Cr	331	314	87.9	170	318	334	84.4	158			
Co	43.7	43.2	6.25	332	43.6	43.9	5.4	224			
Ni	100	89.8	49.5	773	95.6	104	49.8	519			
Cu	80.8	77.4	24.7	408	79.0	82.0	23.3	314			
Zn	86.8	84.3	21.0	452	85.8	88.0	20.1	345			
Rb	4.05	2.10	5.12	1265	1.06	1.36	1.07	791		0.56	1.26
Sr	138	126	68.3	1668	107	110	28.0	1152	130	90	113
Y	32.4	30.9	13.1	1530	30.7	32.2	10.9	1072	30	28	35.8
Zr	103	92.1	60.3	1530	88.3	88.8	40.4	1075	90.1	74	104
Nb	6.44	3.82	7.98	1450	2.33	2.8	1.88	1026	3.44	2.33	3.51
Cs	0.053	0.029	0.06	588	0.015	0.019	0.02	371		0.007	0.014
Ba	43.4	21.3	59.3	1584	11.3	14.7	11.5	1051	16.60	6.3	13.9
La	4.87	3.68	4.78	824	2.98	3.39	1.98	643	3.77	2.5	3.9
Ce	13.1	10.7	10.8	824	9.13	10.2	5.72	643	11.50	7.5	12
Pr	2.08	1.76	1.52	823	1.56	1.74	0.94	643	1.91	1.32	2.07
Nd	10.4	9.20	6.39	824	8.48	9.22	4.47	643	9.80	7.3	11.2
Sm	3.37	3.10	1.69	824	2.99	3.19	1.35	643	3.25	2.63	3.75
Eu	1.20	1.14	0.45	824	1.11	1.15	0.38	643	1.22	1.02	1.34
Gd	4.42	4.11	2.02	775	4.05	4.29	1.72	604	4.40	3.68	5.08
Tb	0.81	0.76	0.44	818	0.76	0.81	0.45	638	0.78	0.67	0.89
Dy	5.28	4.99	2.16	815	5.05	5.27	1.84	634	5.11	4.55	6.3
Ho	1.14	1.08	0.46	824	1.10	1.14	0.39	643	1.11	1.01	1.34
Er	3.30	3.11	1.38	823	3.18	3.31	1.16	642	3.15	2.97	4.14
Tm	0.49	0.45	0.22	702	0.47	0.49	0.18	536	0.48	0.46	0.62
Yb	3.17	2.99	1.35	824	3.07	3.20	1.10	643	3.00	3.05	3.9
Lu	0.48	0.45	0.21	815	0.47	0.49	0.17	635	0.45	0.455	0.589
Hf	2.62	2.38	1.40	1160	2.20	2.36	1.09	855	2.4	2.05	2.97
Ta	0.417	0.262	0.48	1114	0.161	0.191	0.13	763	0.224	0.13	0.192
W	0.043	0.027	0.06	94	0.021	0.026	0.02	77			
Pb	0.657	0.550	0.44	1255	0.419	0.460	0.20	812	0.57	0.3	0.489
Th	0.491	0.269	0.65	1458	0.148	0.186	0.14	919	0.219	0.120	0.187
U	0.157	0.094	0.24	1415	0.060	0.068	0.05	879	0.080	0.047	0.071

Table 2b. Average Trace Element Concentrations by Ocean Basin

	Atlantic				Pacific				Indian			
	Mean	LN Mean	σ	n	Mean	LN Mean	σ	n	Mean	LN Mean	σ	n
Li	6.28	6.13	1.31	299	8.36	7.75	3.81	59	6.71	6.51	1.92	41
Be	0.607	0.533	0.33	282	0.76	0.68	0.43	41	0.785	0.534	0.711	35
B	1.82	1.64	0.78	224				0	1.66	1.44	0.90	35
K	1537	1100	1628	71	1102	886	810	104	982	737	809	28
Sc	35.5	35.2	4.33	272	40.0	39.8	3.95	151	35.0	34.4	5.92	84
V	295	291	46.8	399	324	307	82.9	197	261	254	59.6	88
Cr	341	324	106	56	315	291	89.5	66	341	337	54.1	48
Co	46.4	46.1	5.2	96	43.3	42.6	7.06	144	41.42	41.2	4.63	91
Ni	104	97.2	38.5	448	85.7	70.3	67.4	219	114.4	107	40.0	105
Cu	92.4	89.2	24.9	205	70.6	69.4	15.1	100	67.5	65.0	20.7	102
Zn	83.2	81.2	17.2	207	100	98.3	21.8	148	73.8	72.5	15.1	96
Rb	4.39	2.29	5.16	816	2.80	1.53	3.77	231	4.11	2.12	5.93	218
Sr	139	127	69.8	874	125.0	119.9	40.6	478	146.0	133.7	73.1	312
Y	30.1	29.3	7.03	806	38.5	35.6	20.6	433	29.5	28.6	7.95	287
Zr	93.9	86.2	39.5	794	118	104	82.5	460	100	90.0	57.4	272
Nb	6.83	4.07	7.72	773	5.43	3.38	7.15	399	6.82	3.90	9.51	278
Cs	0.048	0.025	0.059	419	0.06	0.04	0.05	96	0.07	0.04	0.08	73
Ba	50.1	24.5	62.5	855	25.8	14.6	35.3	399	44.4	22.5	63.4	326
La	5.73	4.24	5.04	892	5.28	4.10	5.12	462	5.43	4.09	5.62	345
Ce	14.6	11.8	10.5	831	14.8	12.4	12.0	489	14.3	11.7	12.0	323
Pr	1.63	1.43	0.91	299	2.40	2.08	1.77	331	2.07	1.89	1.01	235
Nd	10.9	9.83	5.21	881	12.23	10.90	7.83	522	10.7	9.66	6.01	361
Sm	3.36	3.17	1.18	863	3.94	3.65	1.99	538	3.34	3.14	1.38	356
Eu	1.23	1.17	0.37	828	1.41	1.33	0.56	487	1.21	1.16	0.41	324
Gd	4.40	4.23	1.25	781	5.27	4.88	2.66	413	4.24	4.03	1.55	253
Tb	0.705	0.683	0.174	333	0.94	0.86	0.61	355	0.73	0.71	0.17	259
Dy	5.08	4.94	1.2	772	6.31	5.88	3.06	426	4.91	4.74	1.44	288
Ho	1.04	1.01	0.24	290	1.30	1.22	0.57	325	1.03	1.00	0.24	232
Er	3.10	3.02	0.72	766	3.85	3.61	1.74	423	3.02	2.92	0.84	296
Tm	0.427	0.417	0.09	259	0.57	0.53	0.27	269	0.44	0.43	0.12	192
Yb	3.01	2.93	0.71	812	3.71	3.47	1.77	474	2.84	2.74	0.78	322
Lu	0.447	0.436	0.099	572	0.56	0.52	0.24	395	0.43	0.42	0.12	307
Hf	2.39	2.20	1.01	513	2.99	2.71	1.71	382	2.49	2.27	1.38	261
Ta	0.455	0.293	0.461	642	0.36	0.23	0.46	291	0.37	0.21	0.55	180
W	0.048	0.027	0.090	36	0.04	0.03	0.03	34	0.04	0.03	0.05	24
Pb	0.670	0.554	0.420	682	0.58	0.50	0.40	315	0.69	0.59	0.47	254
Th	0.518	0.293	0.58	806	0.40	0.22	0.65	390	0.52	0.27	0.79	257
U	0.158	0.103	0.16	782	0.12	0.08	0.17	374	0.15	0.09	0.22	250

*Arevalo & McDonough (2010)

† Sun & McDonough (1989)

‡Hofmann (1988)

Table 3a. Average Trace Element Ratios in MORB and Back Arc Basin Basalts

	Global MORB				NMORB			Global BABB		
	Mean	Median	σ	n	Mean	σ	n	Mean	σ	n
La/Sm	1.43	1.12	0.81	1637	1.01	0.25	1173	1.80	0.87	318
(La/Sm)_N	0.90	0.70	0.51	1637	0.63	0.16	1173	1.13	0.54	318
La/Yb	1.84	1.17	1.84	1576	1.04	0.37	1120	2.20	1.60	326
Sm/Yb	1.13	1.07	0.34	1599	1.01	0.18	1148	1.18	0.30	341
Ba/La	6.05	5.33	3.76	1522	4.41	2.77	1038	14.00	10.10	349
Nb/La	0.95	0.92	0.33	1389	0.81	0.24	959	0.64	0.36	285
Zr/Nb	30.73	26.64	22.03	1363	39.83	20.83	935	38.0	30.7	347
Sm/Nd	0.333	0.338	0.043	1704	0.353	0.029	1227	0.312	0.044	418
Ba/Rb	11.5	11.2	2.6	1162	11.2	2.6	713	11.9	5.9	474
Rb/Cs	83.4	81.2	25.6	582	77.8	25.2	365	52.8	20.4	184
Pb/Ce	0.045	0.044	0.011	1174	0.046	0.0117	763	0.11	0.07	230
Nb/Ta	15.3	15.4	1.6	1090	14.9	1.6	743	15.2	2.35	174
Zr/Hf	37.5	37.2	4.1	1092	36.6	3.7	808	38.6	5.21	233
Rb/Sr	0.024	0.016	0.021	1247	0.013	0.009	783	0.038	0.06	547
Th/U	3.06	3.00	0.90	1382	2.82	0.89	861	2.85	0.66	197
U/Pb	0.208	0.181	0.122	1162	0.155	0.088	738	0.164	0.07	177
Nb/U	45.1	45.2	9.9	1201	44.2	11.3	796	20.76	14.47	185
K/U	16775	16469	3753	131	17328	3652	103	17351	4189	136
K/Rb	907.1	848.7	468.6	108	956.3	455.3	77	529	193	433
K/La	280.5	275.2	71.7	139	265.4	58.2	115	595	310	289
W/U	0.60	0.47	0.34	94	0.61	0.37	77	—	—	—
Y/Ho	28.1	27.9	2.49	788	28.1	2.13	624	28.4	3.9	222
Eu*	0.98	0.98	0.09	1447	0.97	0.09	1028	0.99	0.08	326
Sr*	0.82	0.79	0.025	1554	0.77	0.2	1114	1.40	0.74	388

Table 3b. Correlation Matrix for Trace Element Ratios in MORB

	La/Sm	La/Yb	Sm/Yb	Ba/La	Nb/La	Zr/Nb	Sm/Nd	Ba/Rb	Rb/Cs	Pb/Ce	Nb/Ta	Zr/Hf	Rb/Sr	Th/U	U/Pb	Nb/U	K/U	K/Rb	K/La	W/U	Y/Ho	Eu*	Sr*
La/Sm	1																						
La/Yb	0.92	1																					
Sm/Yb	0.77	0.90	1																				
Ba/La	0.68	0.56	0.43	1																			
Nb/La	0.70	0.56	0.42	0.70	1																		
Zr/Nb	-0.68	-0.53	-0.42	-0.71	-0.83	1																	
Sm/Nd	-0.88	-0.78	-0.73	-0.53	-0.61	0.62	1																
Ba/Rb	0.15	0.15	0.13	0.31	-0.04	-0.03	-0.10	1															
Rb/Cs	0.29	0.32	0.37	0.16	0.13	-0.27	-0.33	-0.02	1														
Pb/Ce	-0.24	-0.22	-0.21	-0.08	-0.34	0.28	0.25	0.10	-0.04	1													
Nb/Ta	0.44	0.37	0.33	0.49	0.56	-0.51	-0.42	-0.05	0.27	-0.07	1												
Zr/Hf	0.46	0.42	0.48	0.17	0.28	-0.29	-0.61	-0.06	0.13	-0.14	0.29	1											
Rb/Sr	0.77	0.61	0.52	0.65	0.64	-0.67	-0.71	-0.06	0.24	-0.25	0.44	0.41	1										
Th/U	0.41	0.33	0.33	0.44	0.23	-0.38	-0.40	0.28	0.28	0.04	0.16	0.28	0.39	1									
U/Pb	0.67	0.57	0.44	0.57	0.78	-0.60	-0.58	-0.02	0.05	-0.59	0.34	0.33	0.61	0.09	1								
Nb/U	0.19	0.13	0.17	0.20	0.25	-0.36	-0.20	0.15	0.13	-0.17	0.20	0.15	0.17	0.58	-0.08	1							
K/U	-0.34	-0.31	-0.31	-0.28	-0.53	0.39	0.33	0.20	0.16	0.66	-0.25	-0.28	-0.68	0.31	-0.65	-0.10	1						
K/Rb	-0.34	-0.34	0.06	-0.60	-0.43	0.27	0.28	0.28	-0.06	0.31		0.36	-0.53	-0.45	-0.44	-0.15	0.37	1					
K/La	0.43	0.44	0.52	0.61	0.62	-0.59	-0.49	0.16	-0.25	0.07	0.48	0.14	0.54	0.18	0.47	-0.19	0.14	-0.16	1				
W/U	-0.18	-0.13	-0.37	0.04	-0.24	0.46	0.47	0.41	-0.24	0.37	-0.11	-0.45	0.47	0.14	-0.13	-0.16	0.29		-0.03	1			
Y/Ho	0.06	0.05	0.09	0.05	0.01	-0.10	-0.09	0.08	-0.11	0.02	-0.04	0.26	-0.01	0.12	-0.06	0.27	-0.06	0.08	-0.18	0.10	1		
Eu*	0.12	0.15	0.16	0.14	0.04	-0.02	-0.10	0.07	0.08	0.08	0.15	-0.04	-0.10	-0.04	-0.03	0.00	0.20	-0.03	0.23	0.14	0.01	1	
Sr*	0.35	0.36	0.30	0.41	0.22	-0.18	-0.26	0.26	0.05	0.07	0.18	0.17	-0.01	0.10	0.17	0.08	0.23	0.14	0.45	0.14	0.22	0.48	1

Table 4. Isotope Ratios in MORB and Back-Arc Basin Basalts BABB

	⁸⁷ Sr/ ⁸⁶ Sr	ε _{Nd}	²⁰⁶ Pb/ ²⁰⁴ Pb	²⁰⁷ Pb/ ²⁰⁴ Pb	²⁰⁸ Pb/ ²⁰⁴ Pb	ε _{Hf}	δ ⁷ Li	δ ¹⁸ O	δ ¹³ C	δD	δ ¹⁵ N	δ ³⁴ S	δ ¹¹ B
Global													
Mean	0.70289	8.53	18.404	15.505	38.082	14.19	3.04	5.69	-5.99	-67.14	-2.00	0.06	-4.25
Median	0.70282	8.95	18.349	15.497	38.001	14.25	3.00	5.64	-6.30	-66.90	-2.20	0.20	-4.35
σ	0.00048	2.29	0.449	0.054	0.450	4.04	0.59	0.33	1.69	11.23	2.51	1.66	2.13
n	1557	1411	1372	1345	1345	526	7	216	68	95	72	11	20
NMORB													
Mean	0.70273	9.25	18.283	15.490	37.916	15.04							
Median	0.70270	9.48	18.284	15.487	37.867	14.57							
σ	0.00030	1.57	0.338	0.044	0.327	3.36							
n	1094	985	877	857	857	328							
Atlantic													
Mean	0.70304	8.31	18.493	15.511	38.195	14.81	3.10	5.74	-6.50	-69.21	-0.94	-0.58	-4.91
Median	0.70296	8.90	18.384	15.508	38.163	15.86	3.20	5.67	-7.00	-70.00	-1.50	-0.10	-5.10
σ	0.00057	2.78	0.472	0.061	0.477	4.76	0.36	0.40	1.43	10.23	2.92	2.04	2.27
n	610	564	581	560	560	292	3	78	23	57	11	6	11
Pacific													
Mean	0.70261	9.37	18.502	15.508	38.025	13.23		5.68	-6.65	-64.03	-3.03	0.84	-3.91
Median	0.70254	9.54	18.460	15.498	37.953	13.69		5.62	-7.40	-64.00	-3.25	1.00	-4.20
σ	0.00023	1.40	0.295	0.044	0.372	2.04		0.28	2.43	12.06	2.64	0.50	1.65
n	566	493	449	444	444	141		115	9	38	20	5	7
Indian													
Mean	0.70307	7.72	18.125	15.490	37.972	13.70	3.00	5.58	-5.50		-1.79		-1.80
Median	0.70296	7.92	18.074	15.483	37.892	13.97	2.75	5.55	-5.90		-2.00		-1.80
σ	0.00040	2.01	0.461	0.051	0.458	3.51	0.78	0.18	1.52		2.20		0.85
n	381	354	342	341	341	93	4	23	36	0	41	0	2
BABB													
Mean	0.70324	7.81	18.484	15.529	38.237	16.41		5.81	-6.80	-44.15	0.07	1.09	-2.90
Median	0.70319	8.02	18.487	15.533	38.212	15.29		5.80	-7.19	-40.90	-0.10	0.80	-1.80
σ	0.00047	1.42	0.299	0.042	0.288	3.31		0.23	2.10	15.92	0.67	1.94	2.21
n	306	275	137	137	137	6		78	45	21	3	20	5

ε_{Nd} is calculated as [(¹⁴³Nd/¹⁴⁴Nd)_{sample}/(¹⁴³Nd/¹⁴⁴Nd)_{chondrites} - 1] x 10,000 where (¹⁴³Nd/¹⁴⁴Nd)_{chondrites} = 0.512638.

ε_{Hf} is calculated as [(¹⁷⁷Hf/¹⁷⁶Hf)_{sample}/(¹⁷⁷Hf/¹⁷⁶Hf)_{chondrites} - 1] x 10,000 where (¹⁷⁷Hf/¹⁷⁶Hf)_{chondrites} = 0.282786.

Table 5a. Major element Composition of the Bulk Oceanic Crust

	Bulk Crust Wt %	Ave. MORB* (Layer 2)	Lower Crust [†] (Layer 3)			Cumulate
			Mean	σ	Median	
SiO ₂	50.1	50.06	50.6	±1.6	51.0	48.9
TiO ₂	1.1	1.52	0.78	±0.81	0.4	0.12
Al ₂ O ₃	15.7	15.00	16.7	±2.3	16.6	16.4
Fe ₂ O ₃	1.4					0.47
FeO	7.1					4.63
FeO _T	8.3	10.36	7.5	±3	6.1	5.1
MnO	0.11	0.19	0.14	±0.05	0.1	0.03
MgO	10.3	7.71	9.4	±1.1	9.0	14.5
CaO	11.8	11.46	12.5	±1	12.6	13.46
Na ₂ O	2.21	2.52	2.35	±0.45	2.4	1.34
K ₂ O	0.11	0.19	0.06	±0.03	0.1	0.01
P ₂ O ₅	0.10	0.16	0.02	±0.02	0.0	0.0
Total	99.7	99.2	100.1		98.3	99.8
Mg#	72	59	69	±10	73	85

Table 5b. Calculated Trace Element Composition of the Bulk Oceanic Crust

	Bulk Crust (ppm)	Ave. MORB*	Lower Crust [†]			D _{OI}	D _{Cpx}	D _{plag}	Bulk D [‡]
			Mean	σ	Median				
Li	3.52	6.63				0.35	0.25	0.3	0.283
Be	0.31	0.64				0.03	0.05	0.37	0.178
B	0.80	1.80				0.1	0.036	0.13	0.083
K	651	1237							
Sc	36.2	37	37	± 12	40	0.3	2	0.08	0.983
V	177	299	209	± 136	162	0.08	0.78	0.1	0.407
Cr	317	331	308	± 129	285				
Co	31.7	44	50	± 26	41				
Ni	134	100	138	± 45	159				
Cu	43.7	80.8	71	± 19	65	0.55	0.36	0.17	0.307
Zn	48.5	86.8	38	± 9.6	39	0.8	0.4	0.13	0.342
Rb	1.74	4.05				0.0004	0.01	0.1	0.046
Sr	103	138	115	± 30	97	0.0001	0.13	1.5	0.674
Y	18.1	32.4	13.9	± 7.4	13	0.005	0.75	0.008	0.345
Zr	44.5	103	28.4	± 13.6	28	0.001	0.12	0.003	0.056
Nb	2.77	6.44	0.93	± 0.65	1	0.00001	0.01	0.1	0.046
Cs	0.02	0.05				0.0002	0.006	0.1	0.044
Ba	19.4	43.4				0.000001	0.0005	0.25	0.103
La	2.13	4.87	0.86	± 0.68	0.83	0.000001	0.07	0.08	0.065
Ce	5.81	13.1	2.75	± 1.95	2.76	0.000005	0.12	0.06	0.079
Pr	0.94	2.08	0.52	± 0.38	0.53	0.00001	0.18	0.05	0.102
Nd	4.90	10.4	2.78	± 1.86	2.61	0.00005	0.28	0.05	0.148
Sm	1.70	3.37	1.1	± 0.68	1.09	0.0001	0.45	0.05	0.225
Eu	0.62	1.20	0.58	± 0.25	0.58	0.0005	0.45	0.50	0.250
Gd	2.25	4.42	1.6	± 0.93	1.6	0.001	0.49	0.04	0.240
Tb	0.43	0.81	0.31	± 0.18	0.3	0.005	0.56	0.04	0.272
Dy	2.84	5.28	2.09	± 1.17	2.06	0.01	0.62	0.04	0.300
Ho	0.63	1.14	0.46	± 0.29	0.48	0.013	0.66	0.05	0.323
Er	1.85	3.30	1.34	± 0.77	1.32	0.015	0.72	0.05	0.350
Tm	0.28	0.49				0.018	0.76	0.06	0.373
Yb	1.85	3.17	1.27	± 0.74	1.23	0.02	0.8	0.06	0.391
Lu	0.28	0.48	0.19	± 0.11	0.18	0.03	0.8	0.06	0.393
Hf	1.21	2.62				0.01	0.24	0.03	0.123
Ta	0.18	0.417				0.00001	0.01	0.17	0.074
Pb	0.47	0.657				0.0001	0.001	1.5	0.615
Th	0.21	0.491				0.00001	0.0013	0.13	0.054
U	0.07	0.157				0.00001	0.0001	0.1	0.041

*From Table 1.

[†]From Chapter 15, Table 2[‡]Elements for which no partition coefficient is shown were calculated within MELTS.

Table 6. Major Element Chemistry of Back-Arc Basin Basalts

	Global Average			Lau Basin			Okinawa Trough			North Fiji Basin		
	Mean	Median	σ	Mean	Median	σ	Mean	Median	σ	Mean	Median	σ
SiO₂	52.02	50.96	4.19	51.83	51.20	2.71	56.44	51.81	8.97	49.76	49.80	0.86
TiO₂	1.29	1.22	0.58	1.33	1.19	0.90	0.82	0.95	0.30	1.65	1.58	0.30
Al₂O₃	15.64	15.79	1.32	14.80	14.83	1.24	15.44	15.89	1.39	15.10	14.93	0.93
FeO_T	9.34	9.25	2.25	10.79	10.51	2.55	7.44	8.87	3.11	10.08	10.06	1.21
MnO	0.18	0.18	0.04	0.19	0.19	0.03	0.15	0.16	0.06	0.17	0.18	0.03
MgO	6.50	6.95	2.04	6.62	7.03	2.12	5.11	6.33	2.92	7.62	7.77	0.99
CaO	10.65	11.25	2.25	10.86	11.50	2.10	8.81	11.46	4.09	11.55	11.68	0.76
Na₂O	2.84	2.73	0.75	2.54	2.55	0.66	2.98	2.52	0.99	2.68	2.65	0.26
K₂O	0.39	0.28	0.44	0.21	0.15	0.18	1.06	0.51	0.99	0.24	0.13	0.24
P₂O₅	0.16	0.15	0.09	0.14	0.11	0.10	0.14	0.16	0.06	0.16	0.14	0.08
H₂O	1.00	1.02	0.61	0.70	0.59	0.48	—	—	—	0.81	0.74	0.54
Total	100.00	99.78		100.01	99.84		98.40	98.65		99.82	99.65	
Mg#	0.58			0.55			0.58			0.60		
number	966			253			22			185		

Table 7. Average Trace Element Concentrations in Back-Arc Basin Basalts

	BABB Mean	σ	n	Lau Basin	Okinawa Trough	North Fiji Basin	MORB Mean	NMORB Mean
Li	6.99	5.08	122	8.15	—	—	6.63	6.64
Be	0.62	0.31	14	0.85	—	—	0.64	0.50
B	4.56	3.01	25	4.25	—	—	1.80	1.53
K	3273	3687	989	1794	8807	1981	1237	857
Sc	36.4	7.7	352	38.1	36.8	36.3	36.8	38.3
V	282	98	583	332	176	285	299	314
Cr	183	141	554	186	174	254	331	334
Co	45.9	40.4	362	40.5	37.5	42.9	43.7	43.9
Ni	82.8	75.8	580	86.2	65.1	107	100	104
Cu	78.9	34.7	437	94.4	—	81.7	80.8	82.0
Zn	86.5	25.8	376	94.9	—	88.2	86.8	88.0
Rb	7.51	9.54	555	4.96	61.5	4.02	4.05	1.36
Sr	194	98	690	130	208	139	138	110
Y	28.3	11.0	517	30.9	23.6	32.6	32.4	32.2
Zr	89.7	44.2	502	69.9	125	101	103	88.8
Nb	4.19	4.58	363	1.87	4.93	5.88	6.44	2.8
Cs	0.19	0.19	188	0.15	0.41	0.12	0.053	0.019
Ba	81.07	88.7	584	55.8	213	42.7	43.4	14.7
La	6.30	4.60	364	3.73	7.04	5.70	4.87	3.39
Ce	15.2	9.80	370	10.5	16.8	15.9	13.1	10.2
Pr	2.21	1.22	227	1.82	2.37	2.19	2.08	1.74
Nd	11.0	5.18	452	10.0	11.0	11.22	10.4	9.22
Sm	3.34	1.59	434	3.38	3.04	3.37	3.37	3.19
Eu	1.15	.43	369	1.13	1.10	1.15	1.20	1.15
Gd	4.10	2.20	326	4.51	3.45	4.36	4.42	4.29
Tb	0.74	0.44	229	0.82	0.59	0.73	0.81	0.81
Dy	4.80	2.66	337	5.60	3.72	5.28	5.28	5.27
Ho	1.05	2.66	236	1.22	0.80	0.99	1.14	1.14
Er	2.99	1.7	346	3.53	2.33	3.21	3.30	3.31
Tm	0.47	0.32	203	0.56	0.35	0.41	0.49	0.49
Yb	2.97	1.73	370	3.52	2.20	3.07	3.17	3.20
Lu	0.46	0.30	274	0.55	0.34	0.43	0.48	0.49
Hf	2.27	1.75	242	2.38	1.79	2.66	2.62	2.36
Ta	0.270	0.281	190	0.11	0.25	0.46	0.417	0.191
W	0.071	0.031	22	0.078	—	—	0.043	0.026
Pb	1.67	1.22	247	1.13	2.16	1.85	0.657	0.460
Th	0.778	0.701	242	0.37	0.81	—	0.491	0.186
U	0.235	0.181	208	0.16	0.19	—	0.157	0.068